

QATAR UNIVERSITY

COLLEGE OF ENGINEERING

AN INVESTIGATION INTO FOULING, WETTING AND THEIR MITIGATION

USING COMMERCIAL ANTISCALANT IN MEMBRANE DISTILLATION

DESALINATION

BY

REEM FOUAD YOUNIS

A Thesis Submitted to the Faculty of

the College of Engineering

in Partial Fulfillment

of the Requirements

for the Degree of

Masters of Science in Environmental Engineering

May 2017

© 2017 Reem Fouad Younis. All Rights Reserved.

COMMITTEE PAGE

The members of the Committee approve the Thesis of Reem Fouad Younis
defended on 16/05/2017.

Prof. Farid Benyahia
Thesis/Dissertation Supervisor

Prof. NorEddine Ghaffour
Committee Member

Prof. Samer Ahmed
Committee Member

Dr. Renju Zacharia
Committee Member

Approved:

Khalifa Al-Khalifa, Dean, College of Engineering

ABSTRACT

YOUNIS, REEM, F., Masters: June: [2017:], Masters of Science in Environmental Engineering

Title: An investigation into fouling, wetting and their mitigation using a commercial antiscalant in membrane distillation desalination

Supervisor of Thesis: Prof. Farid Benyahia

An experimental investigation into membrane fouling and loss of hydrophobicity was carried out in direct contact membrane distillation (DCMD) desalination of high salinity seawater. The membrane used was a commercial hydrophobic polypropylene flat-sheet with nominal pore size of 0.2 microns and a porosity of 73-75%. Extended runs of up to 91 hours in batch mode were conducted at various temperatures and flowrates, namely 50-70 °C and 1.5-2.5 L/min respectively. Some runs consisted of injecting antiscalant. The results obtained showed that the membrane becomes significantly fouled at temperatures above 50 °C often leading to significant distillate flux decline and a modest reduction of salt rejection, indicating that partial membrane wetting has occurred. It was found that the flux declined by 74% and 92% for temperatures of 60 °C and 70 °C, respectively at feed flowrate of 1.5 L/min. The effect of flowrate on the overall flux decline was not significant. The loss of hydrophobicity was studied using distillate conductivity and used membrane surface contact angle. In this work, both partial and surface membrane wetting were observed. The modest membrane wetting occurred at 70 °C and 1.5 L/min and led to the lowest salt rejection of around 86%. However, at flowrate of 2.5 L/min regardless of the feed temperature studied, the salt rejection was higher than 99%. The morphology of the membrane and the chemical composition of the fouling components were studied using SEM and EDS. These were mainly carbonates of Ca and Mg and to a lesser extent, sulfates of Ca. Sodium chloride deposits and traces of silicates and iron were also observed. The presence of calcium

sulfate in the membrane surface was associated with the lowest salt rejection experiments, indicating that this foulant could be responsible for the membrane wetting mechanism. Experiments performed with commercial antiscalant injected in the feed with a dose of 4 ppm showed that fouling and wetting were almost completely prevented. This work has successfully shown that fouling in membrane distillation desalination can be mitigated using commercial antiscalant. However, the importance of developing high performance membranes was recommended to reduce the demand of costly antiscalant injection.

DEDICATION

I would like to dedicate this work in the first place to my loving parents, Fouad Y. and Wafa A. and to express my deep gratitude towards them. Without their continuous support and motivation throughout the process, the achievement of this work would have not been possible.

ACKNOWLEDGMENTS

First, I would like to express my profound appreciation to my thesis advisor professor Farid Benyahia at Qatar university. He steadily permitted this work to be my own, but he always directed me when he thought I needed it. His office door was open to me whenever I was facing difficulties with my thesis writing and research. I should admit he generously supported me during my master research. Without his advice, this work would not have been in as good shape as it is now. I'm really honored to have a professor with his patience and kindness with me all the time.

I am thankful to the College of Engineering for the award of a graduate assistantship. I would also like to thank the Chemical Engineering department at Qatar university for providing laboratory, space and chemical analysis of samples, and the central laboratory unit (CLU) for providing SEM services.

I would also like to acknowledge ConocoPhillips Global Water Sustainability Center (GWSC) for funding the project equipment.

Last, but not least I would like to thank my supportive friends for their continuous heartily encouragement throughout my masters.

TABLE OF CONTENTS

DEDICATION	v
ACKNOWLEDGMENTS.....	vi
Nomenclature	xix
1 Introduction	1
1.1 Objective and scope of work	3
2 Membrane distillation	4
2.1 MD configurations	4
2.1.1 Direct contact membrane distillation (DCMD)	4
2.1.2 Air-gap membrane distillation (AGMD)	5
2.1.3 Sweeping gas membrane distillation (SGMD)	5
2.1.4 Vacuum membrane distillation (VMD)	6
2.1.5 Module configurations and membrane materials	7
2.1.6 Membrane characteristics	9
2.2 Theoretical background	10
2.2.1 Mass transfer	11
2.2.2 Heat transfer	12
2.3 Temperature polarization (TP).....	13
2.4 Concentration polarization (CP).....	14

3	Membrane Distillation Challenges: Fouling, scaling and wetting (including membrane autopsies, and state of art).....	15
3.1	Fouling in membrane distillation	15
3.1.1	Inorganic fouling	20
3.2	Inorganic scaling in membrane distillation	22
3.2.1	Alkaline scale in MD	22
3.2.2	Non-alkaline scaling	27
3.3	Factors that influence scaling in MD.....	29
3.3.1	Temperature	29
3.3.2	Dissolved gases	29
3.3.3	Water source.....	30
3.4	Effect of scaling and fouling on the membrane distillation performance	31
3.4.1	Membrane wetting	31
3.4.2	Permeate flux decline	36
3.4.3	Increased concentration and temperature polarization	37
3.4.4	Membrane damage and chemical degradation.....	37
3.4.5	Effect of temperature on fouling	40
3.4.6	Effect of feed flowrate on fouling	42
3.5	Fouling mitigation and control.....	45
3.5.1	Use of antiscalant.....	45

3.5.2	Membrane cleaning	47
3.5.3	Gas bubbling	49
3.5.4	Magnetic water treatment (MWT)	49
3.5.5	Membrane modification and enhanced properties	50
3.6	Fouling monitoring and used membrane characterization	51
3.6.1	Physical characterization	53
3.6.2	Chemical characterization.....	55
4	Experimental Methodology	58
4.1	DCMD bench scale unit.....	58
4.2	Feed solution.....	60
4.3	Membrane flat-sheet.....	61
4.4	Configuration of DCMD Unit.....	62
4.5	The MD module construction materials	66
4.6	The MD module dimensions	67
4.7	Auxiliary equipment details	69
4.7.1	Heater and cooler	69
4.7.2	Pump and tubing.....	69
4.7.3	Digital balance.....	71
4.7.4	Temperature sensors	71
4.7.5	Conductivity meter	72

4.7.6	Data acquisition scheme	72
4.8	Experimental method	73
4.8.1	Experimental operation	73
4.8.2	Antiscalant	75
4.8.3	Measurements of contact angle (CA)	76
4.8.4	SEM-EDS physical characterization	78
4.8.5	Water Quality Experiments.....	78
4.8.6	Method for flux decline and salt rejection	79
5	Results and discussion	80
5.1	Flux performances	80
5.1.1	The effect of the feed temperature on the extended runs performance of MD. .	80
5.1.2	The effect of the feed flowrate on the extended runs performance of MD.	85
5.2	Investigations of membrane wetting.....	94
5.3	SEM-EDS physical characterization and analysis	103
5.3.1	SEM- EDS analysis for the used membranes at the lower flowrate	104
5.3.2	SEM-EDS analysis at the higher feed flowrate.....	111
5.4	The effect of antiscalant on the extended runs performance of MD.....	118
5.4.1	Investigation of membrane wetting occurrence with added antiscalant.....	122
	SEM-EDS analysis of the used membranes with added antiscalant	124
6	Conclusions and recommendations.....	130

6.1 Conclusions 130

6.2 Recommendations and future work 134

References 136

Appendix A: Antiscalant datasheet..... 151

Appendix B: Salt rejection tables 152

Appendix C: SEM images of the used membrane for experiment code 7015..... 155

Appendix D: SEM images of the used membrane for experiment code 5015 156

Appendix E: EDS for experimental code 6025 157

LIST OF TABLES

Table 1: The thermal conductivities and surface energies of the available membrane materials used for MD applications.....	8
Table 2: Summary of some physical, chemical, and biological characterization of fouled membranes, adopted in MD studies.	53
Table 3: The conductivity and pH of the feed seawater.....	60
Table 4: Properties of the polypropylene membrane used.....	61
Table 5: The specifications of the heater and cooler used.....	69
Table 6: The peristaltic pumps specifications.	70
Table 7: The tubing specifications used in the MD unit.....	70
Table 8: The digital balance specifications.	71
Table 9: The specifications of the thermometer and thermocouples used in the MD system.....	72
Table 10: The specifications of the conductivity meter used.	72
Table 11: The parameters selected with the total operation time of the experimental batches in the lab scale DCMD system.....	74
Table 12: Physical properties of PERFORMAX 3-S200 antiscalant.....	75
Table 13: The operational conditions for the set of experiments with added antiscalant.	76
Table 14: The average fouling rate at the operational conditions employed.	83
Table 15: The virgin flat-sheet polypropylene membrane (0.2 μm) contact angle measurements.	95
Table 16: The measured contact angles at various sites of the fouled membranes operated at different feed temperatures and at a constant feed flowrate of 1.5 L/min.....	95
Table 17: The measured contact angles at various sites of the fouled membranes operated at	

different feed temperatures and at a constant feed flowrate of 2.5 L/min.....	97
Table 18: The salt rejection percentages for all the runs of experiment code 7015.....	98
Table 19: The salt rejection percentages for all the runs of experiment code 6015.....	99
Table 20: The salt rejection percentages for all runs of experiment code 5015.	100
Table 21: The contact angle measurements of the used membrane under the effect of added antiscalant.....	122
Table 22: The contact angle measurements of the used membranes, with and without the addition of antiscalant to the feed.	123
Table 23: The worst-case scenarios before and after the addition of antiscalant.	127
Table 24: Case scenarios with membrane fouling and after the addition of antiscalant.....	128
Table 25: Case scenarios with minimal membrane fouling without the addition of antiscalant.	129

LIST OF FIGURES

Figure 1: DCMD configuration.	4
Figure 2: A schematic diagram of AGMD configuration.	5
Figure 3: A schematic representation of SGMD configuration.	6
Figure 4: VDM schematic configuration.	7
Figure 5: Schematic representation of (a) tubular module, and (b) frame and plate module.	8
Figure 6: (a) The thermal distribution of the DCMD affected by membrane fouling, SEM images of (b) Porous fouling layer of CaCO_3 , (c) Non-porous fouling layer of protein, (c) Unfouled, virgin membrane.	16
Figure 7: The factors influencing fouling formation.	18
Figure 8: Schematic representation of the external fouling and the pore blocking fouling.	19
Figure 9: Schematic diagram representing the mixed fouling mechanisms propensities, where a, b, c and M each present a different form of mixed fouling per the foulants present.	20
Figure 10: A schematic diagram representing the mechanisms of Bulk crystallization, and surface crystallization due to inorganic fouling in MD process.	21
Figure 11: The solubility of different forms of calcium carbonate with respect to temperature.	24
Figure 12: SEM image of CaCO_3 scale morphology on an Accurel PP membrane, using tap water as the feed in a DCMD system.	25
Figure 13: SEM imaging of CaSO_4 during saline wastewater separation in a DCMD process.	28
Figure 14: A schematic representation of the different degrees of membrane wettability. (A) non-wetted (B) surface-wetted (C) partial wetted (D) completely wetted.	32
Figure 15: Water logging mechanism.	34
Figure 16: To the left is SEM image of the cross section of a PVDF membrane after an exposure	

by seawater up to 4 weeks. To the right: a cross section of a PP membrane showing the top portion of the pores after rinsing with HCl.....	35
Figure 17: (a) Cracking (b) salt deposition layer. Both (a) and (b) show PTFE membrane within 2 weeks of seawater exposure under drying conditions.....	38
Figure 18: The effect of increasing temperature on the fouling rate, where the major fouling contributor is CaCO ₃ scale.....	41
Figure 19: The permeate flux profiles obtained at different feed temperatures, using a solution of CaSO ₄ as the feed.....	42
Figure 20: The effect of feed velocity on the fouling rate (% decline in initial flux) at a constant temperature.....	44
Figure 21: The effect of feed velocity on calcium concentration [Ca]%. Where Fb1, Fb2 and Fb3 are 84, 688, and 1438 mL/min, respectively.	45
Figure 22: SEM images of (a) virgin membrane (b) fouled membrane.	54
Figure 23: A diagram showing a liquid droplet with the three-phase forces.	55
Figure 24: (a) SEM image of the membrane (b) The attached EDS spectra showing elemental composition of the fouled layer used tap water as the feed	56
Figure 25: The bench scale DCMD unit setup in the chemical engineering laboratory of QU.	59
Figure 26: The flat-sheet PP membrane used in the MD runs.....	61
Figure 27: The membrane distillation flat-sheet module schematic diagram (dimensions in mm).	63
Figure 28: Presentation of the position of the spacer and membrane coupon in a view diagram of the MD unit.....	64
Figure 29: The inner parts of the bottom and the top plates of the MD unit.	65

Figure 30: The MD unit from outside with the leak-proofing clamping shown.	65
Figure 31: The DCMD module plate dimensions from the outside in millimeters.	67
Figure 32: The MD compartment dimensions from the inside in millimeters.	68
Figure 33: The dimensions of the plates from the sides.....	68
Figure 34: The drop shape analyzer KRUSS DSA25 used for CA measurements.	77
Figure 35: The membrane holder with a sample membrane shown.	78
Figure 36: The flux profiles obtained at $q_f = 1.5$ L/min, where $t_f = 50-70$ °C, and $t_p = 20$ °C.	81
Figure 37: The flux profiles obtained at $q_f = 2.5$ L/min, where $t_f = 50-70$ °C, and $t_p = 20$ °C.	84
Figure 38: The effect of varying the feed flowrate at $t_f = 50$ °C, and $t_p = 20$ °C.....	86
Figure 39: The effect of varying the feed flowrate at $t_f = 60$ °C, and $t_p = 20$ °C.....	88
Figure 40: The effect of varying the feed flow rate at $t_f = 70$ °C and $t_p = 20$ °C.	89
Figure 41: The overall flux decline percentage after 45 hours of operation for $t_f = (50- 70$ °C), $t_p = 20$ °C and $Q_f = 1.5, 2.5$ L/min.	90
Figure 42: Schematic representation of the main three zones of declining flux profile curves....	93
Figure 43: The shape of the deionized droplet and the contact angle on the surface of a virgin flat-sheet PP membrane ($0.2 \mu\text{m}$).	94
Figure 44: The salt rejection percentages for feed temperatures ($50- 70$ °C), at feed flowrates of ($1.5, 2.5$ L/min).....	102
Figure 45: The representative SEM image of a pristine polypropylene membrane ($0.2 \mu\text{m}$) at $\times 50000$ magnification.....	103
Figure 46: SEM images of the fouled membrane (a) The salt deposit layer magnification and (b) at $\times 15000$ magnification, where $t_f = 70$ °C and $q_f = 1.5$ L/min (experiment code: 7015).	105
Figure 47: The EDS spectrum of the identified distinct crystal morphology shown in Figure 46.	

.....	106
Figure 48: SEM images of the fouled membrane surface sites (a), (b), and (c) at x 10000 magnification and their corresponding EDS, where $t_f = 60\text{ }^\circ\text{C}$, $t_p = 20\text{ }^\circ\text{C}$ and $q_f = 1.5\text{ L/min}$ (experiment code: 6015).	107
Figure 49: SEM image at x 2500 magnification of the surface of the fouled membrane, where $t_f = 60\text{ }^\circ\text{C}$, $t_p = 20\text{ }^\circ\text{C}$ and $q_f = 1.5\text{ L/min}$ (experiment code: 6015).	108
Figure 50: SEM-EDS analysis (a), (b), and (c) showing different parts of deposit formed on the surface of the fouled membrane at different high magnifications, where $t_f = 50\text{ }^\circ\text{C}$ and $q_f = 1.5\text{ L/min}$ (experiment code: 5015).	110
Figure 51: The SEM image at low magnification x 1000 for experiment code: 5015.	111
Figure 52: Sample of the SEM-EDS analysis of the fouled membrane surface, where $t_f = 70\text{ }^\circ\text{C}$ and $q_f = 2.5\text{ L/min}$ (experiment code: 7025).	112
Figure 53: SEM image at 2500 x magnification showing the distribution of the deposit layer on the surface of the fouled membrane (experiment code: 7025).	113
Figure 54: The result of the SEM-EDS analysis of the fouled membrane, where $t_f = 60\text{ }^\circ\text{C}$, and $q_f = 2.5\text{ L/min}$ (experiment code: 6025).	114
Figure 55: The SEM image at 1000 x magnification of the fouling layer formed on the surface of the membrane, at $t_f = 60\text{ }^\circ\text{C}$ and $q_f = 2.5\text{ L/min}$. (experiment code: 6025)	115
Figure 56: SEM-EDS analysis at 10000 x magnification of the fouled membrane surface, where $t_f = 50\text{ }^\circ\text{C}$ and $q_f = 2.5\text{ L/min}$ (experiment code: 5025).	116
Figure 57: SEM image at a low magnification to give an indication on the distribution of the fouling layer on the surface of the membrane (experiment code: 5025).	117
Figure 58: The permeate flux obtained at $t_f = 60\text{ }^\circ\text{C}$, $t_p = 20\text{ }^\circ\text{C}$ and $q_f = 1.5\text{ L/min}$, without (6015)	

and with added antiscalant (6015 A)	119
Figure 59: The permeate flux obtained at $t_f = 60\text{ }^\circ\text{C}$, $t_p = 20\text{ }^\circ\text{C}$ and $q_f = 2.5\text{L/min}$, without (6025) and with added antiscalant (6025A).....	120
Figure 60: The permeate flux obtained at $t_f = 70\text{ }^\circ\text{C}$, $t_p = 20\text{ }^\circ\text{C}$ and $q_f = 1.5\text{L/min}$, without (7015) and with added antiscalant (7015 A).....	121
Figure 61: The salt rejection percentages with and without the addition of antiscalant to the feed.....	124
Figure 62: The SEM images of used membranes at x 2000 magnification with added antiscalant to the feed.	125
Figure 63: The SEM image at 1000x magnification of the used membrane after applying antiscalant to the feed.....	126

Nomenclature

A	constant in Antoine equation (dimensionless)
B	constant in Antoine equation (dimensionless)
B _g	pore geometric factor (dimensionless)
C	constant in Antoine equation (dimensionless)
C _m	overall mass transfer coefficient for water vapor through the membrane (kg/m ² s Pa)
d	pore diameter (m)
D _{AB}	diffusivity of water vapor in air(m ² /s)
h ₁	convective heat transfer coefficient at the feed side (W/m ² k)
h ₄	convective heat transfer coefficient at the permeate side (W/m ² k)
J	mass flux (kg/m ² h)
k ₂	thermal conductivity of the biofouling layer (W/ mK)
k _m	effective thermal conductivity of the microporous membrane (W/mK)
K _{sp}	solubility product constant
M _A	molecular weight (kg/kmol)
p	total pressure for volatile component transport (Pa)
p _{fm}	partial vapor pressure at the membrane surface of the feed side (Pa)
p _{pm}	partial vapor pressure at the membrane surface of the permeate side (Pa)
P _{Pore}	air pressure in the pore (kPa)
P _{Process}	liquid pressure on either side of the membrane (kPa)
q _f	flowrate of the feed side (L/min)
R	universal gas constant (J/mol K)
R ₁	convective heat transfer resistance at the hot feed (K m ² /W)

R_{12}	effective resistance of the resistances R_1 and R_2 in series (Km^2/W)
R_{124}	effective resistance of the resistances R_1 , R_2 , and R_4 in series (Km^2/W)
R_2	conductive heat transfer resistance associated with the fouling layer (Km^2/W)
R_3	effective heat transfer resistance associated with the resistances (R_m , R_v) in the membrane ($\text{m}^2 \text{K}/\text{W}$)
R_4	convective heat transfer resistance at the cold permeate (Km^2/W)
R_m	conductive heat transfer resistance accompanying porous membrane (Km^2/W)
R_t	total heat transfer resistance(Km^2/W)
R_v	pseudo heat transfer resistance accompanying with water vaporization (Km^2/W)
SI	Saturation Index
T	Kelvin temperature (K)
t_f	bulk temperature at the feed side(K)
t_{fi}	temperature at the interface of fouling layer/feed side water (K)
t_{fm}	temperature at the membrane surface of the feed side (K)
T_m	mean temperature within the membrane (K)
t_p	temperature of the bulk at the permeate side(K)
t_{pm}	temperature at the membrane surface of the permeate side (K)
δ_m	membrane thickness (m)
ϵ	porosity of the membrane
θ	contact angle of the surface of the membrane (deg.)
λ	heat of water vaporization ($\text{W.s}/\text{kg}$)
τ	membrane tortuosity
σ	solution surface tension (N/m or kg/s^2)

1 Introduction

The demand for fresh water worldwide is increasing gradually along with its supply. Seawater desalination is considered to be the most reliable way to produce fresh water [1]. The available technologies can be divided into two broad categories: the distillation systems and membrane systems. The distillation methods such as the multi stage flash (MSF) uses a relatively inexpensive sources of thermal energy supply to produce high purity water [2]. However, the cost of the facilities required is high. The common known membrane technologies used in industry such as reverse osmosis (RO) require expensive membranes and associated pretreatment units to separate the brine from the pure water conducted under more compact and less demanding facilities. Nevertheless, high energy source is required in terms of high electrical power supply to achieve high feed pressure. In general, these technologies are energy intensive desalination processes and associated with negative environmental impact in the form of CO₂ emissions. Membrane distillation (MD) is an emerging technology that has been under research and development since the 1990s [3]. MD is a thermally-driven process used mainly for desalination purposes. Other uses of MD include, the concentration of various types of aqueous solutions [4, 5], the separation of heavy metals from contaminated water or the removal of volatile organic compound traces [6, 7]. MD process operates by allowing only vapor to pass through a barrier layer consisting of a micro-porous hydrophobic membrane, by utilizing low grade thermal energy [8]. Water vapor diffuses through the pores of the membrane from the feed-pore interface, then depending on the MD configuration it is collected or condensed by different means at the permeate side [9]. There are mainly four configurations of MD that can be employed, including: direct contact membrane distillation, vacuum, sweep gas, and air gap [10].

One of the important factor the MD process relies on is the design and structure of the membrane. The characteristics of a good quality MD membrane is in compromise between membrane permeability and

its resistance to wettability [8]. These characteristics include adequate thickness, high porosity, narrow uniform pore size distribution, and high hydrophobicity [8]. Due to some issues including its production of relatively low permeate flux when compared to RO, concentration and temperature polarization and fouling of the membrane will lead to further reduction in the permeate flux [2, 11], and membrane damage along with loss of hydrophobicity in long-term performance [12]. In recent years, many studies were conducted for the purpose of improving the structure and design of the fabricated MD membrane including flat-sheets and hollow fiber membranes, to achieve high permeate fluxes and salt rejection what makes MD more viable for many uses [13-15].

Nevertheless, MD process has advantages over conventional desalination processes including the thermally-driven systems such as flash distillation, and the pressure-driven systems such as reverse osmosis. RO demands heavy gauge piping and requires high maintenance, which is not the case in MD since it is thermally-driven. Moreover, MD is less prone to fouling than RO [16] since only vapor crosses through the membrane, and theoretically MD is capable of 100% rejection of macro-particles and ions [9]. Compared to thermally-driven systems, MD requires lower temperature, and so waste heat of low-grade in addition to solar and geothermal energy sources can be utilized [8]. MD technology has less parts requirement and can be run in a relatively smaller footprint because of its lower vapor space [10].

Although, MD is a promising technology over other desalination technologies, it is not yet fully commercialized, thus significant advancements should be done for MD technology to achieve growth in market shares [17]. Despite that MD is less prone to fouling than RO, it is one of the issues that affects the life time and performance of the MD process. Many studies have pointed out and detailed fouling existence and its control approaches in reverse osmosis, nano-filtration and ultrafiltration [18-22]. However, compared to MD the behavior of fouling is different, since the applied pressure in RO is much higher than that applied in an MD process. Moreover, only vapor and not the solution of the feed enters the pores of the membrane, hence the chemical interactions between the feed solution and the

membrane will not be the same as in the membrane filtration pressure-driven processes [10]. It is imperative to reveal that numerous studies have been conducted on the scaling and fouling of the membrane in typical laboratory MD processes, but no studies was conducted to explicate this knowledge [23].

Since the operational conditions and the membrane properties in MD are different compared to pressure-driven processes and in order to maintain MD efficiency, it is important to understand fouling mechanisms and to suggest control strategies [8]. The development of fouling control techniques in MD is vital not only in reducing the contaminated permeate production as a result of pores wetting induced by fouling, but also to reduce the costs of consumed energy, membrane area, replacement requirements, and shutdown periods [24, 25].

1.1 Objective and scope of work

In order to deploy membrane distillation desalination commercially, it is important to address outstanding issues such as membrane fouling and suitable mitigation methods. Therefore, it is the objective of this work to investigate:

- The effect of temperature and flowrate on the membrane fouling behavior.
- The effect of antiscalant addition.

These objectives will be attained through analysis of flux performance and membrane autopsy using a variety of tools such as SEM-EDS, contact angle, and salt rejection.

2 Membrane distillation

Membrane distillation desalination process is unlike other membrane based processes that depend on the pressure differences or gradients of concentration or electrical potential. MD is a thermal membrane-based separation process, where the driving force is a temperature induced vapor pressure difference through a micro-porous hydrophobic membrane. Vapor crosses the membrane by means of simultaneous mass and heat transfer from the hot feed to the cold permeate side.

2.1 MD configurations

2.1.1 Direct contact membrane distillation (DCMD)

DCMD is aimed to be employed widely in desalination, the manufacture of acids, and in food industries for aqueous solutions concentration [26-28]. It is considered as the simplest configuration of MD amongst others, where the feed is in direct contact with the surface from the hot side of the membrane. The vapor pressure difference is the driving force that moves the vapor through the pores of the hydrophobic membrane into the permeate cold side where it condenses in the membrane module (Figure 1). The main disadvantage of this configuration is heat losses due to conduction, reducing the overall thermal efficiency [13].

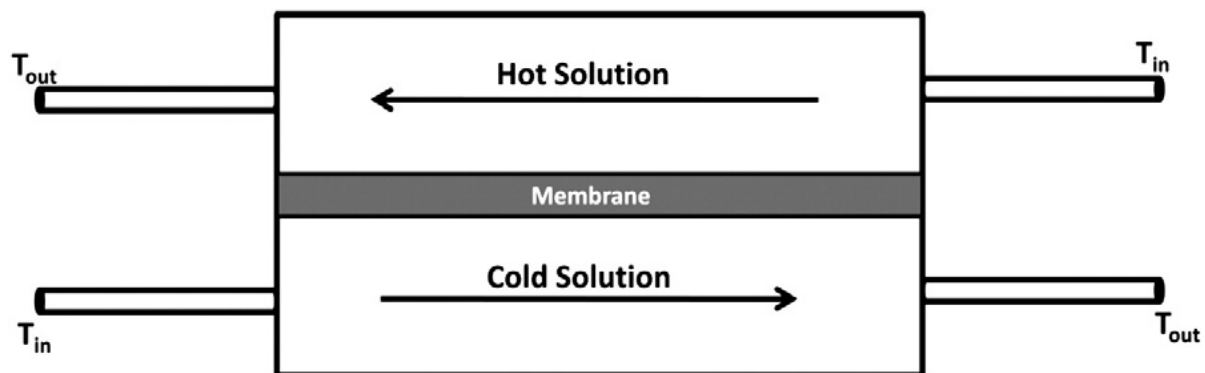


Figure 1: DCMD configuration [13].

2.1.2 Air-gap membrane distillation (AGMD)

AGMD configuration is suitable for desalination purposes and the condensation of volatile compounds traces in aqueous solutions [29, 30]. The hot feed is in direct contact only with the surface of the membrane. In the permeate side a stagnant air is interposed between the cold surface and the membrane, where condensation of the vapor passing across the air gap takes place inside the membrane unit (Figure 2). Thus, the driving force is the temperature difference in the liquid-vapor interface of the hot feed with the condensing surface [13]. One disadvantage of this configuration is the mass transfer resistance added because of the presence of air gap. Yet, it promotes reduced heat losses due to conduction [13].

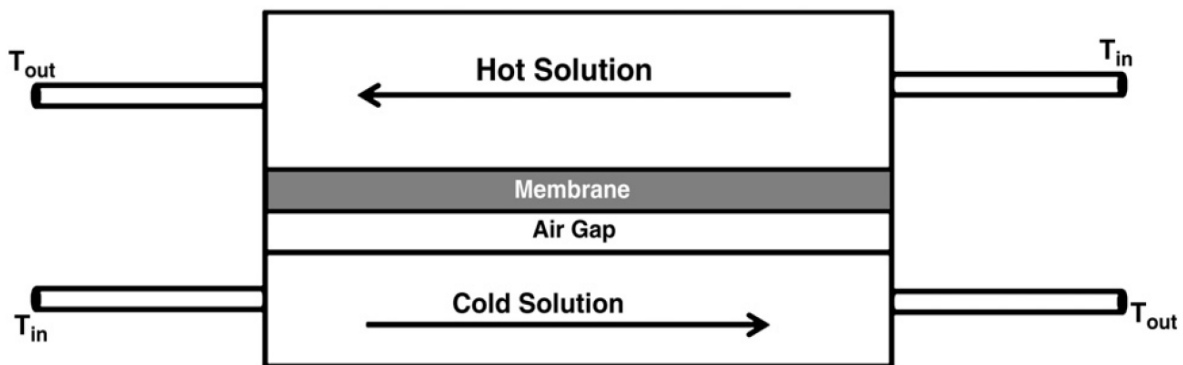


Figure 2: A schematic diagram of AGMD configuration [13].

2.1.3 Sweeping gas membrane distillation (SGMD)

In this configuration, the vapor condensation takes place outside the membrane module, by sweeping inert gas at the permeate side (Figure 3). Similar to AGMD, gas barrier is present thus, the conduction heat losses are reduced. However, the coefficient of mass transfer is enhanced since this barrier is not stationary. One drawback of this configuration is the requirement of large condenser, since large volume

of sweep gas is needed to diffuse only a small volume of permeate [13]. The AGMD process is suitable for the removal of volatile compounds from aqueous solutions.

It is worthwhile mentioning the development of a combined process known as the thermostatic sweeping gas membrane distillation (TSGMD). It functions by passing an inert gas across the gap between the cold condensation surface and the membrane. The condensation of vapor takes place over the surface of condensation (AGMD), while the remaining part is condensed in an exterior condenser outside the membrane module (SGMD) [3, 31].

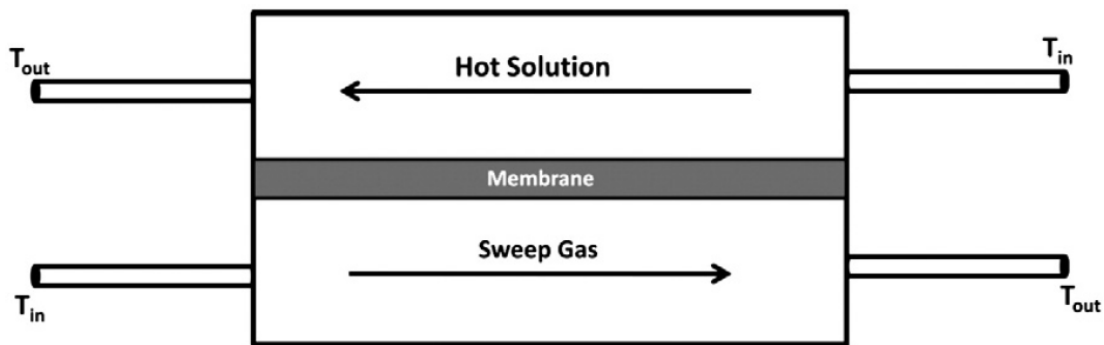


Figure 3: A schematic representation of SGMD configuration [13].

2.1.4 Vacuum membrane distillation (VMD)

A pump is used in VMD configuration in the permeate side of the membrane to create a vacuum and the vapor condenses outside the membrane cell (Figure 4, excluding the vapor condensation unit). VMD has a negligible conduction heat losses, which is considered as a great advantage [10]. VMD is suitable for the separation of volatile aqueous solutions [32, 33].

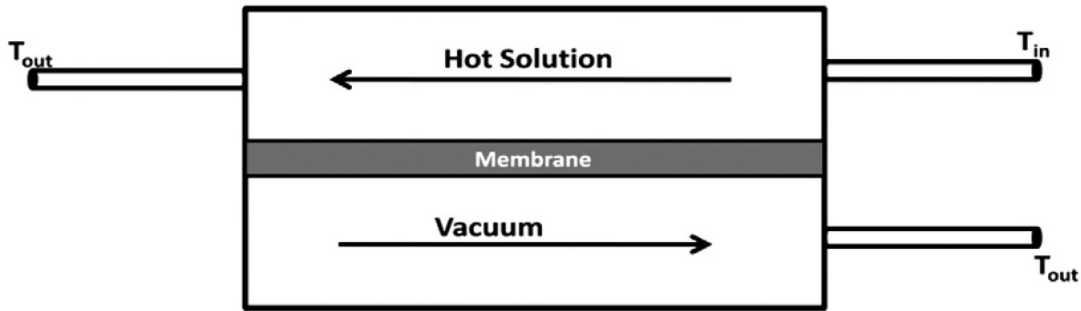


Figure 4: VDM schematic configuration [13].

2.1.5 Module configurations and membrane materials

The two main configurations of MD module used are the frame and plate module, and the tubular module. In tubular hollow fiber module (Figure 5a), the feed passes through the shell side where the membranes are implemented, while the permeate is applied on the other side of the hollow fiber. Depending on the configuration DCMD, SGMD, or VDM, coolant, sweeping gas, or negative pressure is applied, respectively. The packing density of this configuration is high ($3000 \text{ m}^2/\text{m}^3$) [33,37]. The other module configuration is the frame and plate (Figure 5b), where flat-sheet membranes can be used in any of the MD configurations discussed in section 2.1. The packing density is less than that of tubular module around $100\text{-}400 \text{ m}^2/\text{m}^3$ [10,33]. However, the effective area to volume can be increased by constructing multiple layers' flat sheet membranes, and the dynamics of the flow can be enhanced by adding a spacer that promotes flow turbulence [34]. As the configuration suggests, it is easier to replace the damaged MD membranes in the frame and plate module. Moreover, a better distribution of flow can be accomplished implying a lower degree of temperature polarization than that in hollow fiber module [34]. Accordingly, this module configuration was more employed in a laboratory scale to examine the effect of various membrane properties and operational conditions on the performance of MD process [35].

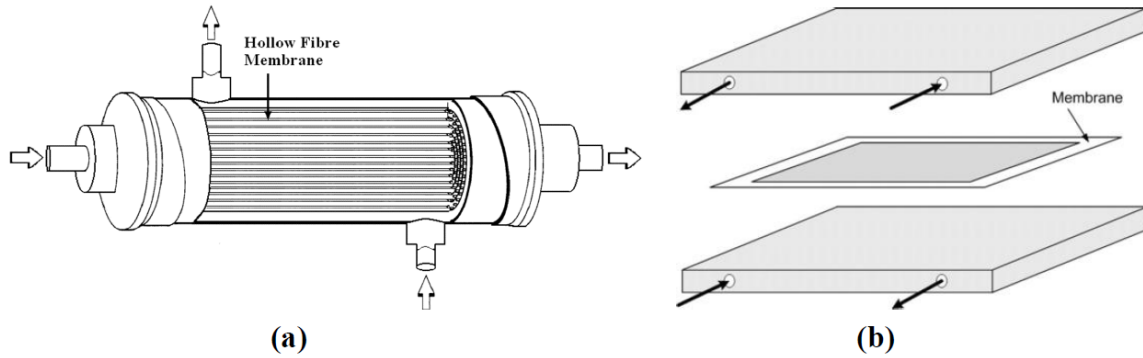


Figure 5: Schematic representation of (a) tubular module, and (b) frame and plate module [34].

The most common membrane materials used in MD applications include: polypropylene (PP), polytetrafluoroethylene (PTFE), and polyvinylidene fluoride (PVDF) [53]. The commercially available membranes have porosity range of 0.60 to 0.95, thickness of 0.04 to 0.25 mm, and size of pore of 0.2 to 1 μm [34]. The surface energies and thermal conductivities of these materials are presented in Table 1.

Table 1: The thermal conductivities and surface energies of the available membrane materials used for MD applications [35, 36].

Membrane material	Thermal conductivity (W/mK)	Surface energy ($\times 10^{-3}$ N/m)
PP	~ 0.17	30
PTFE	~ 0.25	9-20
PVDF	~ 0.19	30.3

2.1.6 Membrane characteristics

The membrane acts as a barrier layer, where its properties selectively prompt the transport of heat from the feed to the permeate side, the vapor phase is transferred through the inorganic or microporous polymeric membrane allowing the simultaneous exchange of heat and mass at the interfaces based on a vapor-liquid equilibrium [34]. The characteristics of membrane applicable for membrane distillation uses, include [37-40]:

- Optimum thickness in compromise between mass and heat transfer. While, high mass transfer can be achieved by a thicker membrane, a lower thermal resistance leads to an increase in the driving force for a thinner membrane to produce a higher flux.
- Low thermal conductivity of the membrane material, since low conductivity reduces the loss of sensible heat through the membrane that leads to a higher permeate flux production by increasing the temperature difference at the membrane interface.
- Relatively large pore size ranging from several nanometers to few micrometers with a narrow distribution such that the liquid entry pressure (LEP) is not exceeded.
- Low surface energy, implying a higher hydrophobicity of the membrane. Where the membrane with higher hydrophobicity can withstand higher pressure with the same pore size. In other words, according to equation (1), more hydrophobic material allows MD operation with a membrane of larger pore size under the same pressure.
- High porosity, where the porosity is defined as the fraction volume of the voids that allow the production of vapor flux, regardless of the configuration of MD.
- Exhibits good long term thermal stability handling temperature as high as 100 °C, and stable performance of MD in terms of selectivity and permeability.

Liquid entry pressure is the liquid entry pressure above which the water is able to penetrate the membrane's pores, causing wetting [8]. The transmembrane pressure should be as high as possible to avoid the entry of liquid from the feed or the distillate side by overcoming the hydrophobic forces of the membrane. LEP depends on many factors, such as the water's surface tension, the surface energy of the membrane's material, and the geometry and distribution of the pores [8]. LEP can be calculated using Laplace-Young equation, as following [13]:

$$LEP = \frac{(-4B_g \sigma \cos \theta)}{d_{max}} < P_{process} - P_{pore} \quad (1)$$

Where B_g is the geometric factor of pore, and is equal to 1 for cylindrical geometry of the pores. σ is the solution's surface tension, θ is the angle of contact between the surface of the membrane and the solution, and d_{max} is the diameter of the largest pore. Where the pressure difference of the liquid in either side of the membrane and the air in the pores of the membrane should be greater than the designed LEP [34]. To avoid membrane wettability, the hydrophobicity of a membrane's material can be increased by increasing the contact angle, in which a higher value of LEP can be achieved, or by decreasing the size of the pores to a small maximum pore size limited by membrane permeability, promoting a better performance of MD [34]. However, besides wetting of the membrane taking place due to many factors such as the presence of surfactants, it should be noted that the major contributor to membrane wetting is induced by fouling and scaling [41].

2.2 Theoretical background

During the operation of MD heat and mass transfer takes place simultaneously. Moreover, the dominant resistance across the membrane depend on the flow regime, wherein at high flowrates the mass transfer resistance of the membrane is predominant, while at lower flowrates the rate limiting step across the boundary layer is the resistances of heat transfer [2, 3]. One of the issues that affects the life time and performance of MD process is fouling by adding heat resistance to the MD process, that will be addressed in this section.

2.2.1 Mass transfer

The vapor partial pressure gradient is the driving force in MD. The mass transfer transmembrane flux, is expressed as [42]:

$$J = C_m(p_{fm} - p_{pm}) \quad (2)$$

Where J is the flux of mass transfer, C_m is the overall coefficient of mass transfer, and p_{fm} and p_{pm} are the vapor-liquid feed and permeate partial vapor pressures, respectively [42].

The vapor pressure is exponentially related to temperature difference as predicted from Antoine's equation [10].

$$p = e^{(A - \frac{B}{C+T})} \quad (3)$$

Thus, the higher the temperature difference in the vapor-liquid interface of the membrane from the distillate and feed sides [23], the higher the driving force which leads to an increase in flux of the permeate. Per Knudsen-molecular diffusion model, equation (3) can be expanded as following [43]:

$$J = \frac{\varepsilon}{\tau\delta} \frac{pD_{AB}}{RT_m} \ln \frac{(p - p_{pm})/pD_{AB} + (\frac{3}{4d})\sqrt{2\pi M_A/RT_m}}{(p - p_{fm})/pD_{AB} + (\frac{3}{4d})\sqrt{2\pi M_A/RT_m}} \quad (4)$$

All the factors that influence the flux of DCMD are included in this equation, such as the characteristics of the membrane ($\varepsilon, \tau, \delta, d$), the feed and permeate (p_{pm}, p_{fm}) temperatures, transported components' molecular weight (M_A) and diffusivity (D_{AB}), and the membrane module fluid dynamics and properties [44].

The temperature at the feed and permeate surfaces of the micro-porous membrane influences the vapor pressure by its polarization effects. The fouling layer formed at the surface adds an additional heat transfer resistance to the vapor pressure at both surfaces of the membrane; specifically fouling layers formed due to inorganic foulants and humic materials that are found to be porous [12]. Moreover, according to recent studies not only heat transfer resistance is added, but also hydraulic resistance when the fouling layer formed has small pores (< 50 nm) or gel-like free volume hydrophilic layer of fouling that will cause further reduction in the driving force due to the depression in vapor pressure. The water in liquid form may pass

through this layer by capillary action forming another liquid/vapor interface. This phenomenon is known as Kelvin effect which was not incorporated in the model of mass transfer [45]. However, the surface resistance is negligible since the area of the pores in MD is larger than the area of the surface [35].

2.2.2 Heat transfer

The thermal resistance in process transport is used to analyze the heat transfer in MD operation. Excluding the effect of fouling, three main sections are involved in heat resistance: The resistance of the membrane and the resistance of the hydrodynamic feed and permeate boundary layers. Additionally, in the presence of fouling layer a further heat transfer resistance is induced. Each heat transfer step contributes to a certain resistance and driving force. However, all the steps have equal transfer of heat under steady state conditions. The heat transfer at steady state is described as follows [11, 44]:

$$q = \frac{t_1 - t_{fl}}{R_1} = \frac{t_{fl} - t_{fm}}{R_2} = \frac{t_{fm} - t_{pm}}{R_3} = \frac{t_{pm} - t_p}{R_4} = \frac{1}{R_t} (t_f - t_p) \quad (5)$$

Where,

$$R_1 = \frac{1}{h_1} ,$$

$$R_2 = \frac{\delta_2}{k_2} ,$$

$$R_3 = \frac{1}{\frac{1}{R_m} + \frac{1}{R_v}} = \frac{1}{\left(\frac{k_m}{\delta_m}\right) + \lambda C_m \left(\frac{dp}{dT}\right)_{T_m}}$$

$$R_4 = \frac{1}{h_4}$$

R_1 and R_4 represent the feed and permeate hydrodynamic boundary layers' heat transfer resistances, respectively. R_2 is the conductive heat of the fouling layer, and R_3 is the resistance corresponding to the parallel resistances of the membrane's conduction heat, taking into account the pores and the solid portions. Figure 6a schematically describes the thermal resistances discussed. R_t is the heat transfer total resistance from the feed to the permeate. The temperatures at the membrane interface of the feed and

permeate (t_{fm} and t_{pm}) can be determined from equation (5) solution, as follows [11]:

$$t_{fm} = t_f - \frac{(R_1 + R_2)(t_f - t_p)}{R_3 + (R_1 + R_2 + R_4)} = t_f - \frac{R_{12}(t_f - t_p)}{R_3 + R_{124}} \quad (6)$$

$$t_{pm} = t_p - \frac{R_4(t_f - t_p)}{R_3 + R_{124}} \quad (7)$$

The relation of the known difference in temperature ($t_f - t_p$) with the unknown temperature difference ($t_{fm} - t_{pm}$), can be described as [11]:

$$t_{fm} - t_{pm} = \frac{R_3(t_f - t_p)}{R_3 + (R_1 + R_2 + R_4)} = \frac{R_3(t_f - t_p)}{R_3 + (R_{124})} \quad (8)$$

2.3 Temperature polarization (TP)

Temperature polarization phenomenon is known to have a significant influence on MD performance. The latent heat of evaporation is removed when the water evaporates through the pores of the membrane. Near the membrane surface a thermal boundary layer is formed due to the cooling process. The MD driving force drops dramatically as a result of temperature reduction, since the water vapor pressure decreases exponentially with temperature [9], leading to a higher degree of flux decline.

The effective heat transfer coefficient is the factor that determines the temperature polarization extent, at a given flux. A higher heat transfer coefficient is required to minimize the temperature difference required to transfer the same amount of vaporization heat across the thermal boundary layer. Thus, MD design strategies aim to increase the feed side heat transfer coefficient to reduce the temperature polarization effects by increasing the feed flowrate, trying to operate under turbulent regimes or adding spacer in the MD module to promote turbulence [9]. Equation (9) [46] present a simple temperature polarization model:

$$T_{f,b} - T_{f,m} = \frac{q_{out}}{h} \quad (9)$$

Where q_{out} is the total loss of heat across the membrane, where vapor sensible heat transfer and evaporation latent heat are included, h is the heat transfer coefficient, and $T_{f,b}$ and $T_{f,m}$ are the

temperatures at the bulk in the feed stream and the membrane interface, respectively.

In addition to vapor flux reduction, temperature polarization may lead to the reduction in scaling potential, because the solubility of some salts is inversely proportional with temperature. Nevertheless, concentration polarization may rise under similar conditions at which temperature polarization rises; increasing the potential of scale formation, due to increased salt concentration near the surface of the membrane [9].

2.4 Concentration polarization (CP)

The MD system operates by allowing only water vapor to pass through the membrane, increasing the concentration of non-volatile salts and creating a film at the vapor/liquid interface of the membrane this is referred to as concentration polarization. The film model is used to describe the concentration polarization process, depicted by equation (10) [3].

$$\frac{x_m}{x_c} = \exp\left(\frac{J}{\rho k}\right) \quad (10)$$

Where x_m is the membrane surface molar concentration and x_c is the fluid streams bulk molar concentration, J is the flux of water through the membrane and k is the coefficient of mass transfer of the salt in the solution.

It should be noted that the influence of concentration polarization is indirect and insignificant on the driving force of the MD process, when compared to the influence of temperature polarization on the vapor pressure difference. The significance of the concentration polarization effect arises due to the promotion of scale formation as a result of increased concentration at the membrane interface. As described in Eq. (10) an increase in the flux J causes an increase in the concentration polarization effect, while this effect is reduced with an increase in the mass transfer coefficient. Nevertheless, concentration and temperature polarizations take place simultaneously and both phenomena influence and depend on vapor flux of water through the membrane [9]. Details of fouling and scaling mechanisms will be elaborated in chapter 3.

3 Membrane Distillation Challenges: Fouling, scaling and wetting (including membrane autopsies, and state of art)

3.1 Fouling in membrane distillation

In general, fouling can be defined as the accumulation of deposits on the membrane's surface or within its pores that leads to the reduction in the permeation flux and the degradation in the performances of salt rejection, inducing wetting [47, 48]. Wetting will be discussed further in section 3.4.1.

All the fouling sorts found in other membrane-based separation processes take place in MD. Generally, the formation of deposit occurs due to the interaction of foulants; that are of colloidal nature amongst them or/and amongst the membrane surface [49].

Hydraulic and thermal resistances rise in the presence of a fouling layer, depending on its thickness and porosity [50]. If the layer of fouling was porous (Figure 6b) it may contribute to thermal resistance by observing a decrease in the flux of permeate only. However, if it was non-porous (Figure 6c) it increases both types of resistance, with a higher influence on the mass transfer resistance by hindering the water vapor transport across the membrane [8]. Temperature polarization effect is increased, due to the drop-in temperature difference across the membrane passing through the fouling layer, leading to further reducing in the driving force of MD process [1]. The tendency and intensity of fouling depend on the type of feed solution used, as investigated by Gryta [12] in which he studied the effect on PP capillary membranes using DCMD system by feed solutions of brines, proteins from wastewater and demineralized water production. While brine feed contributed to a porous fouling layer of CaCO_3 scale, wastewater caused the formation of a non-porous layer of protein fouling, as shown in the SEM images in Figure 6, where Figure 6d represents an image of a virgin unfouled membrane.

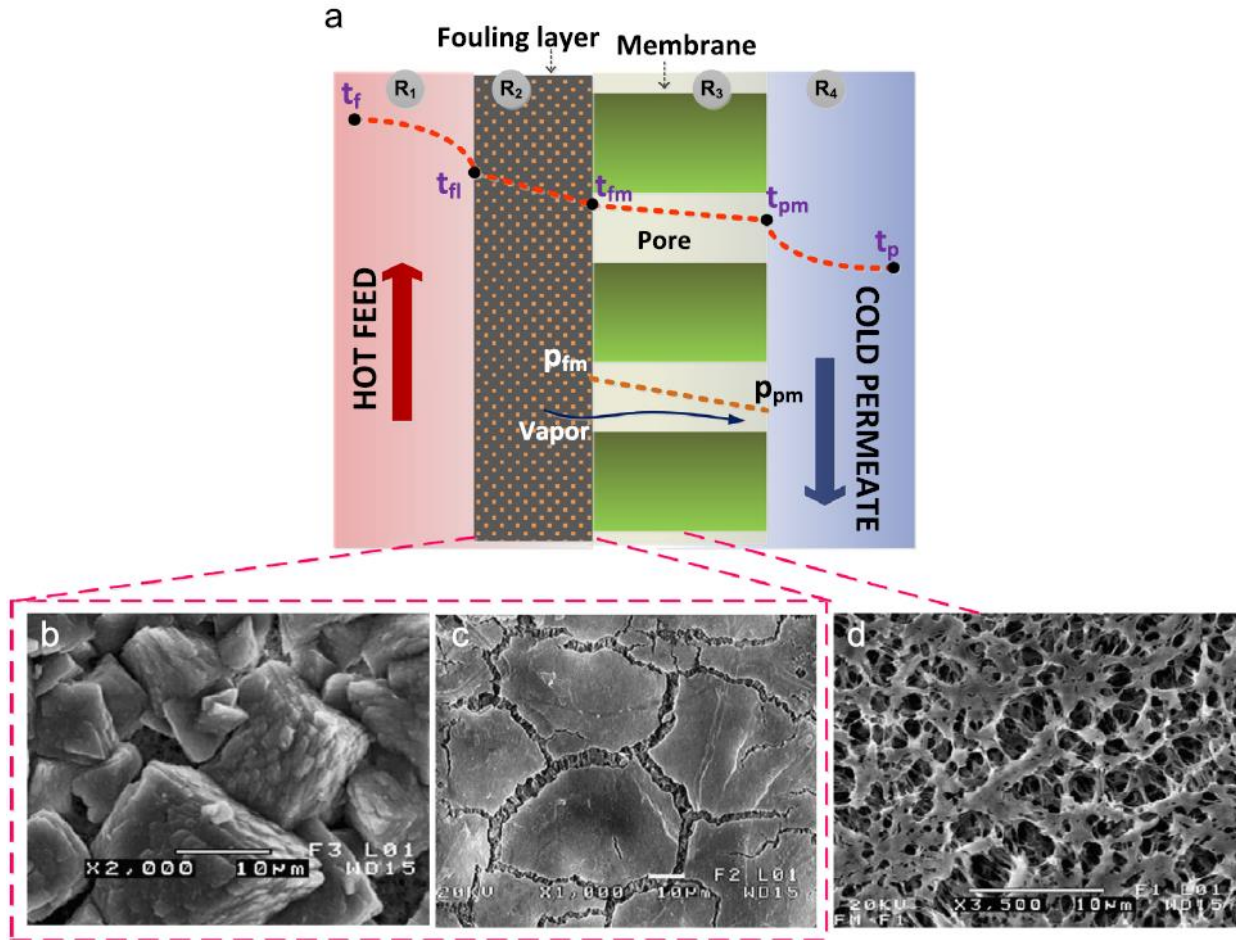


Figure 6: (a) The thermal distribution of the DCMD affected by membrane fouling, SEM images of (b) Porous fouling layer of CaCO_3 , (c) Non-porous fouling layer of protein, (d) Unfouled, virgin membrane [8].

The mechanisms of fouling in membrane distillation are disparate compared to that encountered in membrane pressure-driven processes, due to the differences in the properties and pore size of the membranes used, in addition to the effect of operational parameters. According to previous studies [12, 48, 51], it was found that fouling due to CaCO_3 and protein depositions were more critical under the effect of the elevation of feed solution temperatures, at which the MD processes operate. Moreover, the feed flowrate effect on the fouling rate and the deposit size and morphology, was studied. It was found that

while, increasing the flowrate of the feed led to the formation of porous fouling layer of smaller crystals, lowering the flow rate caused the production of thicker fouling layer with a mountain-like structure of deposition [12].

The complication of fouling phenomenon arises from the fact that it is influenced by many factors and can form on the surface or within the pores of the membrane, understanding the mechanism at which fouling takes place is essential in developing approaches for fouling remediation and cleaning [8]. These factors can be divided into four groups [18], as shown in Figure 7: (a) The characteristics of the foulants (solubility, charges, concentration, diffusivity, etc.); (b) properties of the membrane (pore size and its distribution, hydrophobicity, roughness of the surface, it's charges and functional groups); (c) operational parameters (temperature, and flowrate); and (d) the characteristics of feed water (pH, organic and/or inorganic occupation, ionic strength and the chemistry of the solution). The membrane surface fouling is mainly influenced by the foulant characteristics, while membrane properties mainly affect the interactions of the surface of membrane with the foulant [8]. Moreover, the operational conditions of MD process influence the propensity and intensity of fouling.

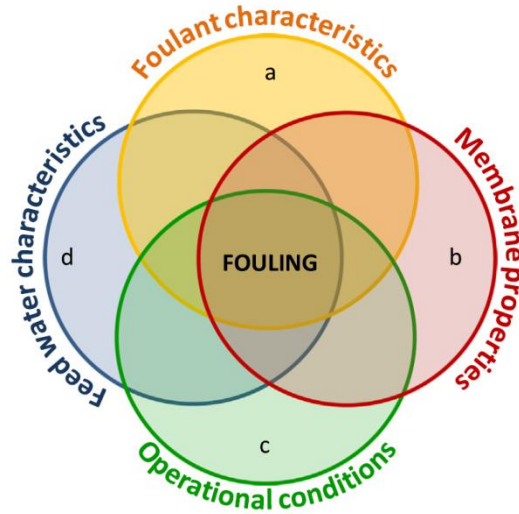


Figure 7: The factors influencing fouling formation [8].

The fouling sites can be at the external surface or blocking the pores of the membrane (Figure 8) [52]. The formation of deposit (gel-like) layers on the feed-membrane interface is referred to as external fouling this type of fouling is considered to be reversible by simple cleaning methods. Whereas, pore blocking fouling takes place when the foulants penetrate the surface of the membrane into its pores causing partial pore blockage by narrowing the pores gradually, or complete blockage by penetrating the full pores' depth [53]. Accordingly, pore blockage induced fouling in most cases is irreversible, as result of membrane degradation and permanent damage [8]. According to the study performed by Gryta [12] on DCMD system, it was observed in a microscopic level that fouling did not take place only on the surface of the membrane, but also within the pores, causing an irreversible damage of the membrane.

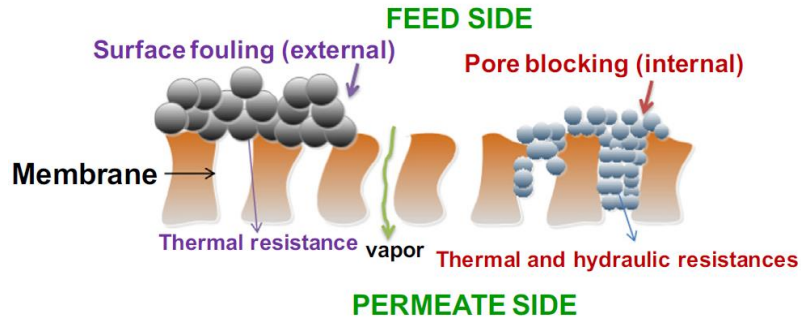


Figure 8: Schematic representation of the external fouling and the pore blocking fouling [8].

In accordance with the material of the fouling layer, there are three main broad categories of foulants found in MD technology studies [54], including: (a) inorganic, (b) organic, and (c) biological fouling. Where the colloidal particles and particulates deposition such as slit, clay, silica take place and/or precipitation and crystallization of hard minerals from the feed solution such as CaCO_3 , CaSO_4 , NaCl , iron oxide, BaSO_4 , silicate, etc. The deposition of organic matters such as proteins, humic and fulvic acids, polymers of polycrylic cause organic fouling. While Biological fouling, is due to the presence of microorganisms from sources such as fungi, algae, sludge, yeast, and bacteria. It is important to note that what makes fouling an even more complicated phenomenon is the fact that not only one mechanism take place in real MD process, instead a combination of variety of foulants and fouling mechanisms may occur simultaneously [8], as described in Figure 9. However, in real seawater the main concern is inorganic and particulate fouling.

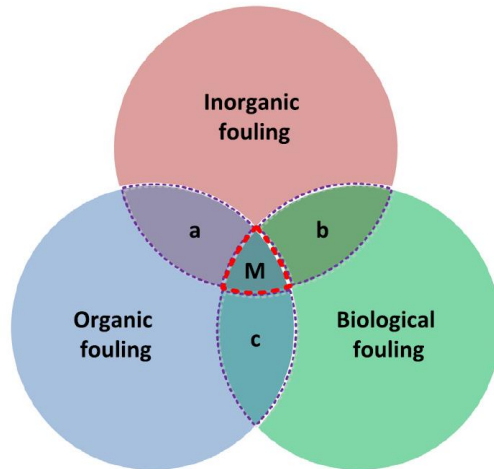


Figure 9: Schematic diagram representing the mixed fouling mechanisms propensities, where *a*, *b*, *c* and *M* each present a different form of mixed fouling per the foulants present [8].

3.1.1 Inorganic fouling

In general, inorganic fouling is referred to deposition and scaling by the precipitation of hard mineral salts from the feed solution involving transport and crystallization phenomena. As mentioned previously also colloidal particles, silica and slit precipitates, products of corrosion, etc. all affect inorganic fouling significantly. When the equilibrium product of solubility becomes less than the ionic product of a salt, scaling starts to form [48]. At the membrane surface near the feed side, due to water vaporization allowing supersaturation condition to take place, causing crystals growth and nucleation [55]. The fouling intensity can be determined by the consideration of kinetics of precipitation along with the conditions of supersaturation [21].

Crystals that nucleate on the surface of the membrane is termed as surface heterogeneous crystallization, on the other hand crystals nucleating in the bulk is known as homogeneous bulk crystallization [56] (Figure 10). Usually these two mechanisms in MD process occur simultaneously. Furthermore, the crystallization starts in the larger pores of the membrane, as they are more susceptible to wetting compared with small

pores [57]. As a consequence of supersaturation conditions, a higher tendency of secondary crystallization of ions and precipitated particles to collide with each other's in the bulk due to transport of particles or/and gravitational settling mechanisms [58, 59]. As a result of the formation of fouling layer on the surface, the driving force across the membrane is reduced resulting in a reduced permeation flux due to the additional temperature polarization caused by increased thermal resistance at the membrane interface [60].

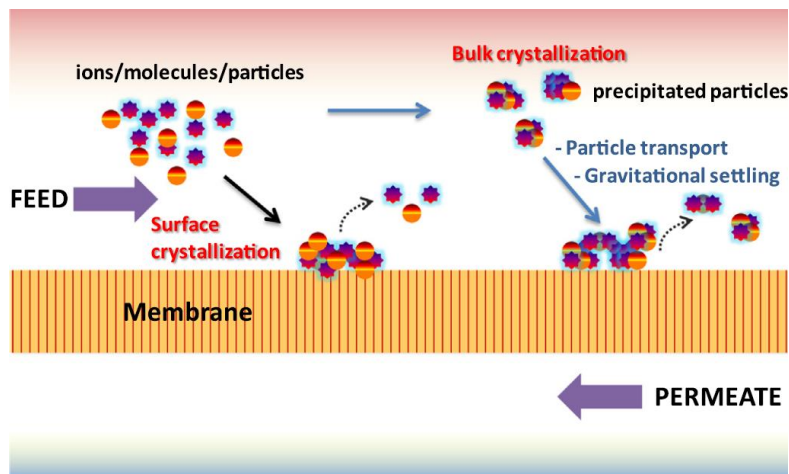


Figure 10: A schematic diagram representing the mechanisms of Bulk crystallization, and surface crystallization due to inorganic fouling in MD process [8].

The most common inorganic scale foulants in membrane distillation are calcium carbonate, calcium sulfate, calcium phosphate and silicate [61]. Other common foulants include ferric oxide, iron oxide, magnesium sulfate, magnesium chloride, barium sulfate, and strontium sulfate [62].

There are many factors that affect the rate of inorganic fouling induced by scaling, including: the supersaturation degree, the temperature of both the surface of the membrane and the solution, the properties of the surface such as its morphology and roughness, the properties of water, the types of

substrate present, and the availability of nucleation sites such as water impurities and particulates [63, 64].

3.2 Inorganic scaling in membrane distillation

Inorganic scaling was studied in MD fouling and reported in the literature. Inorganic scaling, or simply scaling can be divided into three categories, as also classified in RO: alkaline, non-alkaline and particulate scaling [19, 24, 65]. Alkaline salts, is known also as basic salts, will be easily formed when hydrolyzed in a solution increasing the pH above 7, which allows the formation of hydroxide ions. Thus, acidifying the solution will inhibit the precipitation tendency of the alkaline salts, such as calcium carbonate [65]. Other charged ions dissolved in water that are independent of pH variations are classified as non-alkaline salts [66]. Particulate scale, such as silica, can be considered as uncharged molecule scale, as polar water molecules does not have the tendency to dissolve these salts [67]. Furthermore, numerous factors govern the scale formation rate. These factors include: the operational conditions, the composition of water, substrate material, nucleation sites when available, and the supersaturation degree [56, 68, 69].

3.2.1 Alkaline scale in MD

Calcium carbonate is the most typical scale in thermal desalination processes. The fouling of membrane by calcium carbonate scale will often limit the conditions at which MD system can operate at [21, 70], because it is the fastest to reach supersaturation conditions, compared with other salts present in the feed solution [70].

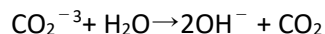
The breakdown of bicarbonate, HCO_3^- , is responsible for the formation of calcium carbonate scale, as shown in the equation: $\text{Ca}^{2+} + 2\text{HCO}_3^- \rightarrow \text{CaCO}_3 + \text{CO}_2 + \text{H}_2\text{O}$

Calcium carbonate scaling under typical MD operating conditions, is dominated by bicarbonate breakdown [71]. However, the carbonate equilibrium is complex, because it depends on many factors. The precipitation tendency increases with respect to increase in pH, and concentration of bicarbonate [72]. The increase in temperature has a dramatic effect on the solubility of CaCO_3 , because CaCO_3 solubility

is inversely proportional to changes in temperature regardless of CO₂ concentration [71]. Moreover, increasing the temperature allows more CO₂ to evaporate from the solution raising the pH and shifting the equilibrium of the equation shown above to the right, thus CaCO₃ solubility may decrease permitting more precipitation to take place [21, 73].

In accordance to Shams El Din, as reported in MSF and common thermal desalination systems, at a temperature as low as 37 °C using ocean water as the feed, calcium carbonate scale may form [74]. Which is typically below the average temperature MD system operates at (50-90 °C). Moreover, alkaline scaling is dependent on many factors such as the residence time, the concentration of the feed, the heat transfer and the operational conditions, etc. [71].

As indicated in the equation below, also carbonate tend to hydrolyze into carbon dioxide, as following:



The equation implies that the solution will become more basic. The increase in pH will allow the precipitation of other scales such as Mg(OH)₂, and the solubility of other scales will be influenced as well [75].

Calcium carbonate has six forms of crystals, known from their different morphology, hardness, refractive index and color. First, the anhydrous polymer form of crystals: vaterite, aragonite and calcite [22]. Although vaterite is common in MD systems with respect to operational conditions, calcite is known to be the most stable form among them, as it was observed in MD systems under laminar flow conditions [76, 77]. While, 99% of the calcium carbonate deposited was in aragonite form in MD instillation operating at higher temperatures [71, 78]. Calcite is rounded in shape and has an average diameter of 10 μm, aragonite has a needle-like structure, while vaterite is spherical in shape with diameter ranges from 0.05 to 5 μm [106]. The three remaining forms occur in hydrated state, known as: Calcium carbonate hexahydrate (CCH), monohydrated calcium carbonate (MCC), and amorphous calcium carbonate (ACC) [71, 79]. Figure 11 shows that the form nature of calcium carbonate is highly reliant on temperature.

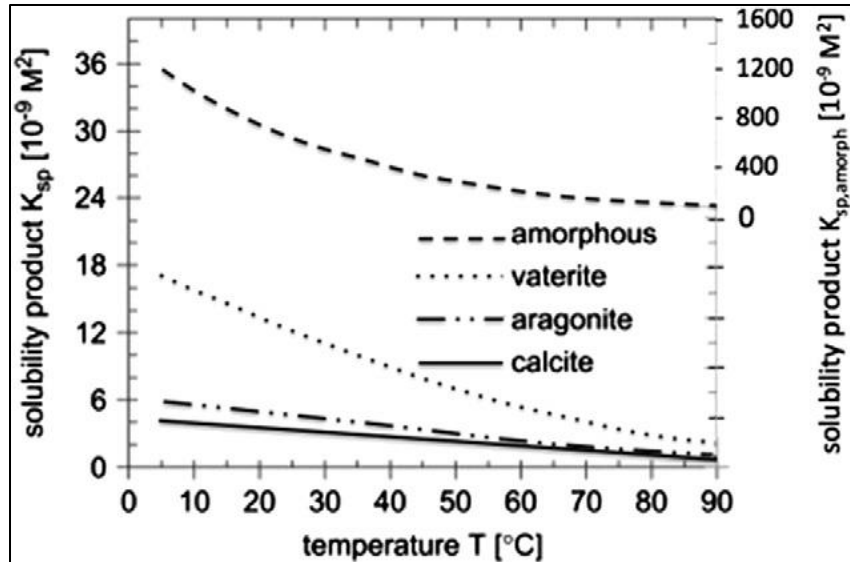


Figure 11: The solubility of different forms of calcium carbonate with respect to temperature [80].

Generally, calcium carbonate scaling in MD process is only observed at quite high saturation indices. However, because of the micro-porous nature of the membrane, calcium carbonate has a high tendency to precipitate at a considerably lower induction period (higher nucleation rate), regardless of the saturation index (SI) value [81, 82]. As reported by Fei et al. calcite scale was observed in the MD system only at a concentration of $CaCO_3$ 32 times higher than the saturation index [77]. However, according to Gryta's observation at temperature ranges of 20 °C to 100 °C using hollow fiber membranes, the induction time of $CaCO_3$ precipitation exceeded 30 minutes although the SI was considered to be at low levels [71, 83]. At higher temperatures, the solubility of $CaCO_3$ decreases. Accordingly, it was recommended by Gryta to operate at a temperature below 80 °C to reduce the scale formation, where lake water was used as the feed [71]. However, in another study using untreated tap water, calcium carbonate was observed at a temperature as low as 40 °C in a stack membrane module [84]. Notably, there is high range of variations of fouling, because scaling is highly dependent on temperature, but is also affected by other factors, such as the properties of foulants, feed water and membrane characteristics, etc. [52]. In concentrated feed

solution, fouling by calcium carbonate can take place in RO process at a temperature as low as ambient [5].

Although studies conducted on calcium carbonate scaling in MD processes are comparably trivial, compared to that in pressure driven systems. In general, it was found that when CaCO_3 was used in feed purely as the foulant, the deposit layer created was nonporous in nature, and high rate of flux decline was observed [56, 71, 85]. However, it was also found that the morphology of the deposit layer is influenced by changes in flowrate. Figure 12 shows a SEM imaging of CaCO_3 on a capillary membrane under laminar flow. Usually, at lower flowrate larger crystals are formed and the scaling layer will be more compact. On the other hand, higher flowrates inhibit the growth of large crystals and the morphology of calcium carbonate layer formed on the surface will be more porous [71]. Accordingly, the flux decline values vary significantly from near zero to as high as 66% [86]. Moreover, it was found in other studies that CaCO_3 can penetrate and block the pores of the membrane, especially in long term performance, causing partial wetting of the membrane and the contamination of the permeate [2, 76, 85].

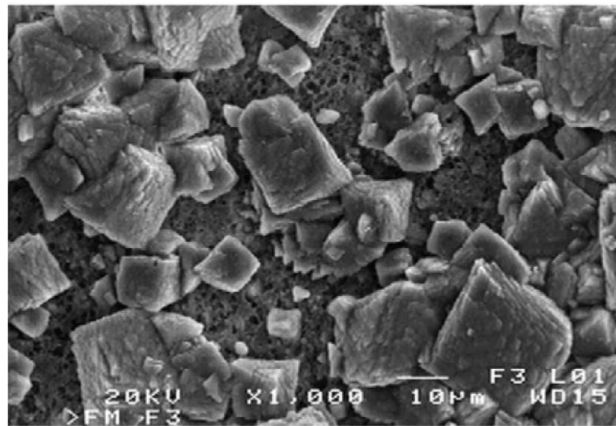


Figure 12: SEM image of CaCO_3 scale morphology on an Accurel PP membrane, using tap water as the feed in a DCMD system [85].

Some studies reported that the level of impurities existing in the solution with CaCO_3 can affect the scaling rate and flux decline. For example, the conclusion brought by He et al. shows that in case of using a highly pure solution of calcium carbonate the membrane scaling was minor [77]. This result agreed with another study conducted by Nghiem et al., where the insignificant impact on the flux decline was explained by the CO_2 transport through the membrane and the rapid homogenous precipitation in the bulk [23].

The foulants co-precipitation is a common phenomenon observed in MD processes and desalination systems in general. The co-precipitation is a more complex and unpredictable behavior of scaling. The most common observed foulants co-precipitation is calcium carbonate with calcium sulfate [56]. Unfortunately, there is no systematic studies on such a behavior [50, 87]. Gryta has observed crystals of bimodal size distribution using SEM-EDX analysis, as a form of co-precipitation of CaCO_3 with CaSO_4 . It was found that the co-precipitation reduced the damage on the membrane and reduced wettability, compared to CaCO_3 alone [56]. Nevertheless, a flux increase was observed when CaSO_4 co-precipitated with CaCO_3 in a study conducted by Fei [77]. The conflict in the results related to the precipitation of these two compounds can be explained from the kinetics of the co-precipitation, because a higher level of carbonate present in the feed implies a slow CaSO_4 precipitation rate, but at the same time the precipitate formed will adhere stronger to the surface [87].

From MD literature it is inferred that the interaction between mixed salts in feed solution has a significant effect on the thermodynamics of scale formation [88]. Gryta has investigated the co-precipitation of CaCO_3 with iron oxide. It was found that the scaling layer was porous and the flux was not reduced significantly [62].

Magnesium scale is of a concern in MD desalination systems in the form of magnesium hydroxide, especially in groundwater and in other applications where the concentration of Mg^{+2} is high in feed solution. Magnesium hydroxide is commonly observed and its solubility is inversely proportional with temperature as CaCO_3 scale [71]. Gryta has found that the $\text{Mg}(\text{OH})_2$ scale formed only at a temperature

above 348 K in a direct contact membrane distillation system, in which he used Mg concentration of 15 mg/L with tap water derived from lake [71].

3.2.2 Non-alkaline scaling

One of the most common non-alkaline scale in MD systems is calcium sulfate [21]. The scale of calcium sulfate can take place as an anhydrite form CaSO_4 , or as one of the two hydrated forms, the hemihydrate (Plaster of Paris) $\text{CaSO}_4 \cdot 0.5\text{H}_2\text{O}$, and the dihydrate (Gypsum) $\text{CaSO}_4 \cdot 2\text{H}_2\text{O}$. Regardless of the form of calcium sulfate scale it is considered to be persistent and can adhere strongly to the surface of the membrane [56]. However, the form of precipitation depends on mainly on temperature, in which gypsum scale occurs at a temperature around 20 °C, while at higher temperature the anhydrite form is more common [21, 89]. In general, the peak solubility of calcium sulfate scale is at a temperature around 40 °C [56], and does not change intensely in typical operation conditions of MD process.

Accordingly, unlike alkaline scale in most cases the cleaning of calcium sulfate scale is relatively difficult and most of the mitigation methods found in literature depends mostly on optimizing the operating conditions of the MD system, to avoid scaling [21]. In a study performed by Gryta on calcium sulfate scale in MD system. Calcium sulfate can be tolerated by bulk flow, if it was in a concentration of 600 mg/L, and does not exceed 800 mg/L [56]. Moreover, it was found that calcium sulfate scaling in MD can cause membrane wetting and blockage of the pores. The SEM imaging revealed a tightly packed, hexagonal, needle-like-gypsum crystals (Figure 13) that tends to grow in the interior of the membrane pores, eventually leading to its damage [56]. As a result, in over 13-hour flux decline of 29% was observed [56]. Other studies revealed that only long induction period after supersaturation condition being reached CaSO_4 crystal formation on the surface of the membrane can be initiated, for example scaling occurred for 2000, 1000, 500 mg/L of CaSO_4 after induction periods of 30, 43, and 53 hours, respectively [23]. Thus, strategies to control membrane scaling by CaSO_4 , may be developed on the bases of the long induction periods [9, 23].



Figure 13: SEM imaging of CaSO_4 during saline wastewater separation in a DCMD process [56].

MD studies were also performed on the non-alkaline sodium chloride scale, the main constituent of desalination feeds. Sodium chloride is known to be highly soluble in water with long induction periods. In an experimental work conducted by Tung-Weng et al. [90] in a DCMD operation it was shown that increasing the concentration of NaCl from 4.5 wt% to 10 wt% caused flux reduction by only 3-4%. This result is expected and is due to increased mole fraction of water (decrease in the driving force) and is not a sign of scaling by NaCl, as confirmed by the SEM imaging showing a minor crystallization level [90]. A comparable result was obtained by Fei He in a MD case study using 10 wt% of NaCl [91]. However, other studies showed a significant flux decline when using high concentrations of NaCl (26-27.5 wt.%) [92]. After reaching a feed concentration of 26% NaCl a dramatic flux drop was observed, after a long induction time of 250 min [92]. Thus, before the flux dropped significantly, the high concentration of NaCl was in agreement with the theory and any drop in flux before 250 min, was only due to the reduction in vapor pressure of the feed [93]. Moreover, other studies showed that membrane wetting may take place when NaCl saturation conditions were exceeded [56, 94].

3.3 Factors that influence scaling in MD

3.3.1 Temperature

In literature, MD operations were performed under wide variety of relevant temperature ranges. Temperature is one of the dominant parameters that affects the performance of MD and membrane fouling and scaling propensities depending on the type of salts present in the feed solution. Notable, the solubility of individual salts may have opposite correlations with temperature. Alkaline salts solubility are typically inversely correlated with temperature, since the precipitation of such salts depend on the hydrolysis with water that increases with increasing temperature, such as calcium carbonate, calcium phosphate, and magnesium hydroxide [66]. While non-alkaline salts solubility is directly proportional to temperature, such as NaCl. In desalination feeds, salts such as calcium carbonate and calcium sulfate that exhibit inverse solubility with temperature tend to reach saturation conditions more rapidly. Moreover, the concentration of these salts varies depending on the source of feed solution, in which the concentration of CaSO_4 is known to be higher when using seawater as the feed, while for ground water being used as the feed the concentration of CaCO_3 tends to be higher. However, in general for common feed solutions it is known that increasing the temperature causes an increased opportunity of scaling and for some salts it reduces the time of induction, implying a higher rate of precipitation [95].

Temperature may have a dramatic effect on biofouling since microorganisms are not tolerant to high temperatures and organic compounds are effected as well, by thermal changes. Most micro-organisms at a temperature above 60 °C, will not be able to survive in accordance with M. Krivorot et al. experiments in MD system using hollow fiber membranes and seawater as the feed solution [96].

3.3.2 Dissolved gases

In the feed solutions of interest in desalination, dissolved gases are present and may diffuse with the water vapor, adding a mass transfer resistance to the driving force reducing the overall vapor flux [71]. Thus, by lowering the permeate flowrate, dissolved gases may indirectly reduce scaling and concentration

polarization, however this effect is minor [55]. Nevertheless, the absence of dissolved gases as studied by Schofield et al. [97] will lead to membrane wettability as the air trapped within the pores will be removed.

3.3.3 *Water source*

As predicted from numerous studies, the fouling nature and likelihood is dependent on the type of feed solution being used in the MD system. In general, using similar operational conditions with a specific source, may give an expectation of the type of fouling that may form, regardless of some exceptions due to seasonal changes in the quality of surface water used [9].

In the desalination process, feed water sources include: lake, river, seawater, ocean, and ground water, waste water may be used as well. The constituents present in the feed water depends on its' source. Seawater contains typically high concentration of sodium chloride compared with other sources and higher concentration of other ions are present in lakes or rivers compared to that in seawater [9].

The expected fouling types that are of concern when using seawater and in consistence with literature studies are: calcium carbonate, calcium sulfate, particulate, and biological fouling [9]. With calcium carbonate being of the most concern in most of the feed water sources. Moreover, since lakes and rivers contain high levels of silica and biological constituents, suspended solids and are characterized by low salinity they are not very applicable for MD uses [98]. Whereas, ocean waters contain high level of salt concentration, with tendencies of calcium carbonate and biological fouling, calcium sulfate being the main fouling concern, and at extremely high levels of sodium chloride, dry-out of the membrane may be an issue [9]. Groundwater fouling tendencies varies significantly depending on its source. However, it is commonly rich in iron that may potentially form iron hydroxide that is almost insoluble in water causing heavy fouling and a significant flux reduction [99].

3.4 Effect of scaling and fouling on the membrane distillation performance

3.4.1 Membrane wetting

It is required that the membrane remains hydrophobic by allowing vapor only to pass through the pores of the membrane, in order to perform probably through MD process [8]. However, once wetting takes place water and any dissolved ions can potentially pass through the membrane pores. Wetting may occur when the feed pressure in the channels exceeds the LEP [34], more importantly in real MD systems fouling and scaling are issues that may eventually induce wetting of the membrane [9]. The hydrophobic nature of the membrane material is the reason to block liquid from passing through the interior of the pores. However, once salt crystals penetrate and grow into the pores of the membrane, the non-wetting character will start to degrade gradually [41]. Scaling induced wetting is a long-term performance concern in MD systems, since the salt concentration is the highest at the interface with the membrane, where liquid evaporates near the pores opening, increasing the capability of salt precipitation in this district [9]. To achieve high permeability, it is recommended to use a membrane with as thin hydrophobic layer as possible and a high porosity and as large pore sizes [100]. In the long-term performance of MD process water penetrates deeper into the pores, hence the thin hydrophobic layer may be wetted easily and once wetting occurred the scaling and fouling phenomena will accelerate and lead to further damage of the membrane [85]. Thus conversely, in order to prevent or reduce wettability it is better to have as thick as possible hydrophobic layer and a small maximum pore size at the surface [41].

Membrane wetting is effected by many factors such as the pores size and shape, the porosity, the surface tension of the liquid and the degree of hydrophobicity of the membrane [101, 102]. Membranes with high contact angle measurements and small pore radius will reduce the potential of membrane wetting [86, 103]. However, the fouling phenomena will not be reduced by increasing the liquid-membrane contact angle [41].

Polypropylene (PP) membranes are relatively inexpensive and have shown their effectiveness in the performance of many MD processes [85, 86, 102, 104, 105]. Yet, PP reveals the smallest contact angle when compared with other polymers (e.g. PTFE and PVDF) used for MD applications. However, PP membranes exhibit lower surface energies and thermal conductivities, which promote their performances as explained in section 2.1.6 [34]. A dramatic scaling of the membrane was observed in MD desalination process using PTFE membranes of pore diameters of 0.2 and 0.5 μm [1]. However in another study by Gryta, no sign of wetting was observed in 3 years' performance of MD system using (Accurel PP S6/2) capillary polypropylene membranes, where the permeate of reverse osmosis (RO) process was used as the feed solution under a temperature of 353 K [85].

Through the performance on an MD process four different degrees of wetting can take place on/in the membrane: (A) non-wetted (B) surface-wetted (C) partial wetted (D) completely wetted (Figure 14) [8].

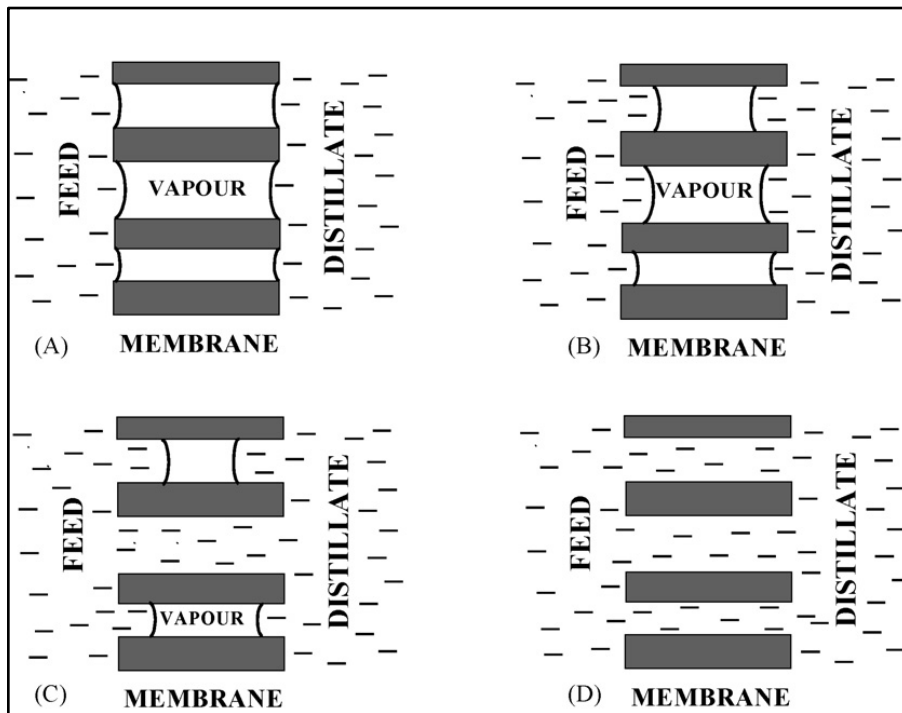


Figure 14: A schematic representation of the different degrees of membrane wettability. (A) non-wetted (B) surface-wetted (C) partial wetted (D) completely wetted. Adopted from [47].

In long-term performance and due to the evaporation at the vapor-membrane interface, surface wetting may take place. Although surface wetting that extends to a certain depth may decrease the permeability of the membrane, the vaporous gap between the distilled and the feed is not broken and the distillation process proceeds. Therefore, the quality of the distillate will not be deteriorated [85]. However, in case of partial wetting the feed may leak through into the permeate side in the open portions of the membrane, while other portions will have decreased gaseous gaps, which will not allow the production of high quality water [90]. However, if the partially wetted parts are small relative to the membrane size the MD operation may continue [86]. Moreover, if the membrane was fully wetted the MD performance will be hindered, since the permeate is allowed to pass through the membrane, and inefficient permeate quality will be produced [41].

Scaling and fouling phenomenon contribute directly to the wetting of the membrane. Furthermore, surface wetting occurs due to the high opportunity of the pores adjacent to the pores filled with deposit to be filled with liquid.

The MD process is derived thermally, as the temperature increases the solubility of carbon dioxide decreases in water, permitting the decomposition of bicarbonate ions that leads to the precipitation of calcium carbonate [41]. There are different forms of calcium carbonate that exist in nature such as anhydrous forms and the hydrated forms. At the feed/vapor interface inside the pores the solvent evaporates [47]. The supersaturation of the solution may be induced filling the wetted part of the pores. Accordingly, a metastable state is created allowing crystal growth and nucleation near to the evaporation surface. Additionally, the solvent may evaporate from the wetted surfaces of crystal, allowing further crystal growth in the vapor phase direction. Water logging takes place in which new areas may be wetted inside the pores, as result of this heterogeneous crystallization (Figure 15) [106].

Moreover, the rate of scaling maybe accelerated due to the inhibition of solute diffusibility from the wetted pores to the feed bulk. The crystallization is effected by the type of the solute and the degree at which it is supersaturated [47].

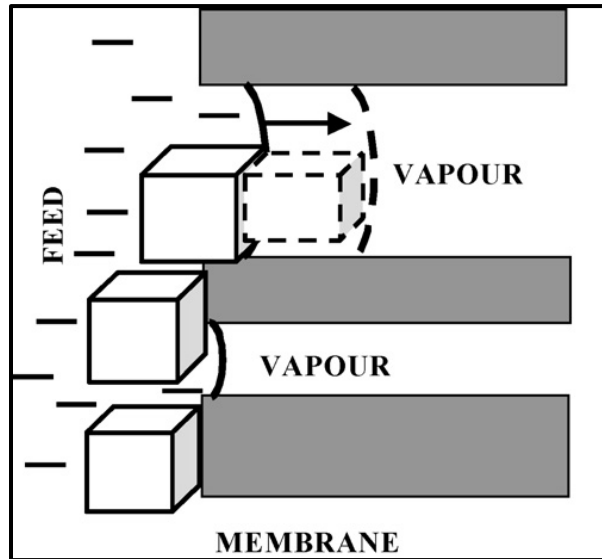


Figure 15: Water logging mechanism [47].

The MD process will be influenced in many ways, once the membrane is wetted. The membrane becomes non-selective and will not achieve the purpose of separation process or desalination. Many studies have shown that once wetting occurs, water can move easily into adjacent pores [50, 62, 85, 86]. The rate of wettability may increase as a result of further crystallization, as explained previously wetting subsequently may lead to scaling within the pores of the membrane as shown in Figure 16. Moreover, salt deposit on the top layer of the membrane will alter its properties to making it more hydrophilic, increasing wetting potential [41, 47, 107]. In some studies, it was shown that wetting propensity on polypropylene membranes, affected only the pores' uppermost part [41]. However, in other studies, using PVDF and PTFE membranes, wetting was reported in the whole portion of the membrane [107]. Salt crystals were

observed in the membranes' full thicknesses along the whole depth, as confirmed by SEM imaging of the cross section of the membranes, depicted in Figure 16.

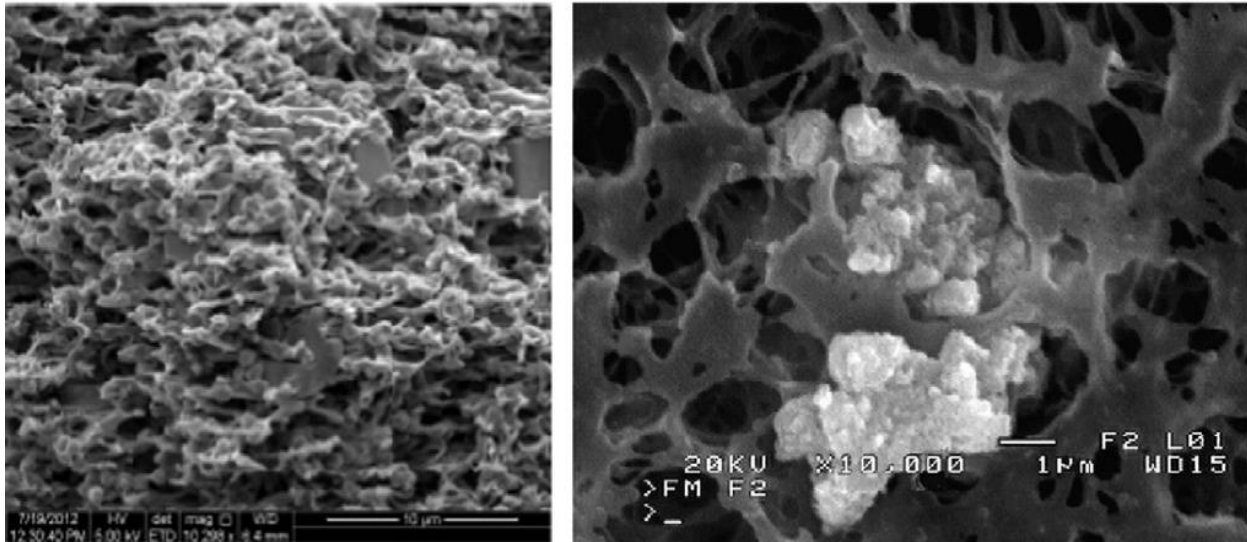


Figure 16: To the left is SEM image of the cross section of a PVDF membrane after an exposure by seawater up to 4 weeks. To the right: a cross section of a PP membrane showing the top portion of the pores after rinsing with HCl [9].

The degradation in the performance of MD process by membrane wettability, is due to either the reduction of the driving force (vapor production), by lessening the area of vapor/membrane interface, or as a result of feed penetration into the pores and eventually into the permeate, leading to its contamination [41, 47, 85, 86, 107].

Interestingly, Guillen-Burrieza et al. [107] reported negative flux (from permeate side to feed) in their study on PVDF membranes, and the positive flux was only restored after a temperature of 10 °C was reached. Franken et al. [108] explained the 30% decay in flux observed in his study at over a duration of month using a DCMD system, by a possible back flow as a result of membrane wetting.

3.4.2 Permeate flux decline

Although few studies were conducted, fouling was reported differently. A metric way was suggested by Warsinger et al. [9] to comprehensively present the effect of fouling on the performance of MD system, by the means of calculating the average flux-reduction percentage. The average fouling rate is defined according to equation 11:

$$\text{Average fouling rate} \left[\frac{\%}{h} \right] = \frac{\text{flux}_{\text{initial}} - \text{flux}_{\text{final}}}{\text{flux}_{\text{initial}}} \times \frac{100}{t} \quad (11)$$

The rate of induced decline in flux by fouling can be used as a direct measure to study the effect of various parameters on MD experiments operating at similar baseline values of flux. Where applicable, together with the fouling rate, the induction period at which the flux starts to degrade can be reported [9]. The induction time is influenced by many factors, such as: the operating pressure and temperature of the system and the foulant constituents present in the feed, etc. After the induction point is reached, the flux decline rapidly, and in some systems a steady state is reached eventually [13].

A wide variety of levels of permeate flux decline were observed. Some experiments showed a minor decay in an operation that lasted for months [10]. Whereas, in no more than two weeks, a flux decline up to 66% was reported [86]. The reason behind this variation is that the drop in permeate flux is related to the formed scale layer thickness and its porosity [62]. Therefore, the permeate decline is dependent on the type of salts present in the feed along with their concentration and solubility under the operating temperature [9]. As explained previously, uncharged particles such as iron oxide scales along with bio-fouling the scale layer was found to be porous. Conversely, non-porous layer of fouling was observed and is of higher propensity to be formed in case of inorganic scaling such as calcium carbonate.

As reported in literature, the decline in flux can be gradual [109], or rapid as a result of exceeding supersaturation conditions, leading to rapid growth of salt crystals [93].

In studies related to fouling and scaling and their control, the rate of reduction in the permeate flow is most reported along with the quality of the distillate that has been worsened. The degree at which the

permeate flow is reduced, gives an indication of the required costs in the designed system to compensate for this reduction [9]. The quality of the distillate, and the degree of contamination by the feed can be quantitatively expressed in terms of salt rejection percentage. It can be calculated using the following equation:

$$\% \text{ Salt rejection} = \frac{\text{Conductivity of feed water} - \text{Conductivity of permeate water}}{\text{Conductivity of feed water}} \times 100\% \quad (12)$$

3.4.3 Increased concentration and temperature polarization

A stagnant hydrophilic layer at the membrane surface is formed as a result of scaling and fouling in addition to the existing thermal boundary layer at the membrane interface, increasing the concentration and temperature polarization effects. If scaling is to decrease the flow velocity, implying a higher residence time of water near the surface, resulting in an increased temperature polarization [110]. Thermal resistance increases, reducing the thermal transfer coefficient at the vapor/liquid interfaces as a result of deposit layer on the membrane surface [12]. Moreover, the process at which polymer materials degrade may be accelerated in some cases [47].

The fouling layer does not contribute directly to temperature polarization, although its thermal conductivity is higher than that of the polymer the membrane made of. However, temperature polarization increases as a consequence of conversing the heat transfer of evaporation, increasing mass transfer resistance; hence concentration polarization is increased [45]. The presence of fouling layer on the membrane's surface, reduces the coefficient of mass transfer. Consequently, the dissolved ions in the interface will increase in concentration, reducing the MD driving force, which leads to flux decline with a higher risk of precipitation [111].

3.4.4 Membrane damage and chemical degradation

Various forms of MD membrane physical and chemical damages were observed in many studies, as a result of scaling and fouling, particularly at lab-scale. These forms include: membrane permeability depression due to the blockage of the surface [41, 107], deflection of the membrane's structure (e.g.

cracking) as shown Figure 17a [107], reduction in the mechanical strength of the membrane [107], diversions in the pores' structure and distribution [107], changes in the membrane surface hydrophobicity and thermodynamics [41, 107]. In many cases, due to membrane damage distillate quality deterioration was observed by lowering the salt rejection rate [65, 85, 112, 113]. The formation of scale layer on the top of the surface of the membrane is the most reported case in MD literature (Figure 17b). The scale layer consists of NaCl in addition to salts that are insoluble, such as CaCO_3 , CaSO_4 and MgCO_3 [41, 107].

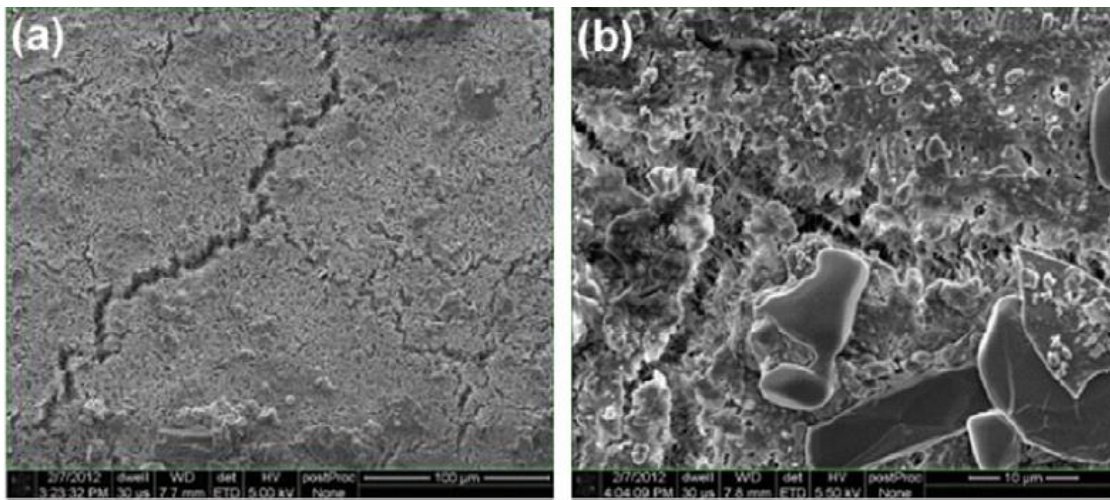


Figure 17: (a) Cracking (b) salt deposition layer. Both (a) and (b) show PTFE membrane within 2 weeks of seawater exposure under drying conditions [107].

In accordance with MD literature either increase or decrease in flux were observed as a result to membrane damage, compared with the flux of an intact membrane [41, 114]. While an increase in flux can be explained by pore wetting that lowers the salt rejection through the membrane [107, 113], flux decrease is primarily due to the blockage of the pores by the deposits formed on the surface [41, 114]. Hsu et al. [1] observed flux decay due to severe fouling, in desalination MD process with high potential of

bio-fouling, however the quality of the distillate was not affected, in this study ultrasonic cleaning was effective in restoring the flux, with only small degree of fouling irreversibility. Moreover, Guillen-Burrieza et al. [107] result is in agreement with that of Hsu et al. in which flux decline was observed through the MD operation as a result of scale deposition at the membrane's surface. While many other studies on MD reported a permeate flux increase after membrane fouling occurred that was attributed by dramatic pore wetting process due to membrane damage and inorganic scaling [9]. In these cases, post washing of the membrane by de-ionized water was not very affective for salt deposition removal [9].

Alteration in membrane's morphology due to fouling was also observed in MD processes. Gryta et al. [41] confirmed a high thermal stability of the PP membranes polymer material, since only small alteration in the membrane structure was observed. Whereas, PVDF and PTFE membranes exposed to seawater under two weeks of operation showed dissimilar behavior in a study conducted by Guillen-Burrieza et al. [107]. They reported a variation in the porosities and the distributions of pore size of the membranes in accordance with membrane autopsies. PVDF membranes showed higher shift in pore size distributions (PSD), compared to PTFE that is because of PVDF broader pore size distribution. These changes were explained by salt deposit layers (4-7 μm) thick and membrane damage, which was more severe in PTFE in the form of fiber cracks attributed by mechanical strength deterioration confirmed using Mullen burst test (Figure 17) [107]. On the other hand, scaling of PVDF membranes took place within the pores. Moreover, the atomic force microscopy (AFM) studies revealed different surface roughness and attraction forces with CaCO_3 for the membranes used [107]. Thus, it can be concluded that the material of the polymer the membrane composed of, in addition to membrane's morphology contribute to its propensity to fouling resistance, with the mechanism of formation left unexplored [9].

Chemical degradation of the membrane was reported during MD operation. Gryta et al. [41] observed increased wettability rate due to loss of hydrophobicity of the Accurel PP membranes. Moreover, the degradation of PP polymer material was confirmed by the presence of hydrophilic surface group due to

increased temperature and oxidation. As recognized by the Fourier transform infrared spectroscopy (FTIR) analysis, sodium carboxylate was formed from the reaction of hydroxyl and carbonyl (hydrophilic) surface groups with the sodium chloride solution [41]. Due to the presence of these surface groups it was difficult to control membrane wetting by simple means of rinsing and drying. Nevertheless, the distillate quality in this study did not deteriorate [47].

3.4.5 Effect of temperature on fouling

The effect of temperature was discussed previously, it was pointed out that different types of fouling are differently influenced by variation in temperature. The dominant effect being the relation between the solubility of minerals with temperature on the formation of scale. Moreover, because of high dependence of common foulants solubility on temperature, temperature polarization plays a major role in fouling and scaling propensities. At the membrane interface the temperature is reduced due to the effect of temperature polarization, reducing the precipitation of calcium carbonate and calcium sulfate which are more soluble at lower temperatures, on the other hand the solubility of other non-alkaline foulants are increased due to their inverse solubility with increased temperature polarization. Moreover, higher temperatures may hinder biological fouling formation, so a higher degree of temperature polarization can simulate bacterial growth due to biofouling. In a study conducted by Gryta [71], where the feed was lake water using hollow fibers PP membranes in DCMD process, it was found the major foulant was calcium carbonate. Figure 18 is used to demonstrate the effect of elevating temperature on the rate of CaCO_3 scale formation, where the percentage decrease in the flux per hour is used to represent the rate of fouling induced by CaCO_3 scale [71]. Reduced flux contributing to a higher concentration polarization as a result of inverse salt solubility in the feed stream with increase in temperature translated to a significant higher fouling rate. Figure 18 shows that increasing the temperature from 80 to 90 °C increased by four times the fouling rate [9].

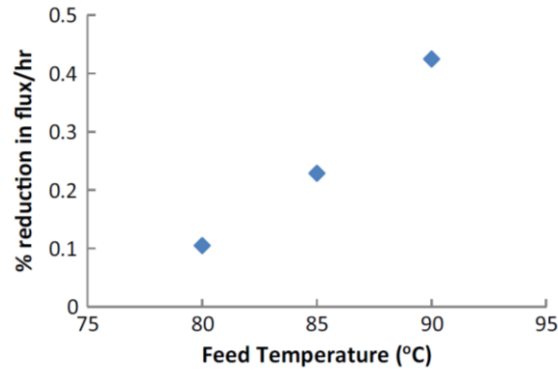


Figure 18: The effect of increasing temperature on the fouling rate, where the major fouling contributor is CaCO_3 scale [9].

In another study conducted by Long D. Nghiem et al. [23] on the effect of increasing temperature on CaSO_4 scaling in a DCMD system at a constant flowrate. Figure 19 shows that using an initial concentration of 2000 mg/L of CaSO_4 as the feed solution, the induction time of CaSO_4 scale formation was found to decrease as the feed temperature increases. Moreover, the size of the crystals formed were directly correlated with changes in temperature. The largest crystals were observed by SEM image at temperature of 60 °C, while a thin needle-like structure of crystals was observed at 40 °C. The results attained by this study is in agreement with the thermodynamics and kinetics of CaSO_4 precipitation in theory [23].

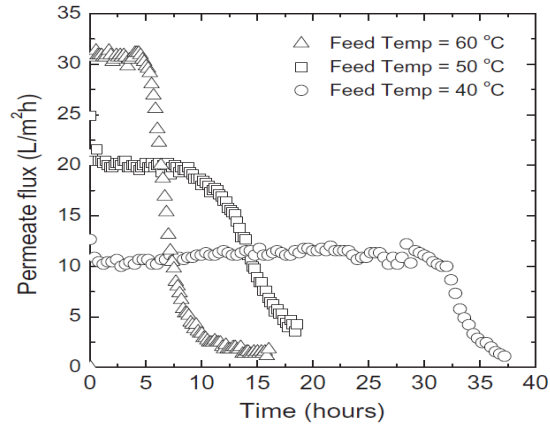


Figure 19: The permeate flux profiles obtained at different feed temperatures, using a solution of CaSO_4 as the feed [23].

3.4.6 Effect of feed flowrate on fouling

The mass and heat transfer coefficients are directly affected by the feed flowrate in the channels. An increase in the velocity of the feed is translated to a higher mass and heat transfer coefficients, despite the discontinuance in this increase due to the transition region from laminar to turbulent flow. The temperature polarization effect is reduced due to the increase in flow rate and permeate flux [9].

The increase in temperature causes a decrease in the solubility product (K_{sp}) value for salts that have inverse solubility such as CaCO_3 (Figure 11). As previously mentioned, the increase in flow velocity increases the heat transfer coefficient (h); increasing the temperature at the interface. Also, the salt concentration at the interface of the membrane decreases as a result of the increase in the coefficient of mass transfer [9]. Thus, the activity product and the K_{sp} both decrease, which are the numerator and denominator of the saturation index (SI), respectively [115]. Described in equation (13).

$$SI = \log \left(\frac{\text{Activity product}}{K_{sp}} \right) \quad (13)$$

Therefore, the rate at which these two quantities varies determine the change in SI relatively which gives an indication of fouling tendency at the membrane surface as a function of salt supersaturation [9].

However, the numerical models in literature study the effect of changes in system parameters on the fouling rate induced by flux decline in terms of SI assuming the presence of a single salt only [9], which is not the case in real seawater and other surface waters. Where the presence of mixture of salts significantly contribute to major changes in SI value, the current numerical modeling gives only a general trend of SI variation under the effect of various parameters [88]. Moreover, the co-precipitation of a salt in the presence of other salts may have a different solubility product leading to variations in the structure and morphology of the precipitates, and the solubility product for a given precipitate is a function of temperature only [88]. Thus, there is a lack of studies on the thermodynamics of precipitation tendencies in terms of SI indices by numerical modeling, that take in account the overall effect (in the presence of salt mixtures) of fouling as a result of increasing the feed flowrate at the membrane surface.

In a study conducted by Gryta [71] on the influence of varying the feed velocity on the rate of fouling using tap water as the feed and hollow fiber polypropylene membranes with pore size of (0.22-0.55 μm) and porosity of 73%. At a constant temperature of 80 $^{\circ}\text{C}$, it was found that increasing the flow velocity from 0.31 to 0.96 m/s lead to a notable reduction in flux decline; lower decrease in flux. However, as indicated from Figure 20 further increase in the velocity from 0.96 to 1.4 m/s did not enhance the flux performance, despite the initially higher flux at 1.4 m/s the decline in flux was steeper. Thus, it was concluded that an optimum flowrate can be adjusted for each MD module, where further variation in flowrate may have limited effect on the efficiency of the performance [71]. It was pointed out that the influence of the distillate flowrate is less significant on the flux performance. Moreover, the crystal morphology by SEM imaging shows that at the lower feed flowrate (0.31 m/s) an adhered fouling layer was formed of larger crystals on the surface of the membrane and penetrated into its pores, indicating a sign of wettability. While the opposite is true for the higher flowrate (0.62 m/s) with a more porous layer of fouling formed, where the shearing action of water is higher and can distribute the crystal formation and remove precipitation [9].

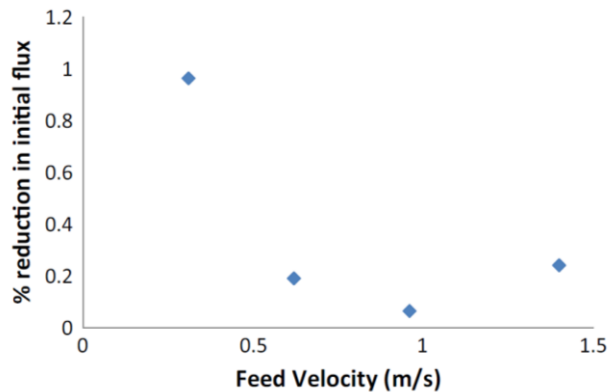


Figure 20: The effect of feed velocity on the fouling rate (% decline in initial flux) at a constant temperature, literature data [9, 71].

In another study performed by He et al. [77], using brine as the feed solution in a crossflow hollow fiber DCMD system. According to their experimental work the maximum precipitation rate of calcium ions was observed at a velocity 688 mL/min, which is an intermediate value between the other two velocities shown in Figure 21. However, it was stated that as Reynold's number increase the temperature at the membranes interface should increase, eventually the concentration polarization effect increases and dominates over the temperature polarization effect in the MD operation [77]. Nevertheless, the highest flux decline percentage was observed at 688 mL/min. The conclusion brought by He et al. [77] on the effect of the flowrate is by some means consistent with Gryta's conclusion [71]. Likewise, other studies [114, 116] confirm the presence of an optimum feed flowrate depending on the MD module used in their studies, in which further variation in the feed flowrate will not lead to any improvement in the efficiency of the module. Thus, literature findings imply that there could be a specific flowrate, where above, an inverse or insignificant effect may be observed. In other words, for each module the fouling rate decreases at a higher feed flowrate up to a certain value, where further increase in feed flowrate will reduce its effect on the scaling potential.

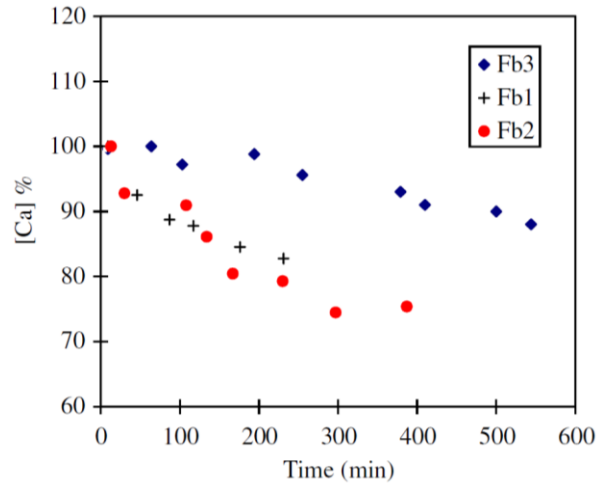


Figure 21: The effect of feed velocity on calcium concentration [Ca]%. Where Fb1, Fb2 and Fb3 are 84, 688, and 1438 mL/min, respectively.

3.5 Fouling mitigation and control

The main mitigation techniques used in MD systems so far, are chemical cleaning and the pretreatment of the feed [13, 56]. However, many other technologies and methods were employed in the purpose of scale inhibitions and fouling preventions, including: hydraulic cleaning, surface roughness reduction, altering surface charges or the hydrophobicity of the membrane and increasing the flowrate of the feed [55]. The use of antiscalant and the effect of filtration were investigated, in addition to other less employed technologies, including: magnetic water treatment, heating of the feed, flocculation and variation in pH [76, 86, 92]. Some of these mitigation technologies will be discussed in more details.

3.5.1 Use of antiscalant

The use of antiscalant in pressure-driven applications, such as reverse osmosis and multi-stage flash desalination, has shown its effectiveness in scaling inhibition [117, 118]. Antiscalants are known to be effective inhibition tool for inorganic scales of carbonate, and sulfate, along with fluoride, metal oxides, and detached colloids [71, 119]. Antiscalants are of low costs and only small doses are required, usually less than 10 ppm [9]. However, antiscalants are claimed to reduce the surface tension of water and may

accelerate membrane wetting, since their molecules are typically organic [120].

Antiscalant can be defined as a chemical added to the feed to interfere with the adhesive forces of the scales and foulants to the membrane surface; to hinder crystallization and precipitation reactions [8]. The antiscalant acts through different mechanisms, it is adsorbed on the surface of the crystal, so that the active sites of growth are blocked. The growth rate of the crystals is retarded; thus, nucleation and precipitation rate are delayed, and the properties of the crystal surfaces and their accumulation tendencies are altered. Furthermore, the use of antiscalant may cause deviations in the morphology of the crystals (deformed scales) by weaken the adhesion to the membrane surface, or it may change the concentration of CO_2 [121, 122]. However, since the antiscalants have hydrophilic property a possible mechanism to inhibit the scale formation is by changing their surface energies, they may as well have a potential to alter the surface energy of the membrane in a MD application, and eventually lead to membrane wetting [8].

A study performed by Gryta [116] to investigate the use of antiscalant to particularly inhibit calcium carbonate scaling in a hollow fiber MD system. The antiscalant was designed for RO and polyphosphate-based. However, the name and composition of the used antiscalant were not provided. Large cubic-like structure of crystals was formed without the use of antiscalant. Although CaCO_3 crystals growth was reduced significantly when adding the antiscalant in a dose of (2-20ppm), a thin amorphous non-porous layer was created on the surface of the membrane, eventually lead to the reduction in the permeate flux. Moreover, it was found that the flux was higher without adding antiscalant and the more concentrated the antiscalant was, the lower the flux of the permeate [116]. Periodic rinsing by HCl was applied and found to be effective along with the use of antiscalant, since the initial flux value was restored and no sign of wetting was observed. However, the MD operation time was recommended to not exceed one hour, in order to prevent the breakdown of the antiscalant to form orthophosphate deposit [41].

Another study performed by He et al. [123] showed more positive results using hollow fibers with

fluorosilicone coated PP membranes and different types of antiscalant, with different degrees of scale inhibition depending on the type of antiscalant used. For example, it was found that antiscalant composed of polyacrylic acid was more effective in calcium sulfate scale inhibition than the organo-phosphorus antiscalant that was more potent in reducing calcium carbonate scales. Moreover, a blend of phosphoric and carboxylic acids antiscalant showed a moderate inhibition of both calcium carbonate and calcium sulfate scales [123]. Varying concentration of the antiscalant from 0.6 to 70 mg/L was applied, however increasing the dose of antiscalant did not show any changes in the degree of scale inhibition. The measurements of the antiscalant solutions surface tension (71.5 mN/m) were similar to that of tap water (71.8 mN/m) [123]. Under the operational conditions of the experiment no signs of wetting phenomena were detected by the breakthrough pressure test.

3.5.2 Membrane cleaning

Cleaning by acid is commonly applied method in laboratory MD studies in order to reclaim the fouled membrane. In terms of removing salt depositions from the membrane surface, many acids have been used including weak and strong acids with HCl being the most common acid used in studies related to MD systems. HCl is effective in dissolving salts that are basic such as CaCO_3 . In terms of cleaning the membrane, an acidic solution is introduced to the feed in a batch process replacing the feed water. However, as noted by Gryta [26,152], the permeate should be removed during the cleaning process since HCl is volatile and can blend with the water vapor to reach the permeate side.

Acid cleaning by HCl of the membrane where the major foulant is CaCO_3 as reported by Gryta [26, 152] was found to restore the flux to its original value. However, repeating the process of rinsing with a concentration of 2-5% of HCl, the flux restored was reduced compared with the original value as reported by Gryta [111]. In another study by Curcio et al. [25] using feed solution of synthetic seawater, the MD flux and hydrophobicity of the membrane were completely restored by applying two steps of rinsing; by an acidic solution followed by a NaOH solution with a period of 20 min between each step. Pretreatment

with $\text{Ca}(\text{OH})_2$, was found to be effective in reducing silicates and sulfates fouling, as reported by Gryta et al. [102].

In case of cleaning the membrane from iron oxide scale Gryta [26] added HCl with different concentrations (5-36 wt.%). Although adding a high concentration of HCl (36 wt.%) fully removed iron oxide scale in a duration of one hour, the flux decreased and the membrane was wetted indicating that the negative effects of fouling by high acidification level was increased. Thus, Gryta recommended 18% HCl to partially remove iron oxide scale and recover the flux near to its initial value as it worked better than 5% HCl, eliminating the other negative effects caused by higher concentrations.

Thus, the effectiveness of cleaning by acid rinsing varied dramatically according to the type of foulant existing in the feed, the amounts of acid added, and the time the acid is allowed to act. In general, HCl washing was effective in removing alkaline scales including CaCO_3 . Crystalline scales required stronger acids to be removed, such as iron oxide scales [26]. While, other organic foulants were partially removed by the addition of acids to clean MD membranes, acid cleaning was not very effective in the removal of other forms of scales such as silica [30]. Overall, acid cleaning can be effective in reducing the rate of fouling relatively, especially for alkaline foulants. However, continuous addition of acid to modify the pH, adds to the cost of MD process, depending on the value of acid added [124].

Other cleaning methods include, rinsing with de-ionized (DI) water that absorbed salts readily [121] or by simple approach of reversing the flow direction. For example, in a study performed by Mericq et al. [109] using VMD system with synthetic seawater as the feed, the flux was recovered completely by running water permeate RO that re-dissolved the salt depositions. In another study conducted by Meindersma et al. [87] using AGMD configuration with pond water where biofouling was major, reversing the flow was effective in restoring the flux completely.

3.5.3 Gas bubbling

Gas bubbling is one of the methods that was implemented to reduce the effect of temperature and concentration polarization. Chen et al. [83] improved the flux by adding turbulence to the feed in the means of introducing gas bubbles, which consequently reduced membrane fouling. Spacers have been used to induce turbulence in the feed streams. Chen et al. [83] used hollow fibers in an MD process where the permeate was inside the fibers to study the effect of different configurations on the flux and fouling tendencies, including: spacer, air bubbling with no-spacer, and no-spacer. The lowest flux was that in the case of no-spacer. However, after certain time NaCl concentration increased and formed a fouling layer. The scaling was more severe in the case of spacer compared to no-spacer case due to the trapping of NaCl near the membrane surface, which may not be the case in flat sheet configuration. While less scale formation in the air bubbling case showed an improved performance due to sufficient mixing and hindering of the local salt trapping. At higher temperatures and lower feed flowrates, where temperature and concentration polarization are expected to be the highest, air bubbling is anticipated to give high improvement in MD performance by decreasing fouling tendencies. However, gas bubbling increases the concentration of dissolved gases in the feed and may add a mass transfer resistance in the permeate stream in configurations such as SGMD and AGMD [9]. In addition, air bubbling impact on the membrane pores' gas content and on gas chemistry such as the content of CO₂ may affect the progression of salt formation [125].

3.5.4 Magnetic water treatment (MWT)

MWT technology was developed in the purpose of hindering the rate of nucleation, however it makes the crystal growth more significant. MWT is implemented for water treatment purposes and heat exchangers [76, 126]. Gryta studied the effectiveness of a MWT device that is available commercially on treating hollow fiber membrane, where the feed used was tap water with the addition of HCO₃⁻ of 2.7 and 3.6 mmol/dm⁻³ alkalinity, heated up to 85 °C by running 0.1 T magnetic field [76]. A significant improvement

in the flux was observed, as expected the morphology of the crystal was changed, despite the bigger crystals in size mainly calcite, a thinner and more porous layer of scale was formed. Moreover, no signs of membrane wettability were observed under MWT [76].

3.5.5 Membrane modification and enhanced properties

Some research studies were conducted for the purpose of reducing fouling rate and achieving higher salt rejection by modification the MD membrane surface by the addition of coating layer, or increasing the hydrophobicity of the membrane by increasing the LEP and the contact angle, to further reduce wettability.

In a study performed by Zhang et al. [127] the fabricated PVDF membrane showed a higher hydrophobicity in terms of increased contact angle from 107° of the original membrane into 156° , this was attained by casting a mixture of SiO_2 nanoparticles that is hydrophobic with polydimethylsiloxane (PDSM) on the surface of the flat-sheet membrane. It was found that the performance of the DCMD was improved by a higher rejection of salt performance and a longer induction period for the modified membrane, despite the lower permeation flux. After 40 h using a high concentration of NaCl (25 wt%) the flux declined steeply for the original membrane compared with the modified one, indicating lower fouling and wetting propensities of the fabricated membrane. After the fouling test NaCl deposits were found to penetrate through the pores of the original membrane; not only on its surface, which was not the case in the modified membrane, revealing that SiO_2 nanoparticles is an example of a potentially effective surface modification method that can be employed in fabricating anti-fouling membranes [127].

Super-hydrophobic coats can provide a reduction in the surface nucleation rate and the attachment of particulates, by acting as a buffer layer [128]. Moreover, these coats enhance the performance of acid rinsing recovery, and hinders membrane wetting [129, 130]. A contact angle of 166° can be reached by fluorosilicone coatings, that are created by the use of hydrothermal synthesis at low temperature to deposit TiO_2 on the surface of the membrane [130]. These fluorosilicone coats showed their effectiveness

in hindering fouling by gypsum increasing the induction period, in MD hollow fiber membrane [123]. In other studies, coating by fluorosilicone significantly reduced CaCO_3 and CaSO_4 scales formation by the means of pore size reduction [48, 77, 96].

Another factor in mitigating membrane scaling and wettability is by increasing the surface porosity and reducing the pores size. Gryta has found that CaCO_3 crystals penetrate the interior of the membrane, in a study conducted on PP capillary membranes with larger pores on its surface, using tap water in the feed stream [47]. The decline in flux observed was similar for membranes having same properties other than their surface porosities, which indicated that the membrane was not clogged in case of higher porosity. However, higher porosity increased the tendency of membrane wettability [47]. Coating the surface with a thin ($1\mu\text{m}$) low porosity layer was found to be effective in reducing wetting tendency, with similar permeate flux compared to an uncoated membrane. Moreover, reducing the pore size to a size smaller than that of the crystal was admitted to restrict their penetration into the pores of the membrane [47]. Thus, applying a thin coat of low porosity may be recommended to reduce membrane wettability, without causing a high reduction in the permeation flux.

Other studies suggested that the material of the membrane may have different degrees of hydrophobicity accounting for different membrane wetting tendencies. for example, Tung-Weng et al. [90] noticed that under similar operating conditions PTFE membranes was more capable of resisting wetting, compared with PTFE membranes. In Gryta study, PP membranes undergo wettability in few days, they were claimed to not exhibit optimal hydrophobicity [47]. Moreover, membranes fabricated of non-polymer materials such as glass are believed to have an improved thermal and chemical performances [129].

3.6 Fouling monitoring and used membrane characterization

To be able to understand fouling and its propensity, it is essential to assess foulants by diagnostic techniques. These measurements include physical, chemical and biological characterization. The characterization methods provide information that help in understanding the fouling process formation

and fundamentals [131]. Thus, fouling control and minimization techniques can be developed based on this understanding of the mechanisms governing fouling process.

Many factors contribute to the lifetime of a membrane such as the chemical and physical cleaning and control methods, in addition to the operational conditions of a MD system. Membrane autopsy is used to assess the degradation in MD performance and a membrane's lifetime along with the changes in its properties even after long operation. Autopsy involves dissecting the membrane and examining the surface to check for foulants and other components that may lead to further damage [132]. Accordingly, the development of cleaning and control strategies, and future pretreatment is based on the characterization methods, and the reveal of foulants identity by membrane autopsy [61]. Some of the characterization techniques applied in MD studies are summarized in Table 2.

Table 2: Summary of some physical, chemical, and biological characterization of fouled membranes, adopted in MD studies.

Physical	Chemical	Biological
Scanning electron microscopy (SEM)	Energy-dispersive X-ray spectroscopy (EDS or EDX)	Direct method: microbial community and microscopy, such as: Confocal laser scanning microscopy (CLSM)
Atomic force microscopy (AFM)	Inductively coupled plasma mass spectroscopy (ICP-MS)	
Contact angle	Foulant concentration by total organic carbon (TOC)	
Pore size distribution (PSD)	Zeta potential	Indirect method: flux decay, transport of solute and bacteria enumeration, and flow field-flow fractionation (FIFFF)
Ultrasonic time-domain reflectometry (UTDR)	Tensile strength parameter	

3.6.1 Physical characterization

Scanning electron microscopy (SEM) a common technique used to view samples' surface structures, morphologies and cross-sections at a microscopic level. SEM provides an image of the targeted area on a screen by generating high-energy electron focused beam that travels in a series of magnetic lenses. Usually, the sample is sputter-coated by gold, platinum or carbon thin layer in order to improve the image resolution by rising the sample's conductivity. The membrane surface and the foulants are assessed qualitatively and quantitatively by SEM providing details about their morphologies, thicknesses and structures. However, a complete or partial dry out of the sample is needed to be used in SEM, increasing the tendency of altering the structure of some foulants [24]. Figure 22 provides an example of a virgin and fouled membrane SEM images.

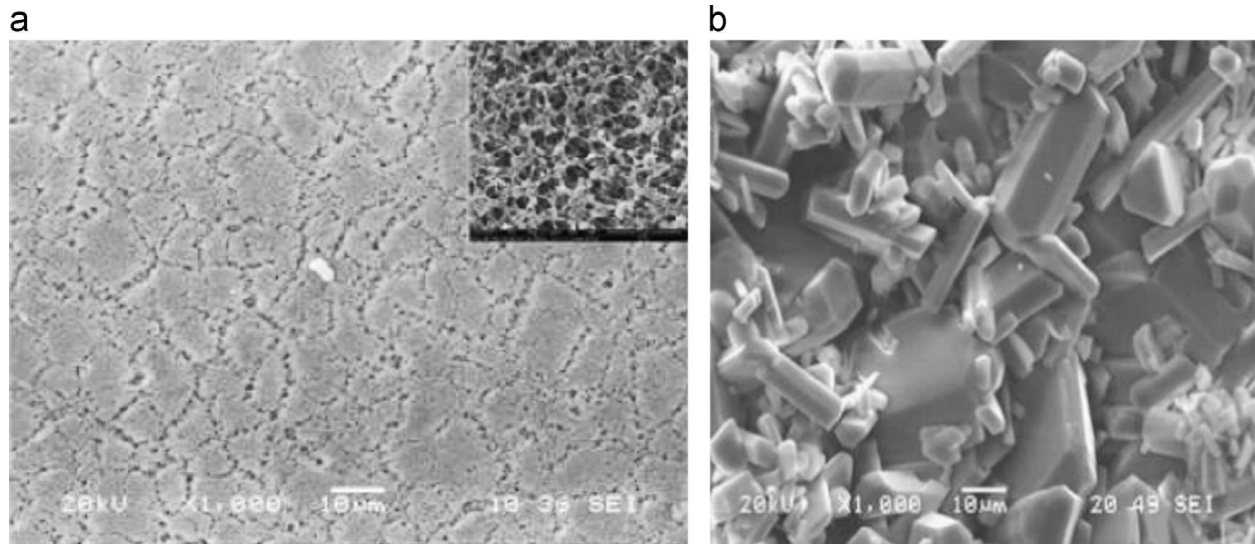


Figure 22: SEM images of (a) virgin membrane (b) fouled membrane [133].

Atomic force microscopy (AFM) is carried out by the use of different modes of cantilever deflection based on Hooke's law. AFM is of a higher resolution compared to SEM, by providing a three-dimensional (3D) profile in a nanoscale level of the surface, without the need of sample pretreatment. Surface morphology, topology and roughness are provided by AFM [134, 135]. However, AFM is of a slow scanning speed, and may be effected by membrane's surface high roughness [131].

To investigate the thickness of the deposit layer, optical laser sensor method can be utilized. The deposit thickness is translated by detecting the difference in the intensity of signal provided by a laser light crossing the deposit layer [136]. This method showed its effectiveness in fouling inspection in a microfiltration process.

Ultrasonic time-domain reflectometry (UTDR) provides a media's physical characteristics where the ultrasonic waves travel, in addition to the location of a moving or stationary interface real-time measurements. The ultrasonic waves are reflected in the presence of interface between different media by partitioning the energy of the detected waves. The thickness can be calculated from the medium velocity along with the detected waves reflection by the transducer [12]. The investigation of fouling

layers in a flat-sheet membrane by UTDR was used by Mairal et al. [20]. Other studies [137, 138] utilized this technique for fouling characterization in hollow fiber membranes.

Surface wetting is determined from the composition of the materials along with the geometry of the surface structure [12]. Contact angle (CA) measurement is used to quantify the wettability of a membrane. Thermodynamically there are three forces, that are balanced when dropping water on a horizontal surface. The three forces shown in Figure 23, include: the interfacial solid-liquid tension, the solid-vapor tension and the surface tension of liquid-vapor [139]. The droplet shape and angle is determined by these forces. The surface is hydrophilic when the angle θ is less than 90° and the droplet forms a thin film. Whereas, the surface exhibits a hydrophobic behavior when the angle is above 90° , with a droplet having a cylindrical shape. surfaces exceeding contact angle of 150° , are considered to be super hydrophobic [140]. Moreover, super hydrophobicity is achieved by modifying the membrane's low surface energy and surface roughness.

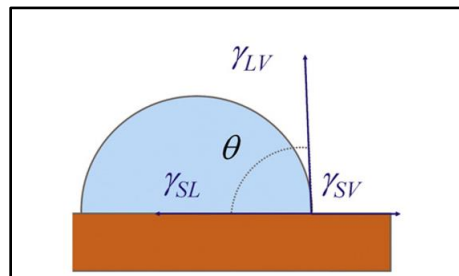


Figure 23: A diagram showing a liquid droplet with the three-phase forces [139].

3.6.2 Chemical characterization

Energy dispersive X-ray spectrometry (EDS) is a technique used to analytical analyze the composition of the elements present in a fouled surface. EDS devise is often coupled with SEM. In EDS analysis, the electromagnetic radiation interacts with the definite atomic structure of each element in the fouling layer

to generate different peaks. Figure 24 provides an example on the EDS of a deposit layer on a PP membrane, according to this EDS the main elements composing the deposit are mainly calcium, and traces of Al, S, Mg and Cl. Thus, it can be concluded that the main fouling issue is calcium carbonate scales.

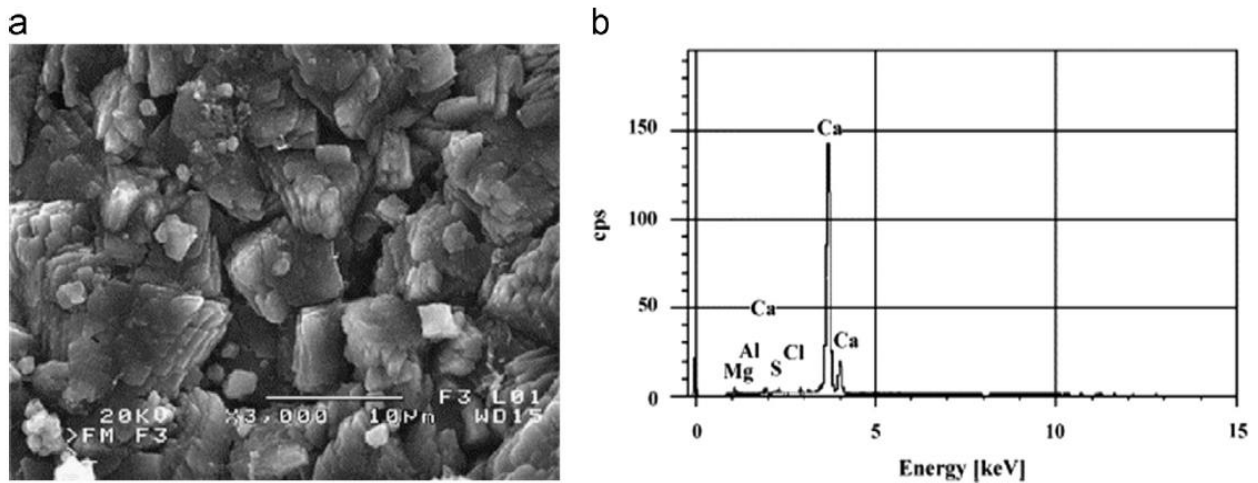


Figure 24: (a) SEM image of the membrane (b) The attached EDS spectra showing elemental composition of the fouled layer used tap water as the feed [47].

In a fouled layer the concentration of metal and non-metal elements in parts per million (ppm) and parts per billion (ppb) is measured using inductively coupled plasma mass spectroscopy (ICP-MS). Ions such as magnesium and calcium can be selectively detected at high accuracy by the ICP-MS. The samples are prepared by dissolving the deposits from the surface of the membrane by acidic or alkaline solution [8]. Usually, more efficient extraction by alkaline and acidic solutions of organic and inorganic scales, respectively [131].

Tensile strength parameter is an important factor in detecting the mechanical integrity of a membrane, that has been used in autopsy studies [141]. The tensile strength of a virgin membrane compared to a fouled one gives an indication of the degree at which the membrane can withstand the operation of MD in long-term performance before it deforms permanently, due to structural changes caused by fouling.

Remarkably, applying cleaning and fouling control techniques extensively in long terms can lead to the damage of the membrane by affecting its mechanical integrity. A universal testing machine can be used to determine the tensile strength parameter following standard test procedures such as ASTM D368-10 [8].

Another chemical characterization method of the membranes is the zeta potential. It is used to determine the charges of the surface, in order to evaluate the interactions that may take place between the membrane surface charges and the foulants present in the feed. The zeta potential can be identified by measuring the potential difference between the charges on the surface and dispersed charges in the feed solution to identify the membrane electro-kinetic phenomena [8].

Biological characterization of the membrane was not considered, since it is outside the scope of this work, where seawater was used as the feed solution. Some of the membrane characterization techniques discussed, namely SEM-EDS analysis and contact angle, will be employed in this investigation to support results and discussion.

4 Experimental Methodology

4.1 DCMD bench scale unit

The DCMD apparatus with flat-sheet used in this work, is composed of different instrumental parts, as shown in Figure 25.

The instrumental parts can be divided into:

- 1- DCMD cell (module).
- 2- Distillate and feed tanks.
- 3- Peristaltic pumps and connection tubing.
- 4- Electronic balances.
- 5- Bath units of cold and hot water (cooler and heater).
- 6- Digital thermometer and associated cables, hot/cold sides.
- 7- Desktop computer with data acquisition system.

Similar system was used in a previous thesis project [142]. The selection of DCMD was based on its availability and to the fact that it does not require additional facility to condense the permeate vapor.

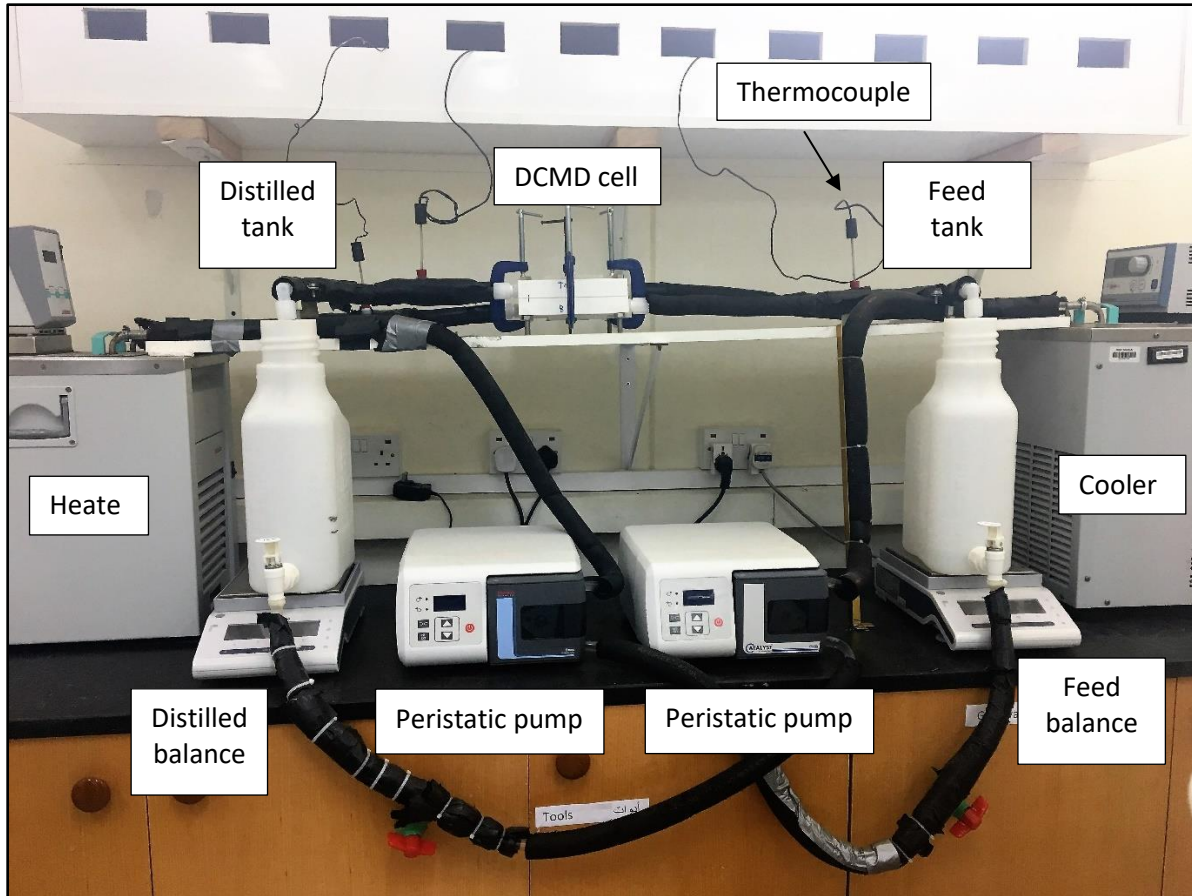


Figure 25: The bench scale DCMD unit setup in the chemical engineering laboratory of QU.

The distillate reservoir was filled initially with 2.5L of deionized water, while the feed reservoir was filled initially with a maximum of 5L and not less than 4L of seawater. The temperatures of the hot and cold streams were selected using the water bath temperature control set points; usually up to 30 minutes would be required to reach thermal equilibrium. A digital thermometer was used to assess the temperature from four thermocouples connected to the tubes from the inlet and outlet of the feed and distillate streams in and out the DCMD module. As can be seen in Figure 25 the tubes were insulated to prevent heat losses from the system. Notably, the distilled (cold unit bath) and feed (hot unit bath) are recycled in closed loops, that are not allowed to overlap. The data acquisition system can be started after

the temperatures were stabilized. Then the temperatures of the feed and distillate streams entering and leaving the DCMD unit were manually measured throughout the experimental operation. The data acquisition system that was connected to the distillate balance, records the weight of the distillate tank. It was programmed to continuously record the weight in the desktop every 30 seconds. Then the data recorded were saved as ASCII text file and further processed in excel spreadsheet, to produce flux graphs from weight data and membrane effective area. The temperature and flowrate were selected then the operation continues until the flux drops to almost zero. It took around (45- 91) hours depending on the selected operational conditions to be able to replace the membrane and start a new run with different parameters. Furthermore, under some selected operation conditions the runs were repeated, but with antiscalant added to the feed seawater to investigate its effect on MD process.

4.2 Feed solution

In this study, raw seawater was used as the feed solution from two different locations in Qatar: Alwakra, and west bay nearby beach regions. However, as shown in Table 3 it can be noted that the values obtained are similar since the sources are not too far apart. Moreover, the conductivities of seawater measured are comparable with that of Arabian Gulf of UAE reported in literature (59-65 mS/Cm) [107].

Table 3: The conductivity and pH of the feed seawater.

Feed solution	Source Location	Conductivity (mS/Cm)	pH
Seawater	Alwakra	62.5	7.5
	West bay	63.9	7.9

4.3 Membrane flat-sheet

A Hydrophobic polypropylene flat-sheet membrane (supplied by Membrana, Germany) was used in this study as shown in Figure 26, and the properties of the membrane are listed in Table 4.

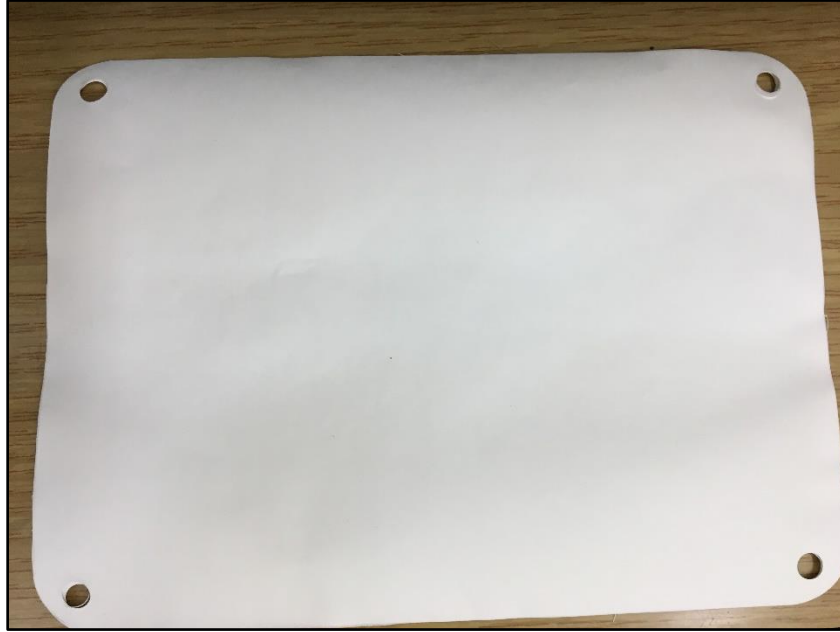


Figure 26: The flat-sheet PP membrane used in the MD runs.

Table 4: Properties of the polypropylene membrane used.

	Membrane trade name	Accurel PP 2E HF (R/P)
Chemical composition	Polymer	Polypropylene
	Residual oil content (%)	≤ 0.1
Physical characteristics	Thickness (μm)	170 ± 15
	Porosity (%)	73 - 75
	Nominal pore size (Microns)	0.2
	Surface energy ($\times 10^{-3} \text{ N/m}$)	30.0
	Thermal conductivity ($\text{W m}^{-1}\text{K}^{-1}$)	~ 0.17

Flat-sheet membranes are more widely used for MD applications in small scale studies compared to hollow fibers. Flat-sheet membranes were found to be less prone to fouling and when operating under the same conditions as hollow fiber, they were claimed to have better performance in terms of their capability in producing higher flux. Moreover, flat-sheets are easier to clean when needed, because of their simpler design [34, 143]. For these reasons, flat-sheet membranes were designated in this study.

The membrane's active area is 0.014 m². The coupons membrane width and length are 14.1 and 19.2 cm, respectively.

4.4 Configuration of DCMD Unit

The DCMD module used in this work was made available from an on-going infrastructure building project supported by ConocoPhillips [144]. Figure 27 shows the MD module bottom and top plates. The module was made up of two machined compartments made of solid PTFE (Teflon) with the membrane and spacer "sandwiched" within as depicted in Figure 28. The feed (hot) stream flows through the bottom plate, in a counter-current flow regime with the cold (permeate) stream carried in the top plate.

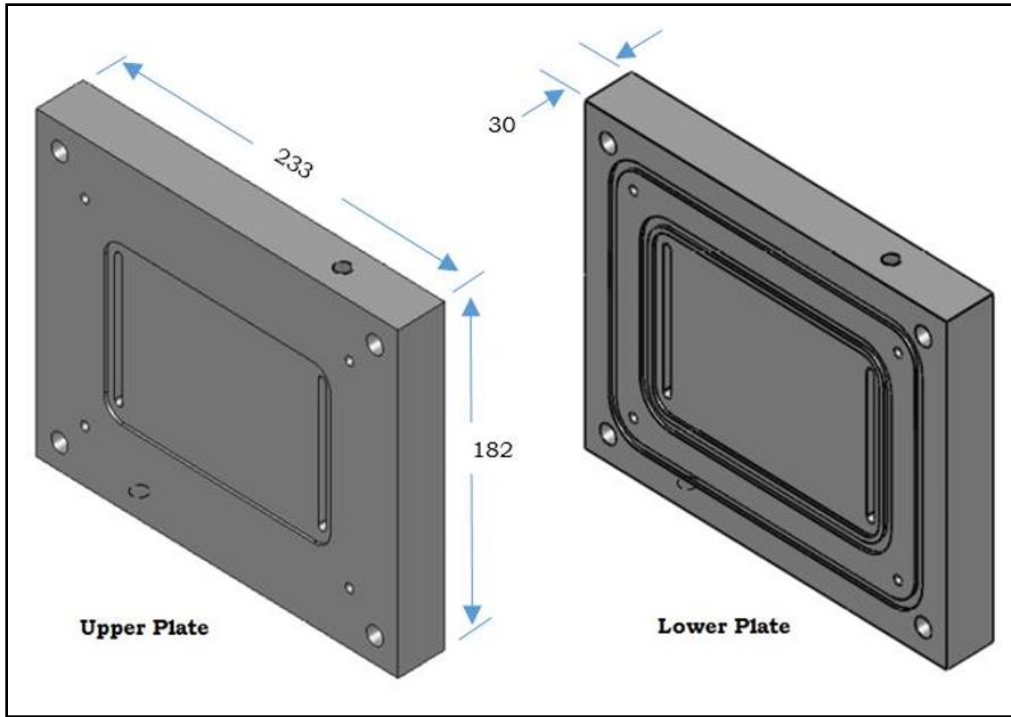


Figure 27: The membrane distillation flat-sheet module schematic diagram (dimensions in mm) [144].

The coupon of the membrane of area 270.7 cm^2 , is placed over a spacer on the bottom plate feed manifold inner O-ring. As shown in Figure 28.

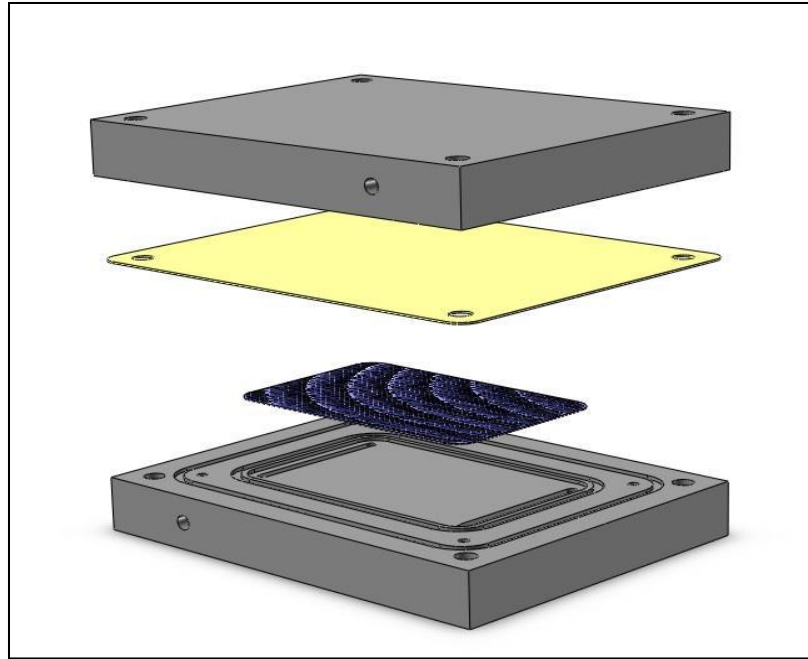


Figure 28: Presentation of the position of the spacer and membrane coupon in a view diagram of the MD unit [144].

Figure 29 illustrates the MD module inner parts including the inlet and outlet flow channels. The inner O-ring is used to prevent the hot and the cold streams from mixing, and both the inner and outer O-rings are used as sealants to avoid leakage. The unit leakage is further prevented by attaching clamps on the top of the MD module, as shown in Figure 30. At the corners of the bottom plate, in between the outer and the inner O-rings, the four guide pins made of stainless are placed to align the plate and the membrane coupon together. Then the two flexible Teflon plates are held together by the Allen screw nuts and bolts, in which four washers are used to distribute the screws load on the plates. Moreover, the function of the spacer used is to increase turbulence of the flow.

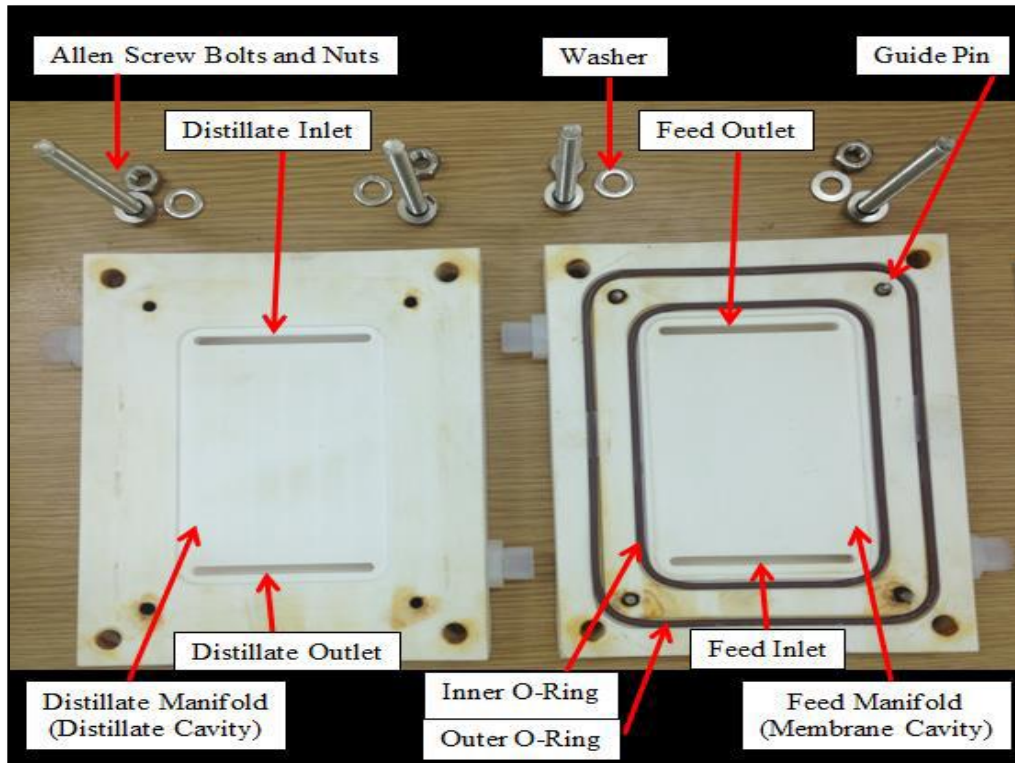


Figure 29: The inner parts of the bottom and the top plates of the MD unit.

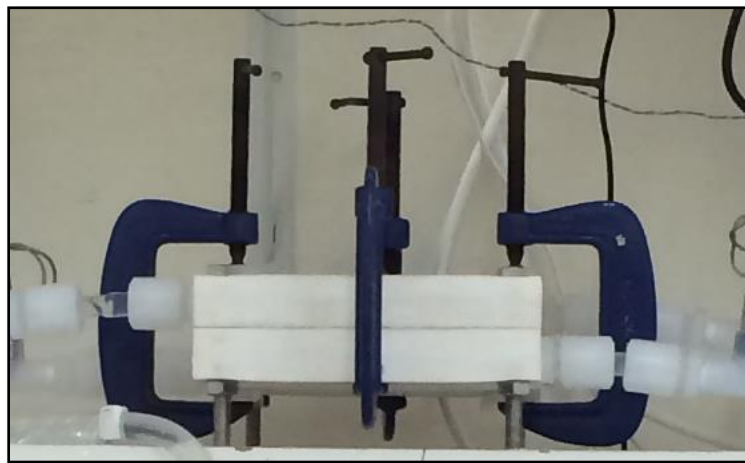


Figure 30: The MD unit from outside with the leak-proofing clamping shown.

The ports for the inlet and outlets of the feed and permeate placed in the top and bottom plates are made using National pipe thread (NPT) standards. In order to prevent stream leakages, the channels are sealed. The feed solution flows in the mid of the bottom plate over the feed manifold in a tangential regime across

the surface of the membrane in which the feed that evaporates get distilled, while the remaining is recycled back to the feed tank. The same closed loop flow regime applies to the permeate in the top plate, in which the cold water is forced to move to the outlet located in the opposite side into the distillate reservoir.

4.5 The MD module construction materials

The parts of the MD unit described earlier, are made up of different materials. Teflon polytetrafluoroethylene (PTFE) polymer material was selected for the body of the MD unit. Since Teflon has many advantages over other polymeric materials, most importantly its high thermal and chemical resistances. Moreover, it supports the MD design to make it more energy efficient as it avoids losses of heat from the system. Other Teflon advantages are listed below [145]:

- The material is non-stick.
- Resistance to numerous chemicals.
- Low friction coefficient.
- High hydrophobicity.
- Can perform under extreme temperatures (-240C – 260C).

The material of construction used in the O-rings is Viton of diameter 2mm. This material is made of elastomer synthetic rubber with fluorocarbon polymers. The advantages of Viton seals are listed below [146]:

- High temperature limits (-23°C – 204 °C).
- High degradation resistance of many chemicals and fluids, compared with other commercially available rubber materials.
- High resistance to oxidation.
- High resistance to burning.
- Very low permeability to substances.

The fittings used in the inlet and outlets steams are fabricated of ethylene-tetra-fluoro-ethylene (ETFE) and Teflon nuts of perfluoroalkoxy (PFA). These materials are highly resistant to corrosion and can tolerate high temperatures and pressures [146].

4.6 The MD module dimensions

The length, width, and height of each plate in the MD unit is 233 mm × 182.8 mm × 30 mm, respectively. More details are depicted in Figure 31 and Figure 32.

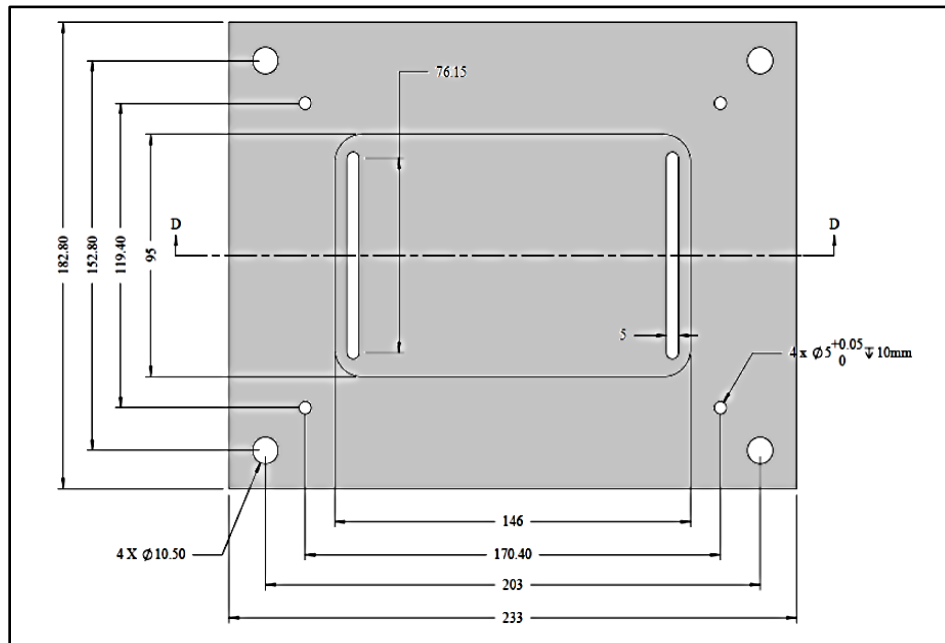


Figure 31: The DCMD module plate dimensions from the outside in millimeters [144].

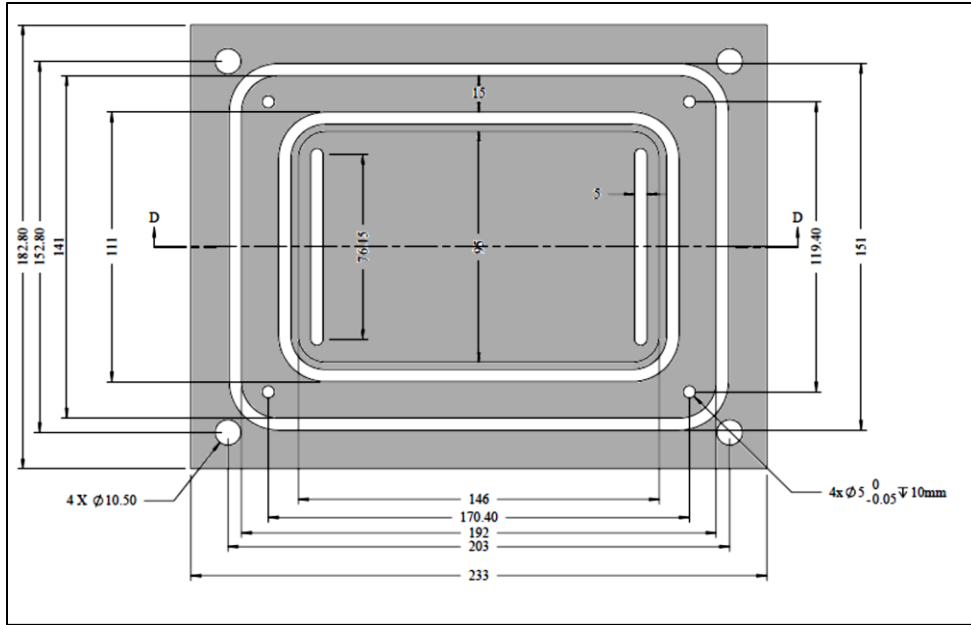


Figure 32: The MD compartment dimensions from the inside in millimeters [144].

The membrane cavity length is 131 mm and depth is 2 mm. Likewise, the grooves depth for the 2 mm diameter O-rings is 2 mm to prevent water leakage. Figure 33 demonstrates the proportions of the plates sides.

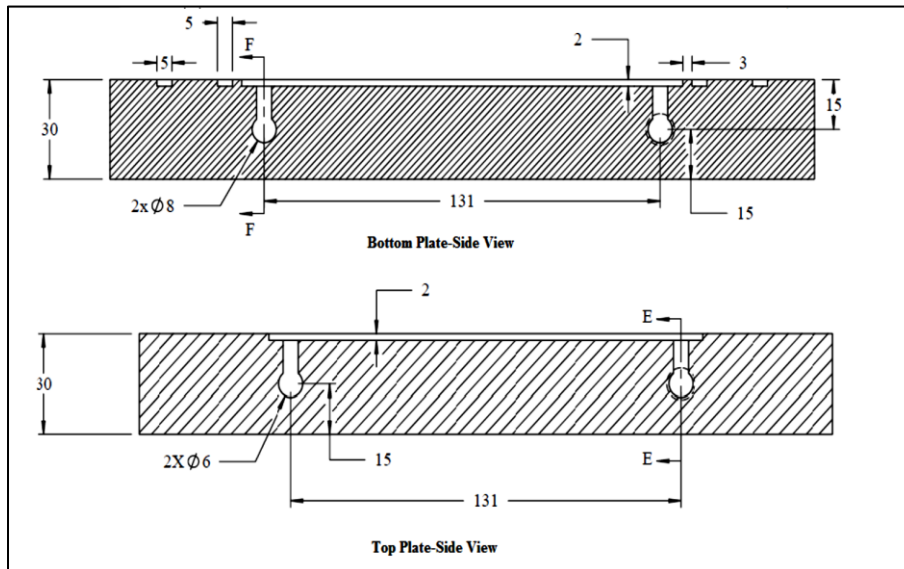


Figure 33: The dimensions of the plates from the sides [144].

4.7 Auxiliary equipment details

In this section, some of the details of the auxiliary equipment in the DCMD unit are presented along with their functions. The auxiliary equipment used in this study include: Heater and cooler, two pumps, two weight balances, digital thermometer sensor and data acquisition system.

4.7.1 Heater and cooler

The heater was used to heat the feed (seawater) in a heating bath circulation. While, the permeate (distillate) was cooled in a refrigerating bath circulation. Table 5 presents the specifications of the heating and refrigerating circulators.

Table 5: The specifications of the heater and cooler used [147].

Model	Julabo, F32-MA, Germany
Temperature range/ Stability	(-35 °C, 200 °C)/ ± 0.02 °C
Dimensions (L x W x H)	42 x 31 x 64 cm
Heating capacity	2 kW
Filling volume	2 L

4.7.2 Pump and tubing

Peristaltic pumps used to deliver the feed to the heater and the distillate to the cooler before reaching the MD unit. The reasons behind selecting this type of pump are their low maintenance requirements, high volumetric precision, and easy flow control and cleaning.

The peristaltic pump used is supplied by Thermo Scientific (FH100X). The pump is controlled digitally.

Table 6 list the peristaltic pumps specifications used in the MD system.

Table 6: The peristaltic pumps specifications [148].

Dimensions (W x L x H)	27.9 x 31.7 x 15.2 cm
Operating Temperature range	(0 - 40) °C
Flow capacity	14 - 4000 mL/min
Revolution per minute	4 - 400
Speed regulation	±0.25 %

The tubing used to connect the feed tank and the heater through the peristaltic pumps was flexible Vincon tubing supplied by Saint Gobain, USA. More details and specifications are shown in Table 7.

Table 7: The tubing specifications used in the MD unit [149].

Type	Vincon (PVC)
Color	Clear
Outer diameter	14.3 mm
Inner tubing diameter	9.5 mm
Wall thickness	2.4 mm
Operating Temperature range	(-43 °C, 74 °C)
Tensile strength	16.9 MPa

4.7.3 Digital balance

The digital balances were used in the purpose of monitoring the changes in weight of the feed and distillate throughout the experiments. Additionally, the distillate weight balance was also connected to the data acquisition system to eventually determine the distillate flux. Table 8 shows the specifications of the NewClassic precision balances (MS4002SDR, Mettler Toledo, US) used in the MD process.

Table 8: The digital balance specifications [150].

Balance dimensions (W x L x H)	194 x 347 x 96 mm
Weight pan dimensions	170 x 200 mm
Readability	0.01/ 0.1 g
Capacity	820/ 4200 g

4.7.4 Temperature sensors

Four thermocouples were implanted with insulation to the feed and distillate inlet and outlet streams, the temperatures were measured manually using a digital display thermometer (Model 421502 Dual Input Type J/K), by connecting the thermocouples with the thermometers' input jacks. The specifications of the digital thermometer are shown in Table 9.

Table 9: The specifications of the thermometer and thermocouples used in the MD system [151].

Display	5 digits LCD
Accuracy	± 0.05
Temperature range	(-200 to 1370) °C
Supplied thermocouples	Type K, Teflon insulation Maximum insulation temperature: 270 °C

4.7.5 Conductivity meter

Measuring the conductivity of the distillate is important to judge its quality. The conductivities of the distillate and feed before and after each run were measured to keep track on the ion content. A conductivity meter SD 320 Con (IP 67 waterproof) was used, its specifications are presented in Table 10.

Table 10: The specifications of the conductivity meter used [152].

Conductivity measurement range	(0 – 5000) $\mu\text{S}/\text{cm}$
Temperature range	(-5 – 150) °C
Accuracy	± 0.5 % of reading

4.7.6 Data acquisition scheme

The weight data collection was done by data acquisition system. A freeware software known as (serialporttokeyboard) was installed in the PC that was connected to the digital balance via a serial port

cable to transfer the distillate tank weight measurements from the balance directly into the PC. The distillate weight was recorded every 30 seconds. The data collected were saved as ASCII format using Microsoft Notepad and processed into flux results using Microsoft Excel Spreadsheet.

4.8 Experimental method

This section outlines the experimental operation along with the procedures of measuring the quality of distillate water (ICP) and membrane autopsy techniques that were carried out to achieve the objectives of this study. Membrane autopsy techniques include characterizing membrane fouling by (SEM, EDX) and the surface contact angle measurements of the used membranes to detect the hydrophobicity loss. The same autopsy techniques were applied to used membranes after the use of antiscalant.

4.8.1 Experimental operation

Numerous experiments were performed at different operating conditions, using seawater as the feed solution and deionized water in the distillate tank. The replacement of the membrane for the selected parameters, was done after (45-91) hours in total of subsequent batch experiments each of (4-5) hours of operation. It is worth mentioning that in real operation more than the effective time mentioned was needed for each run, for the desired temperatures to be reached, ~~and cleaning of the tanks after each run from deposits.~~ Moreover, the membrane replacement procedure includes the open-up of the MD module to be cleaned and the membrane is washed with deionized water, then its allowed to dry to be sent for membrane autopsy. The flux data is what adopts the replacement of the membrane. Since, the weight data collected from each batch are used to generate a flux graph. Furthermore, the flux graphs obtained under the same operational conditions using the same membrane are merged together, until the permeate flux reaches almost zero membrane replacement can take place. The time it takes to be able to replace the membrane depends on the operation conditions chosen. The DCMD system operated under ambient pressure and the same permeate inlet temperature (20 °C) for all runs. A summary of operating conditions in this work is presented in Table 11 where the experiment code is a number with four digits

representing the feed temperature and flowrate. For example, the feed temperature of 50 °C and flow rate of 1.5 L/min is represented as 5015.

Table 11: The parameters selected with the total operation time of the experimental batches in the lab scale DCMD system.

Feed/permeate Flowrate (L/min)	Feed inlet Temperature (°C)	Experiment code	Total operation Time (hr)
1.5	50	5015	91
	60	6015	63
	70	7015	49
2.5	50	5025	56
	60	6025	53
	70	7025	45

Due to the lengthy nature of the experiments, it was not possible to repeat all the runs. However, some of the experimental runs were repeated to establish the reproducibility. The operational condition of experiment code 6025 was selected randomly, for the experimental runs to be repeated. It was found that the initial permeate flux obtained was the same for both graphs with comparable average values and relatively low standard deviations.

4.8.2 Antiscalant

The antiscalant is a chemical additive that was added to the feed solution at the beginning of each run, to investigate its capability to mitigate membrane fouling. Several antiscalants were considered for potential utilization. However, in this study antiscalant Performax 3-S200 was provided with samples and data-sheet which highlighted its thermal stability. Antiscalant Performax 3-S200 (supplied by Ashland Hercules Water Technologies, USA) was injected using a pipette to the seawater feed in a dose of 4ppm (within manufacturer recommended range). The chemical exact composition of the antiscalant is confidential. However, it is quoted as a modified polycarboxlyte that is free of phosphorus and nitrogen that is non-toxic, calcium tolerant and strong dispersing polymer especially in low flow areas. The molecular weight of this antiscalant was designed for scale control of high temperature application without Ca-polymer precipitation risk, that is applicable for the thermally driven MD desalination process (Appendix A: Antiscalant datasheet). Some physical properties are presented in Table 12. The selected set of experiments of different operational conditions are presented in Table 13. The letter A is added to the experiment code as an indication of experimental runs with added antiscalant.

Table 12: Physical properties of PERFORMAX 3-S200 antiscalant.

Density	1200 (kg/m ³)
pH	6
Freezing point	< 0 °C approximately
Solubility	Miscible with water in all proportions
Color	Yellowish

Table 13: The operational conditions for the set of experiments with added antiscalant.

Feed/ permeate flowrate (L/min)	Feed temperature (°C)	Experiment code
1.5	60	6015 A
2.5	60	6025 A
1.5	70	7015 A

4.8.3 Measurements of contact angle (CA)

The contact angle of the membrane active layer was measured after each experiment, in order to investigate membrane wettability from the degree of loss of hydrophobicity. The CA measurements were carried out with a KRUSS DSA25 drop shape analyzer along with the ADVANCE innovative software that provided a live camera image display and a workflow of the analysis even for inclined surfaces [153]. The sessile drop method was selected from the software to calculate the deionized water adhesion to the surface by fitting the shape of the drop captured to Young-Laplace equation. The deionized water dosing was controlled automatically by the software employing a syringe perpendicularly placed above the membrane surface. The needle used in the syringe was made of PP with lock connector and the needle diameter was 0.7 mm. The KRUSS drop shape analyzer used in the Chemical Engineering Research Laboratory at Qatar university is shown in Figure 34.

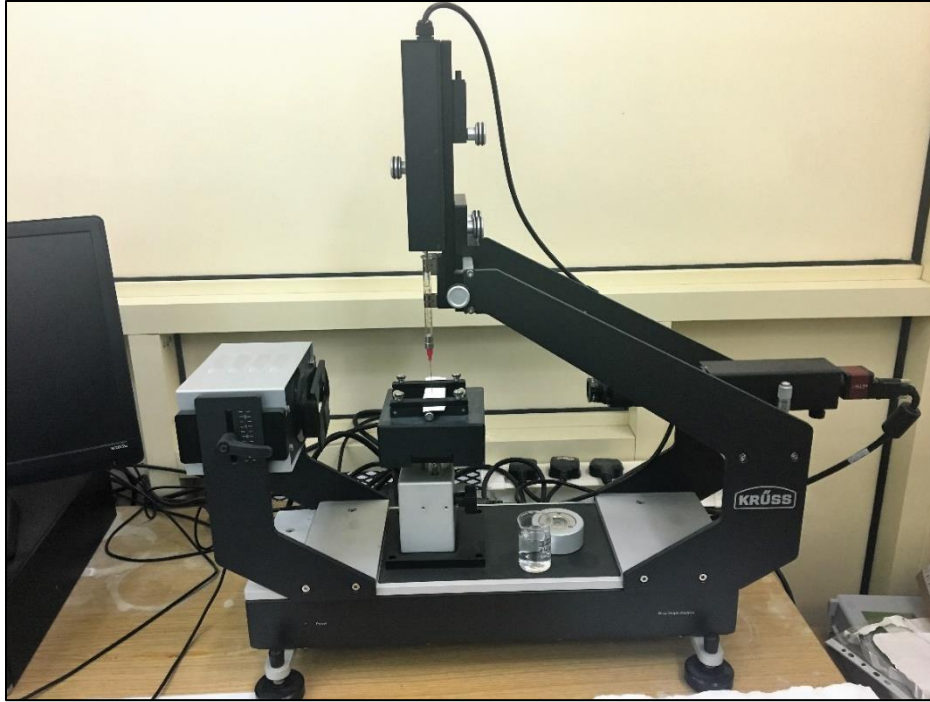


Figure 34: The drop shape analyzer KRÜSS DSA25 used for CA measurements.

The membrane was cut into rectangles from different sites and placed in a membrane holder as shown in Figure 35. The contact angle measurement was automated and consisted of repeated measurements until consistent values are obtained using a built-in statistical routine.

The distilled water drop was brought into contact with the membrane surface to perform the measurement. For convenience, the site portions of the membrane surface near the inlet, outlet and mid were labeled (IN), (OUT), and (MID), respectively. The average value of all the sites of each membrane used was then calculated.

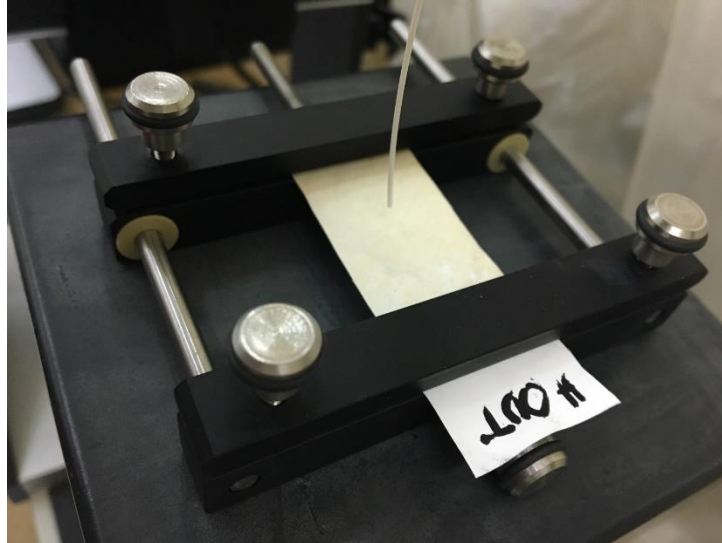


Figure 35: The membrane holder with a sample membrane shown.

4.8.4 SEM-EDS physical characterization

The scanning electron microscope (SEM) was used to view the membrane surface structure and morphology. SEM was attached with energy dispersive spectrometry (EDS) that was used to analyze the composition of the elements on the fouled surfaces. However, in this study it was difficult to view the membrane cross-section or the thickness of the fouled layer since the membrane should be frozen by liquid nitrogen, and cut into a small piece in order to fit the sample holder in the SEM apparatus. The SEM imaging with different magnifications along with the EDS were done using an FEI Quanta 200 instrument in Qatar university at the laboratory of central unit.

4.8.5 Water Quality Experiments

Cations analysis was assessed to study the quality of distillate using inductive coupled plasma- optical emission spectrometry (ICP-OES). The result of ICP analysis was done for (Ca, Mg, Na, K, and Sr) cations. The distillate samples were sent to the chemical engineering laboratory for analysis. The samples were prepared by acidification by 2% of HNO₃. The instrument used was Thermo (ICP-OES) model iCAP-6500

and the reference methods of analysis was the Standard methods for the examination of water and wastewater, EPA Method No. 3120B Metals by Plasma Emission Spectroscopy. In general, the analysis was achieved by first preparing blanks. The preparation of these blanks was done by using ultra-pure water with 100 mL added nitric acid. Along with the blanks several standards were prepared and then placed in the ICP-OES auto-sampler rack with the samples to be analyzed using a compatible ICP-OES software.

4.8.6 Method for flux decline and salt rejection

The flux decline measurements are used as indication of fouling and scaling taking place, as explained in section 3.4.2, using Eq. 11 by utilizing the data acquisition system that translated the recorded weight into flux data using excel spreadsheet. Moreover, the quality of the distillate, and the degree of contamination by the feed is quantitatively expressed in terms of salt rejection percentage. It can be calculated using Eq. 12. Where, the conductivity of the seawater and the distillate were measured after each experimental run of the batch processes.

5 Results and discussion

In this chapter, the results of the experimental work conducted will be presented and discussed. The experiments performed were designed to investigate the effect of fouling and wetting on extended runs performances using Accurel polypropylene membrane within a variety of operational conditions. Moreover, the effect of adding antiscalant as a mitigation method was studied.

The main sections of this chapter include:

- 1- The flux performances at different operational conditions.
- 2- The effect of added antiscalant on the flux performances.
- 3- Membrane wetting investigation.
- 4- SEM-EDS physical characterization of used membranes.

5.1 Flux performances

The main purpose is to study the distillate flux profiles obtained at different operating conditions for extended runs performance to elucidate the effect of fouling and wetting on the MD process. The percentage decline in flux is an indication of the induced average rate of fouling as discussed previously in section 3.4.2. The feed solution used for all runs was seawater, and the membrane utilized in the experiments in the DCMD bench scale unit was made of polypropylene with pore size of 0.2 microns and a porosity of 73-75%. The active area available for membrane distillation was 0.0014 m². More details were presented in section 4.6, along with the experimental procedures. The effect of varying feed temperature and feed flowrate on the MD flux performance are studied herein.

5.1.1 The effect of the feed temperature on the extended runs performance of MD.

The flux performance results are shown in Figure 36, Figure 37 at operating conditions presented in Table 11.

Figure 36 shows that at a constant distillate temperature of 20 °C and a feed flowrate of 1.5 L/min, the increase of feed temperature from 50 °C to 70 °C led to a significant increase in the permeate flux initially. The maximum permeate flux of (37.2 L/m².h) was achieved at the temperature of 70 °C. Whereas, reducing the feed temperature from 70 °C to 50 °C reduced the permeate flux by 58 % of the initial flux. This can be explained in terms of Antoine equation Eq. (3), where the partial vapor pressure that represents the driving force of the MD process for vapor mass transport increases exponentially with an increase in temperature difference. This is consistent with many reported permeate flux results in the literature [65, 71, 107].

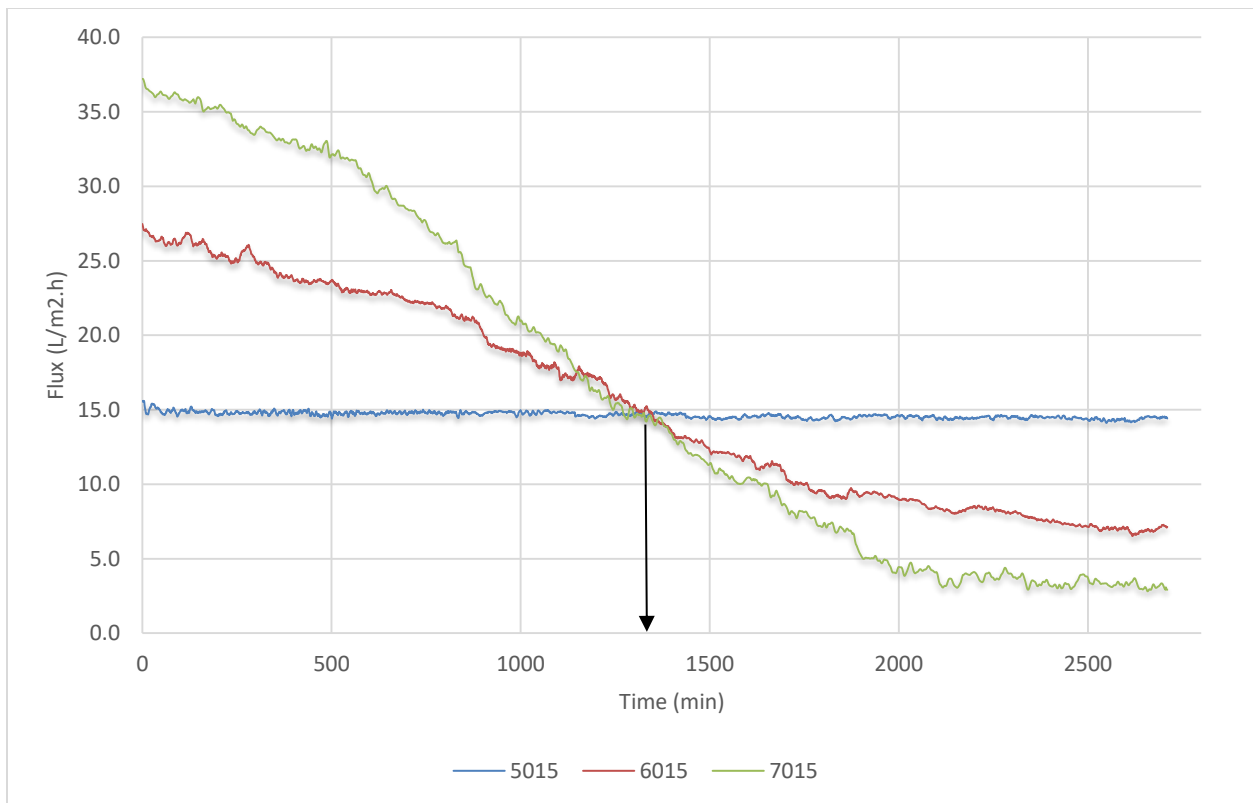


Figure 36: The flux profiles obtained at $q_f = 1.5$ L/min, where $t_f = 50-70$ °C, and $t_p = 20$ °C.

However, the decline in flux increases more rapidly at the higher operating temperature. Figure 36 illustrates that at feed temperature of 70 °C during 17 hours of operation the permeate flux was decreased by 43.5%, while for the same duration the permeate flux decreased by 31.6% for feed temperature of 60 °C. This can be explained by an increased potential of fouling with increase in flux, which will lead to an increase in the heat transfer resistance caused by the fouling layer formed on the surface of the membrane; eventually lowering the driving force and reducing the active area for vapor transport.

Furthermore, as indicated by Eq. (10), for similar mass transfer coefficients of the salts in the feed (same flowrate) it is expected at a higher flux (due to the higher operating temperature) to have a higher degree of concentration polarization, implying a higher potential of scale formation. Moreover, the heat transfer resistance of the membrane induced by the fouling layer (mainly due to the precipitation of the salts) at the interface will further decrease the driving force; eventually reducing the flux more rapidly at a given flowrate. Moreover, since the feed temperature of 50 °C is considered to be relatively low, a lower degree of concentration polarization is expected according to Eq. (10) thus the permeate flux produced was nearly constant.

As scaling occurs the deposit layer on the membrane surface will have two negative effects: reduction of the active area of the membrane with potential of pore blockage, and an additional thermal resistance which enhances the concentration polarization thus reducing the flux.

After 23 hours of operation the flux curves crossed each other and past the crossing point (depicted by an arrow in Figure 36) it can be noticed that the decline in flux is less pronounced. This can be explained by the fact that the formed compact deposit layer enhances the temperature polarization effect in terms of diminishing the rate of scale formation, due to the inverse solubility of the predominant salts such as CaCO_3 and CaSO_4 , as designated from the SEM-EDS analysis in section 5.3.

Moreover, the layer of fouling formed will persist in reducing the permeate flux as a result of the reduced active area of the membrane until it declines to almost zero.

The average fouling rates presented in Table 14, depict the percentage of flux decline per hour. At feed flowrate of 1.5 L/min the average fouling rate was higher for higher feed temperature. This result is consistent with the result found by Gryta [71]. A possible explanation can be in terms of the reduced flux contributing to a higher concentration polarization due to inverse salt solubility in the feed stream with increase in temperature translated to a significantly higher fouling rate. Due to the low average fouling rate obtained at feed temperature of 50 °C, the permeate flux decline was low compared to the higher feed temperatures.

Table 14: The average fouling rate at the operational conditions employed.

Temperature (°C)	Average fouling rate at 1.5 L/min (%flux decline/hr)	Average fouling rate at 2.5 L/min (%flux decline/hr)
70	2.04	2.05
60	1.64	1.74
50	0.16	0.19

Figure 37 depicts that the highest flux obtained was at temperature of 70 °C (40 L/m².h). Accordingly, the significance of feed temperature effect on the level of permeate flux produced was confirmed at the higher flowrate, referring to the exponential increase in the driving force of the MD process with respect to increase in temperature. However, Figure 37 shows that decreasing the feed temperature from 70 °C to 50 °C caused a similar reduction in the initial permeate flux (60%) when compared with that of the lower feed flowrate (58%) shown in Figure 36. Thus, it can be inferred that the effect of varying the feed flowrate on the initial permeate flux is minor compared to the effect of varying the feed temperature.



Figure 37: The flux profiles obtained at $q_f = 2.5$ L/min, where $t_f = 50-70$ °C, and $t_p = 20$ °C.

Moreover, Figure 37 shows the occurrence of a crossing point shared by the permeate flux curves and past that point the flux decline was reduced. Similar pattern in this perspective was shown in Figure 36. Moreover, the arrow in Figure 37 depicts the point where all the flux profiles crossed after 16 hours of operation using the higher feed flowrate, which is 7 hours earlier from the crossing point that took place at the lower flowrate (Figure 36). However, the permeate flux profiles shown in Figure 37 are slightly different than the flux profiles shown in Figure 36. Where Figure 37 indicates that prior to the crossing point the flux curves of feed temperatures 70 °C and 60 °C show clear induction periods, thereafter the fluxes decline rapidly. Unlike the flux curves obtained at the lower feed flowrate shown in Figure 36, where the permeate fluxes declined gradually with indistinct induction periods. Moreover, the interaction of the mixed salts with each other and with the membrane in the seawater feed effect significantly the

thermodynamics and thus the propensity to fouling [88]. Therefore, it is difficult to predict the induction periods for salts precipitations.

The induction period at feed temperature of 60 °C (14 hours) is almost double the induction period at feed temperature of 70 °C (6 hours), as depicted in Figure 37. This can be due to increased fouling rate and concentration polarization effects, where the main constituent on the surface of the used membranes was CaCO₃ as depicted in the SEM-EDS of Figure 52, Figure 54 and Figure 56 in section 5.3, which exhibits an inverse solubility with respect to temperature. Thus, the higher the temperature the higher the rate of precipitation; reducing the driving force for the MD process. Further explanations on the effect of varying the feed flowrate on the performance of MD will be elaborated in section 5.1.2.

Similar average fouling rates were obtained using feed flowrate of 2.5 L/min as depicted in Table 14 when compared to the ones obtained at flowrate of 1.5 L/min. Thus, it can be deduced that the feed flowrate has a minimal effect on the overall permeate flux decline rate caused by fouling.

5.1.2 The effect of the feed flowrate on the extended runs performance of MD.

The effect of feed flowrate on flux performance at operating conditions shown in Table 11 are depicted in Figure 38, Figure 39 and Figure 40.

In section 5.1.1 the temperature effect on the flux performance indicated that the flowrate had a minimal impact on the initial flux. Nevertheless, Figure 38 depicts that the flowrate affects the initial permeate flux to some extent at operating temperature of 50 °C. Moreover, fractional flux decline was observed at longer operating times but it can be considered negligible. Figure 38 indicates that at a feed flowrate of 2.5 L/min the overall flux was maintained at a slightly higher value of 17 L/m²h, when compared with the flux obtained at the lower feed flowrate of 1.5 L/min (15 L/m²h). However, the rate of reduction in the permeate flux at 2.5 L/min is slightly higher than that observed at 1.5 L/min. Despite the fact that increasing flowrate leads to a reduction in temperature polarization as described in Eq. (9) in section 2.3;

implying an increase in the temperature at the boundary layer leading to a higher permeate flux, the scaling potential increases due to the increased flux rising the concentration polarization phenomena. Thus, at a higher flowrate the flux decline is induced by increased fouling potential (CP). Nevertheless, this effect is minor due to the low operational feed temperature. Since the permeate fluxes obtained are low compared to those obtained at higher temperatures, the effect of partial increased flux on concentration polarization and scaling potential is low. This result is supported by observations on the SEM images (Figure 51, and Figure 57) showing partial surface coverage, and scattered scale where CaCO_3 being the main constituent exhibiting inverse solubility.

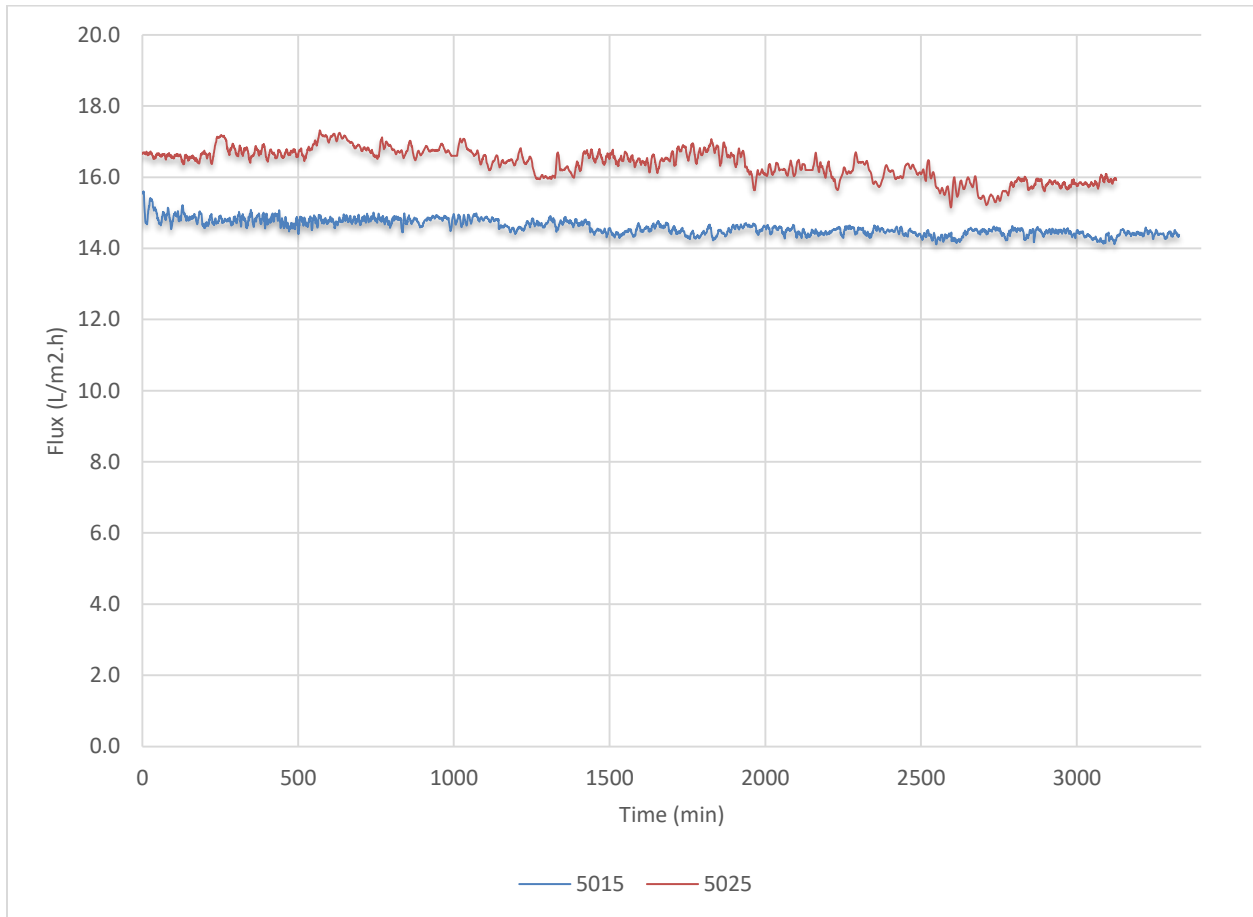


Figure 38: The effect of varying the feed flowrate at $t_f=50\text{ }^\circ\text{C}$, and $t_p=20\text{ }^\circ\text{C}$.

Moreover, the overall average fouling rate (0.19 %flux decline/hr) was not affected as depicted in Table 14. Accordingly, at a temperature as low as 50 °C the rate limiting step is the heat transfer resistance of the thermal boundary layer, which is low compared to the heat resistance of the fouling layer [9]; hence the flux was maintained almost constant with negligible deterioration.

Depending on the operating temperature, the effect of feed flowrate in improving the flux becomes less pronounced, since the thermal resistance of the scale layer formed with higher running temperature becomes much greater than the thermal resistance of the boundary layer. This concept was presented in section 3.4. Moreover, Figure 39 depicts that the flux decline was more rapid for the higher feed flowrate. In addition to concentration polarization effect, the heat loss by conduction, particularly when using DCMD configuration will be introduced [34]. Theoretically heat loss by conduction is expected to increase by the use of higher operating feed flowrate, due to the enhancement of thermal efficiency [65]. Thus, the heat transfer coefficient in the feed side is enhanced, and an increase in the overall temperature difference between the feed and the permeate sides is expected, enhancing the driving force for vapor transport; that should be translated to a higher flux. However, it is expected that the thermal conductivity of the membrane to increase with increased flux [114], hence heat conduction through the membrane wall is facilitated. As result of heat loss by conduction and according to Eq. (9) TP also is expected to increase what lead to the scattered less compact scale formation, due to the inverse solubility of the main constituent CaCO_3 .

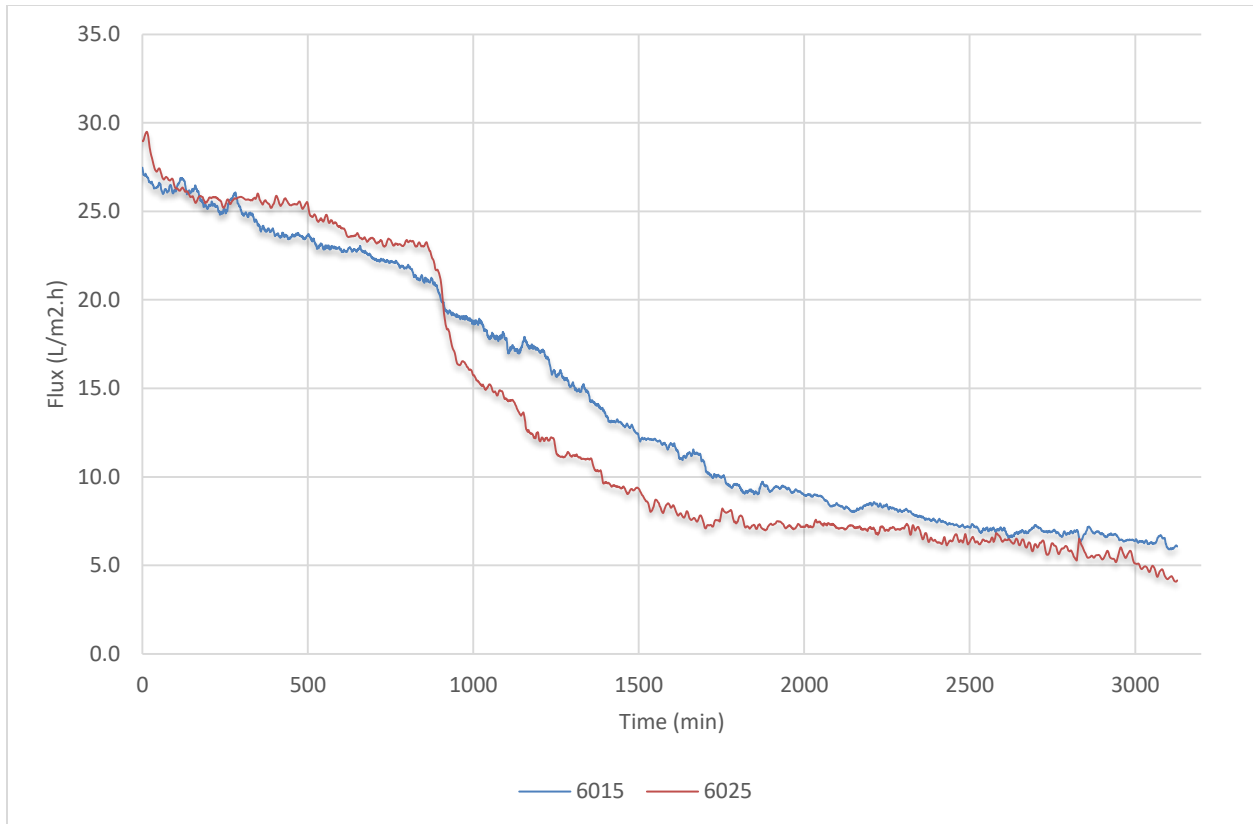


Figure 39: The effect of varying the feed flowrate at $t_f=60\text{ }^\circ\text{C}$, and $t_p=20\text{ }^\circ\text{C}$.

Nevertheless, the average fouling rate was almost the same ($\sim 1.7\%$ flux decline/hr) as depicted from Table 14, which is consistent with the conclusions brought by the literature [71, 114, 116] that there could be an optimum feed flowrate for each MD module, where further changes in the flowrate will not cause considerable changes in the overall flux decline.

Despite that at a higher feed velocity the fouling tendency is higher, due to enhancement in the concentration polarization phenomena, surface renewal and more shear water action on the surface is expected to lower the potential of the scale to form and adhere to the surface. Moreover, due to the turbulence caused by the increased flowrate an increase in flux (reduced boundary layer) is expected. However, the temperature polarization at the surface will be reduced, due to shear actions of the water.

Thus, two negative effects are expected. First, increased potential of scale formation, since the main salts exhibit inverse solubility. Second, increased potential of heat loss by conduction reducing the thermal efficiency and the driving force eventually leading to more flux decline.

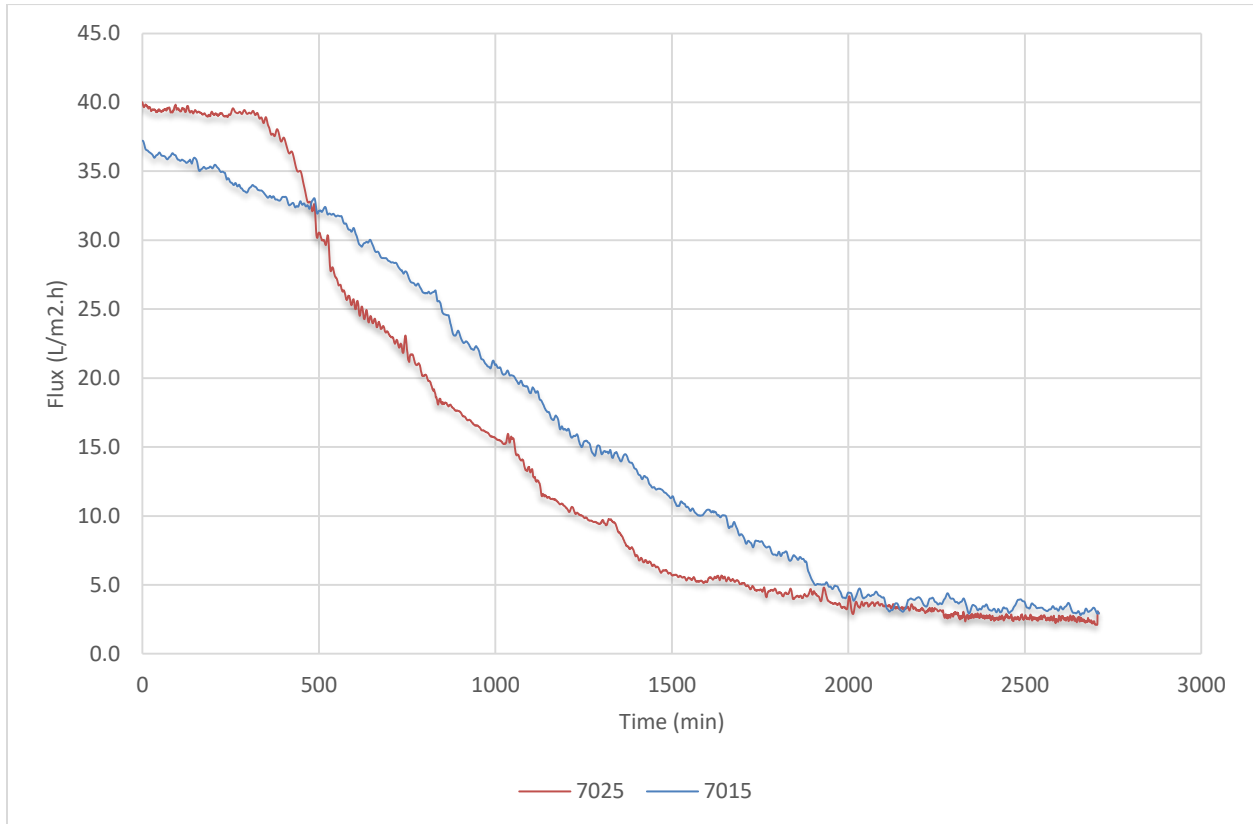


Figure 40: The effect of varying the feed flow rate at $t_f = 70\text{ }^\circ\text{C}$ and $t_p = 20\text{ }^\circ\text{C}$.

The flux was higher initially, for the higher feed flowrate, since the heat and mass transfer coefficients are directly affected by the feed flowrate. However, after an induction period of 6 hours the flux started to decline more rapidly for the same reasons explained for Figure 39. Moreover, the lower induction period obtained compared with the lower temperature of $60\text{ }^\circ\text{C}$ (14 hours) at feed flowrate of 2.5 L/min as shown in Figure 40 may be due to the increased thermal conductivity of the membrane at the higher permeate

flux [65], and increased fouling rate brought by the increase in temperature as explained in section 5.1.1 in more details. Moreover, the slight increase in flux observed following the induction period at the lower flowrate may have been contributed by the partial membrane wetting caused by the CaSO_4 co-precipitation with CaCO_3 [9, 107].

The average fouling rate was high and the same ($\sim 2\%$ flux decline/ hr) as depicted in Table 14, despite the flux decline behaviors observed in Figure 40, because the feed flowrate influences the boundary layer which is a small thermal resistance. However, when scale formation take place on the membrane surface the thermal resistance of this scale layer will become greater than the resistance of the boundary layer. The same argument applies to mass transfer resistance, where the mass transfer of vapor will be reduced eventually.

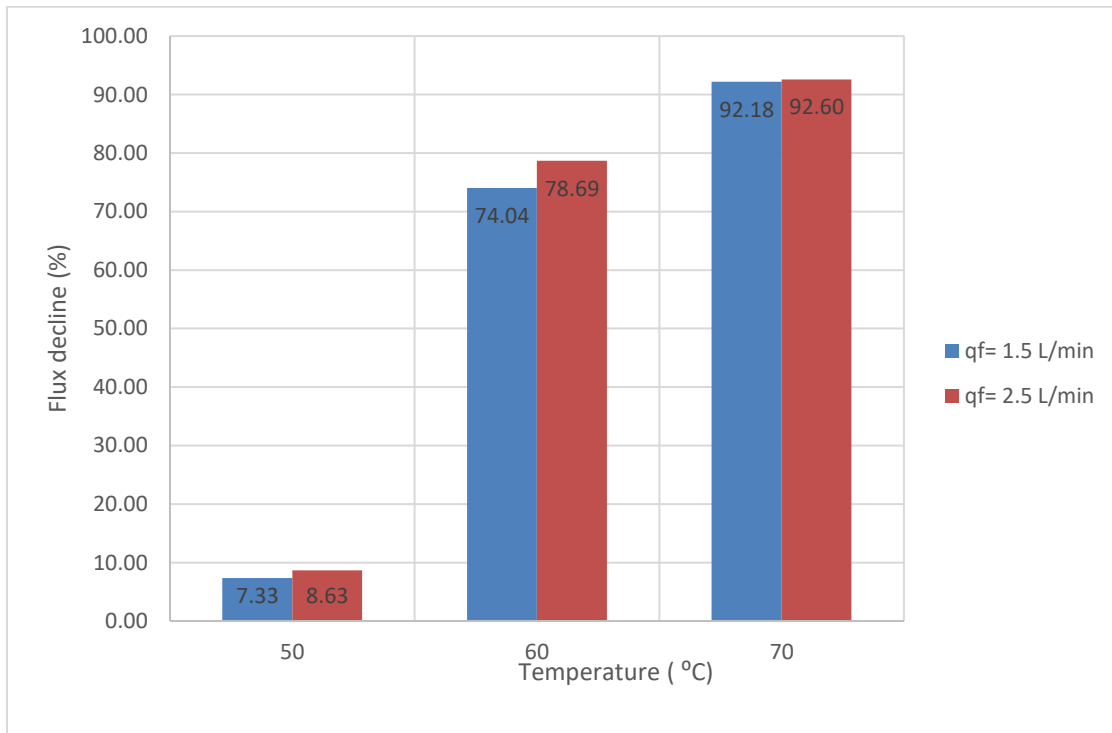


Figure 41: The overall flux decline percentage after 45 hours of operation for $t_f = (50-70\text{ }^\circ\text{C})$, $t_p = 20\text{ }^\circ\text{C}$ and $q_f = 1.5, 2.5\text{ L/min}$.

Figure 41 depicts that the percentage of the overall flux decline increases with an increase in temperature. After 45 hour of effective operation, at feed flowrate of 1.5 L/min the flux decline percentage at feed temperature of 50 °C is only 7.33, while the flux decline percentages at 60 °C and 70 °C are 74.04 and 92.12, respectively.

Moreover, at feed flowrate of 2.5 L/min the flux decline percentage at feed temperature of 50 °C is only 8.63, while at 60 °C and 70 °C the flux decline percentages are 78.69 and 92.60, respectively. The percentages of flux decline for both feed flowrates are very similar. Emphasizing that the feed temperature has a predominant effect on the performance of the MD process (in terms of flux decay) when compared to the feed flowrate effect. However, an increase in the feed temperature from 60 °C to 70 °C led to a less drastic increase in the flux deterioration performance.

Most of the flux profiles depicting decline tend to have three distinct zones (A, B and C) as summarized in Figure 42. This original explanation was established using literature information on MD modeling and experimental evidence from SEM imaging.

Where the flux profile at a higher flowrate is represented in a red curve, while the blue curve represents the flux profile at a lower flowrate for the same feed temperature.

Zone A shows that at a higher feed flowrate more turbulence will promote a higher heat transfer coefficient, due to the reduced temperature polarization (TP) effect. Moreover, higher operating flowrate will lead to the reduction in the thermal resistance of the boundary layer. Thus, a higher driving force for vapor transport at the higher flowrate (red curve) is expected to increase the flux to some extent. It can be inferred that the effect of the thermal boundary layer is dominant in Zone A, represented as (R1 and R4) thermal resistances as explained in section 2.2.2.

Zone B is a transition zone, where the effect of the thermal resistance (R2) due to fouling layer formation

starts to predominate the effect of the boundary layer on the flux performance. Thus, the effect of TP is reduced and inorganic foulants exhibiting inverse solubility will tend to gain a promoted formation tendency. When the fouling layer starts to form, and adhere at the surface of the membrane the effect of CP becomes more dominant, consequently the effect of the thermal resistance of the fouling layer will increase along with a gradual increase in mass transfer resistance. As explained by Eq. (10) the scaling potential is expected to increase exponentially with an increase in flux (J). Accordingly, the flux in red curve (higher flowrate) shown in Figure 42 is expected to decline faster. Moreover, heat loss by conduction through the membrane is expected to increase especially when using DCMD configuration, since increased flux is expected to increase the thermal conductivity through the membrane material (R3). Thus, at this stage both TP and CP effects were increased at the higher flowrate, while mainly CP effect was increased at lower flowrate as distinguished by the compactness of the fouling layer from SEM images at both flowrates.

Zone C shows that the thermal resistance due to the fouling layer dominate (R2). After the transition zone, heat transfer resistance is expected to increase due to the adhesion and compactness of the fouling layer formed on the membrane surface. Where R2 described in Eq. (5) will increase because of increased thickness of the fouling layer; implying also increased mass transfer resistance and reduced thermal conductivity caused by the fouling layer formed. Moreover, the effect of TP in reducing the driving force is further enhanced at both flowrates.

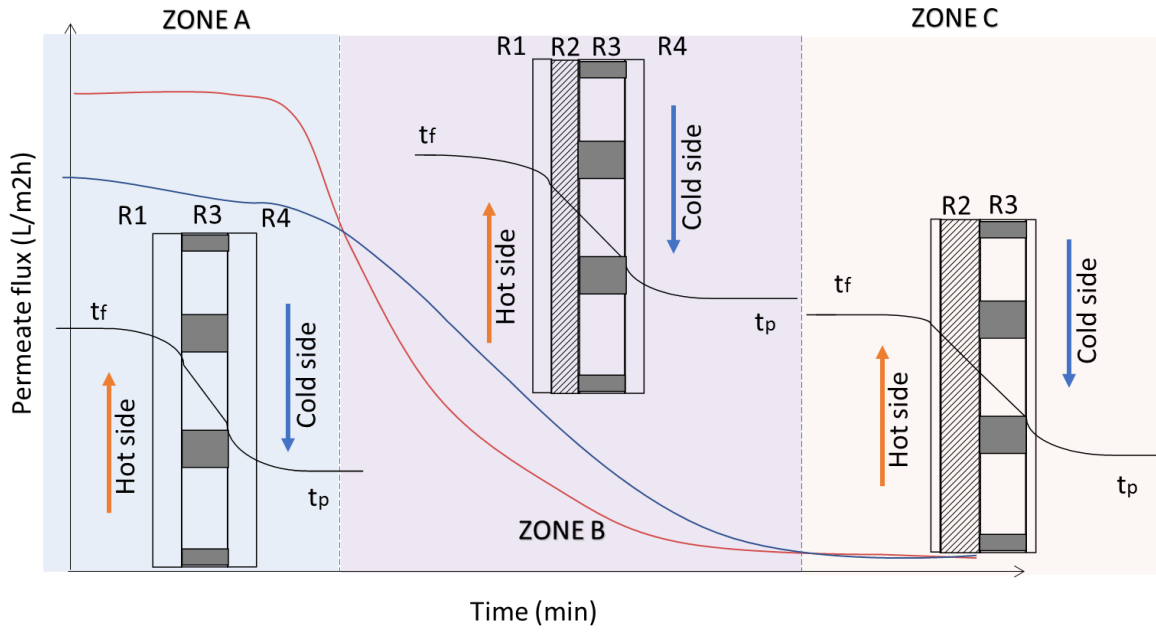


Figure 42: Schematic representation of the main three zones of declining flux profile curves.

5.2 Investigations of membrane wetting

The membranes applicable for membrane distillation uses are hydrophobic in nature. However, wetting of the membrane is induced mainly by foulants penetrating into the interior of the membrane through its pores covering the whole depth, partial depth, or on the surface of the pores only [41]. Depending on many factors such as the residence time, the operating conditions, heat transfer and the feed concentration fouling propensities vary; and so, the opportunity of membrane wettability to penetrate and block the pores of the membrane. The different forms of membrane wetting that may take place according to the degree of damage caused to the membrane, were discussed and summarized in Figure 14. The membrane is hydrophobic when the contact angle is higher than 90° , and super-hydrophobic when the contact angle exceeds 160° [140].

Figure 43 illustrate the contact angle measurement of a virgin polypropylene membrane produced by KRUSS DSA25 drop shape analyzer using the ADVANCE innovative software described in section 4.8.3.

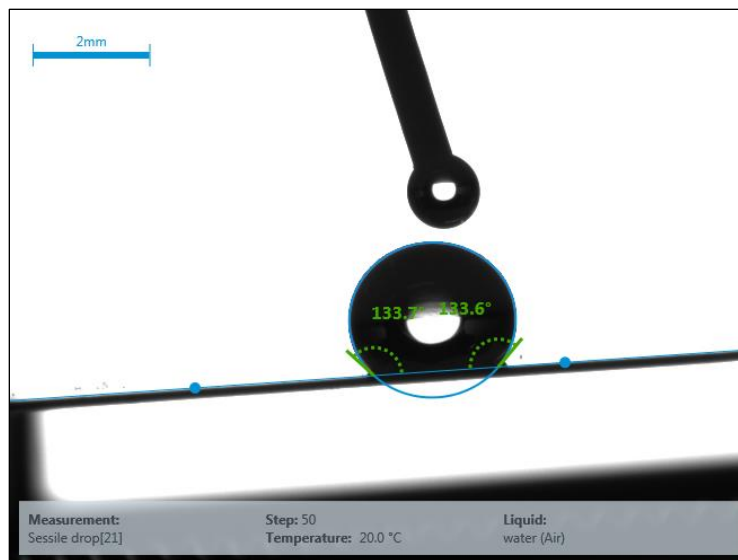


Figure 43: The shape of the deionized droplet and the contact angle on the surface of a virgin flat-sheet PP membrane ($0.2 \mu\text{m}$).

Various measurements of contact angle were performed to insure high accuracy. The values obtained for the CA of the virgin PP membrane are shown in Table 15 along with the calculated average. According to the average contact angle value the membrane can be classified to relatively highly hydrophobic.

Table 15: The virgin flat-sheet polypropylene membrane (0.2 μm) contact angle measurements.

Membrane	Contact angle (CA) ($^{\circ}$)			Average CA ($^{\circ}$)
PP (0.2 μm)	138.2	133.7	131.5	134.5

Table 16 and Table 17 show the contact angle measurements of the fouled membranes. The contact angle measurements and associated labeling schemes are explained in detail in section 4.8.3.

Table 16: The measured contact angles at various sites of the fouled membranes operated at different feed temperatures and at a constant feed flowrate of 1.5 L/min.

Experiment code	IN1	IN2	IN3	M1	M2	M3	OUT1	OUT2	OUT3	Average CA
5015	91.74	98.23	101.84	100.08	100.25	100.95	97.96	92.16	87.44	96.74
6015	103.7	107.13	108.97	103.26	104.7	101.7	96.85	107.72	87.64	102.41
7015	99.89	102.28	103.61	97.39	99.58	99.62	86.19	97.12	97.39	98.12

It is expected that the lowest contact angle measurement is for the membrane with the highest fouling rate and scaling potential, since both are responsible for inducing wetting in the membrane as explained previously in section 3.4.1. Many factors affect the rate of fouling such as the characteristic of the membrane and its properties, the foulant present and their characteristics, and the operational conditions [8]. Similarly, alkaline scaling and crystallization of salts are dependent on the residence time for the scale on the membrane surface, the concentration of the feed, the heat transfer and operational conditions [71]. With the feed temperature having a more pronounced effect on the performance of the MD process as depicted from the permeate flux results (section 5.1.1).

Table 16 shows that the average contact angles of all the fouled membranes are comparable. Although the CA obtained are reduced when compared to the pristine membrane (134.5 °), all CA measurements indicate that the used membranes did not lose their hydrophilicities (> 90 °). Despite that it is expected to have a slightly higher contact angle for the lowest feed temperature (50 °C) used; since the average fouling rate was the lowest (0.14 %flux decline/hr), the operational time under this condition was the highest too (91 hr). Thus, the residence time of the deposits to interact with each other and with the membrane surface was higher and so the expected potential for induced wettability. Nevertheless, it is inferred that only surface wetting took place, since the percentage of salt rejection was the highest (99.94%) depicted in Figure 44, which indicates no signs of full depth penetration of the feed into the distillate side.

Table 17 depicts that the average contact angles measured are reduced by (32-22%) when compared to the pristine membrane (134.5 °). This loss of hydrophobicity indicates surface membrane wetting occurred as illustrated in Figure 14. Since there is no significant contamination of the distillate by the feed, according to the salt rejection values presented in Figure 44 it can be concluded that no partial wetting of

the membrane took place operating at feed flowrate of 2.5L/min. Nevertheless, the contact angle measurements of the experiment code 6025 ($t_f= 60\text{ }^\circ\text{C}$ and $q_f= 2.5\text{ L/min}$) was relatively low occasionally when compared with the other used membranes contact angle measurements, this could be due to measurements error or the selected portions of the membrane to be tested were more fully covered by foulants, since the layer of fouling is unevenly distributed on the surface of the membrane as depicted from the SEM-EDS Figure 55 in section 4.8.4.

Table 17: The measured contact angles at various sites of the fouled membranes operated at different feed temperatures and at a constant feed flowrate of 2.5 L/min.

Experiment code	IN1	IN2	IN3	M1	M2	M3	OUT1	OUT2	OUT3	Average CA (°)
5025	96.05	100.88	106.66	107.3	109.87	109.44	100.9	102.95	103.53	104.17
6025	97.21	94.68	94.85	81.2	78.08	68.62	101.15	100.25	100.09	90.68
7025	109.82	111.95	112.85	110.34	111.85	97.27	82.66	87.83	93.95	102.06

The conductivities of the permeate using the conductivity meter described in section 4.7.5 along with the calculated salt rejection percentage using Eq. (12) and the duration of each run for feed flowrate of 1.5 L/min and temperatures of 70 °C, 60 °C, and 50 °C are presented in Table 18, Table 19, and Table 20, respectively.

The permeate electrical conductivity increased, which is possibly due to partial wetting as explained in section 3.4.1. Where the seawater leaks through the distillate side in the open membrane’s portions which will cause the contamination of the distillate and the production of low water quality, while the other

portions will have only reduced vaporous space which will lead to reduction in flux. After 23 hours, the salt rejection percentage started to decline more rapidly as shown in Table 18 to reach a value of 85.65 % at the end of the batch runs at a total of 49.5 hours of operation. Thus, before reaching 23 hours of operational hours it is expected that only large pores and the pores near the surface primarily experienced wettability. Whereas, the vaporous phase inside the membrane pores was still retained.

Table 18: The salt rejection percentages for all the runs of experiment code 7015.

Sample #	Run duration (min)	Distilled conductivity (mS/cm)	Salt rejection (%)
1	303.0	0.0459	99.95
2	244.0	0.138	99.85
3	309.5	0.0569	99.94
4	270.0	0.2163	99.77
5	232.5	0.5732	99.40
6	274.5	1.663	98.25
7	277.5	2.991	96.86
8	279.0	7.077	92.56
9	260.0	9.997	89.49
10	280.5	8.906	90.64
11	240.0	13.650	85.65

Table 19 shows that the salt rejection percentage started to decline after period of 47 hours of effective operation. Comparing these results with that of the higher running temperature it can be seen that the reduction in the percentage salt rejection took a longer period of time and was less dramatic than that of the higher temperature (70 °C) to reach a value of 93.33% at the end of the runs after 64 hours of effective operation.

Table 19: The salt rejection percentages for all the runs of experiment code 6015.

Sample #	Run duration (min)	Distilled conductivity (mS/cm)	Salt rejection (%)
1	311	40.56	99.57
2	289.5	4.4	99.95
3	292.5	3.9	99.96
4	290.5	7.83	99.92
5	233.5	20.23	99.79
6	208.5	8.26	99.91
7	280.5	9.48	99.90
8	264	25.93	99.73
9	372.5	40.7	99.57
10	279.5	53.66	99.44
11	378.5	225.5	97.63
12	285.5	455.7	95.21
13	344	634.6	93.33

Table 20: The salt rejection percentages for all runs of experiment code 5015.

Sample #	Run duration (min)	Distilled conductivity (mS/cm)	Salt rejection (%)
1	309.5	0.025	99.97
2	277.0	0.047	99.95
3	294.5	0.076	99.92
4	279.0	0.035	99.96
5	292.0	0.038	99.96
6	298.5	0.064	99.93
7	288.5	0.029	99.97
8	291.5	0.038	99.96
9	283.5	0.047	99.95
10	274.0	0.076	99.92
11	259.0	0.075	99.92
12	256.0	0.091	99.90
13	292.0	0.047	99.95
14	292.0	0.055	99.94
15	265.5	0.045	99.95
16	336.5	0.099	99.90
17	277.5	0.106	99.89
18	292.0	0.064	99.93
19	309.0	0.047	99.95

The percentage of salt rejection shown in Table 20, was not effected and is high (99.95%) after 91 hours of operation, deduce that no open portions of the membrane took place at the operating feed temperature of 50 °C and flowrate of 1.5 L/min, implying no sign of partial wetting, since the quality of water did not deteriorate and the distillate was not contaminated by the seawater feed. However, surface wetting may have occurred which was investigated by means of contact angle measurements.

The detailed tables of salt rejection percentage at feed flowrate of 2.5 L/min are added to (Appendix B: Salt rejection tables) and are not shown in this section, since all the values are very high (99%) for all runs as depicted in Figure 44 for all feed temperatures.

Figure 44 shows that the effect of increasing the feed temperature was more pronounced in the reduction of salt rejection at the lower feed flowrate (1.5 L/min). At feed temperature of 70 °C and feed flowrate of 1.5 L/min the constituents of seawater were more constantly in contact with the surface of the membrane with less shear action which allows the salt crystals to adhere to the surface and even to grow bigger increasing the opportunity of the scale to penetrate into the interior of the pores leading to partial wetting of the membrane. Moreover, at feed flowrate of 1.5 L/min the lowest salt rejection percentages of 85.65% and 93.33% were obtained at feed temperatures of 70 °C and 60 °C, respectively when compared with the higher feed flowrate. As confirmed by the SEM-EDS analysis shown in Figure 47, Figure 48 in section 5.3.1 at these two operational conditions CaSO_4 scale was detected on the surface of the membrane increasing the potential of partial membrane wetting, since once it is formed it adheres strongly to the surface and may lead to membrane damage [56].

However, high salt rejection percentages were obtained for all the feed temperatures, operating at the higher feed flowrate of 2.5 L/min. Which indicates a very lower potential for partial wettability, since the distillate was not contaminated by the feed seawater. Varying the feed flowrate did not influence the salt rejection percentage, at the relatively low temperature of 50 °C.

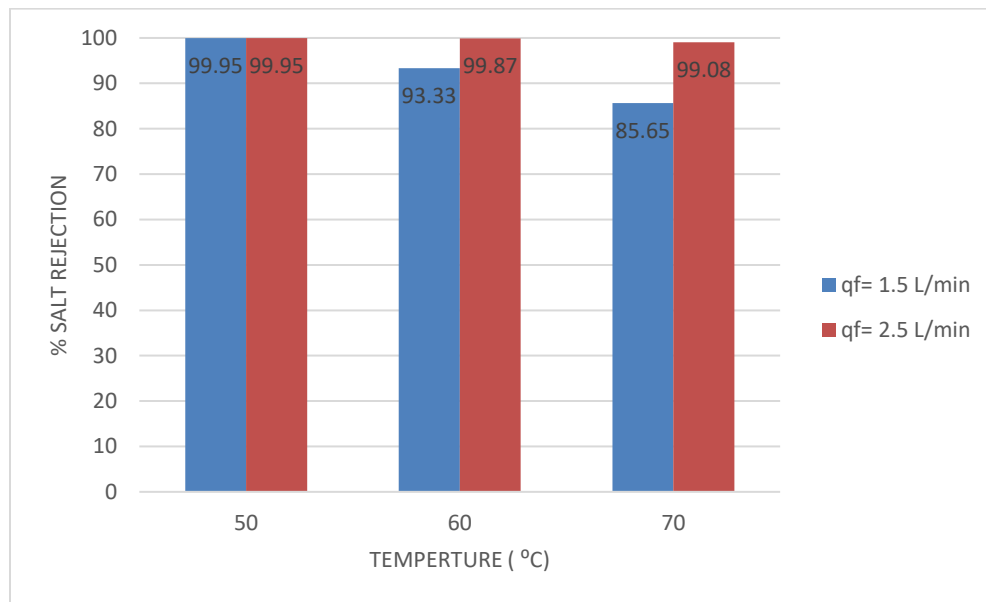


Figure 44: The salt rejection percentages for feed temperatures (50- 70 °C), at feed flowrates of (1.5, 2.5 L/min).

5.3 SEM-EDS physical characterization and analysis

In this section, some of the SEM images at different magnifications along with the EDS analysis will be presented for the used membranes. This technique of membrane autopsy can provide a qualitative description of how scaling and fouling affected the membrane surface. Consequently, flux decline profiles obtained at different operating conditions discussed in section 5.1 can be further understood.

The SEM image of the unfouled pristine membrane is shown in Figure 45, as can be seen the pores are more circular in shape. Fouling of the membrane by salt deposition was investigated after several extended runs at the specified operational condition. SEM imaging of the top surface of each used membrane was performed and the majority of the deposited elements were identified by the EDS analysis.

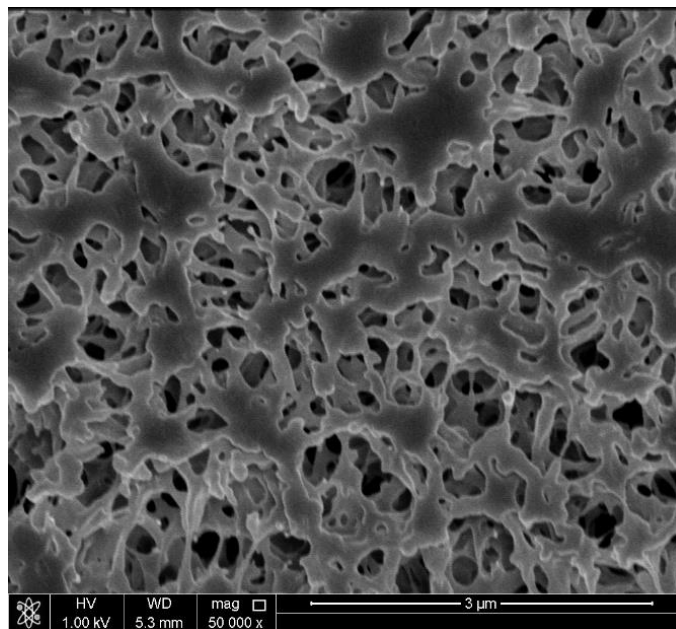


Figure 45: The representative SEM image of a pristine polypropylene membrane (0.2 μm) at x50000 magnification.

Several SEM images were performed from different locations of the membrane (at the inlet, outlet, and center) as described in section 4.8.4, in which only representatively selected images are revealed in order to understand the extent of the fouling and concentration polarization phenomenon on the MD performance.

5.3.1 SEM- EDS analysis for the used membranes at the lower flowrate

Figure 46 shows the fouling layer formed on the surface of the membrane after 4 weeks of seawater exposure in 50 hours of operation, compared with the as-received polypropylene membrane (Figure 45) that can be characterized by the sponge like structure with circular shaped pores. From Figure 46(a), the morphology “mountain-like” structure and the relatively large size of the crystals present, give a hint of severe fouling of the surface with almost all the parts covered with thick salt deposition layer. Same as for other locations on the membrane’s surface, presented in (Appendix C: SEM images of the used membrane for experiment code 7015). Figure 46(b) shows the morphology and the chemical structure of the crystals corresponding to a specific section of the membrane’s surface, similar crystals morphologies were seen in other parts of the SEM images. The arrow indicates the embedded NaCl in the deposit layer of the “needle-like” structure that may be a sign of the presence of calcium sulfate and calcium carbonate in the form of aragonite [8, 106].

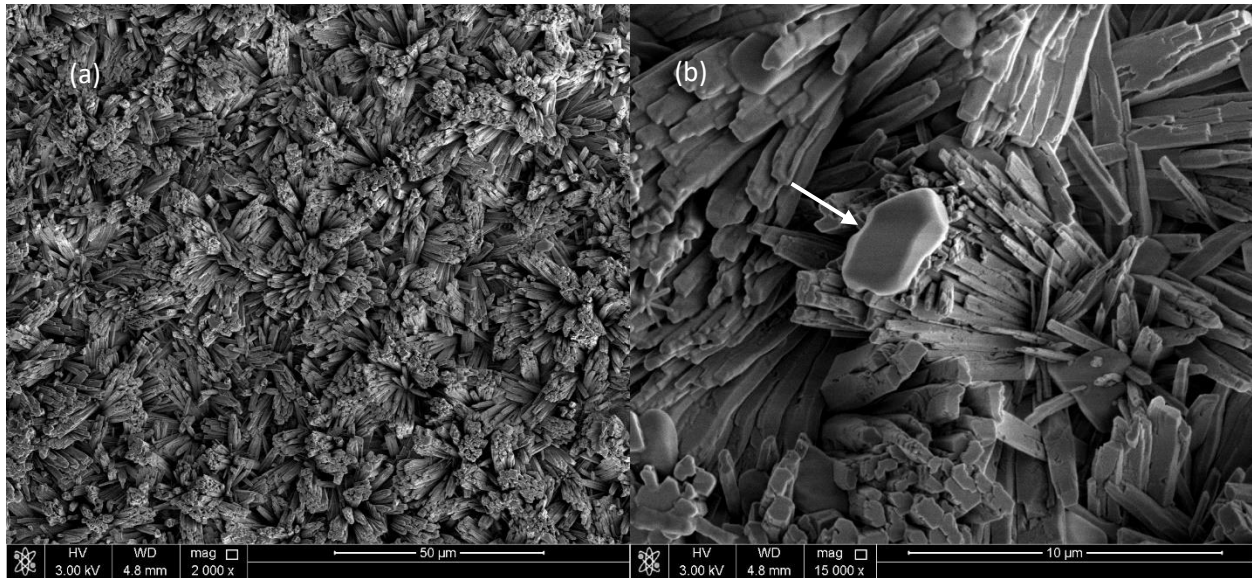


Figure 46: SEM images of the fouled membrane (a) The salt deposit layer magnification and (b) at x 15000 magnification, where $t_f = 70\text{ }^\circ\text{C}$ and $q_f = 1.5\text{ L/min}$ (experiment code: 7015).

The EDS microanalysis presents the elemental compositions of the salt deposits that confirms the identity of the crystals recognized from the electron microscopy. Figure 47 shows the EDS of the SEM images presented in Figure 46, the main elements the deposit composed of are Ca, O, and C and traces of S, Na, and Cl. The presence of these elements confirms that the crystals' chemical compositions consist of CaCO_3 , CaSO_4 , and NaCl that depict the components of the salt deposition layer. Moreover, at feed temperature of $70\text{ }^\circ\text{C}$ and feed flowrate of 1.5 L/min , CaCO_3 can be considered as the main contributor to fouling along with CaSO_4 .

The presences of these salts is consistent with the feed seawater composition Mg^{2+} , Ca^{2+} , HCO_3^{1-} , SiO_3^{2-} , and HSO_4^- confirmed by the ICP-OES test and is comparable with the seawater composition of Arabian Gulf found in literature [107]. Yet, under this specific running condition precipitates containing magnesium were not identified by the SEM-EDS analysis on the surface of the membrane, nor particulate and colloidal fouling.

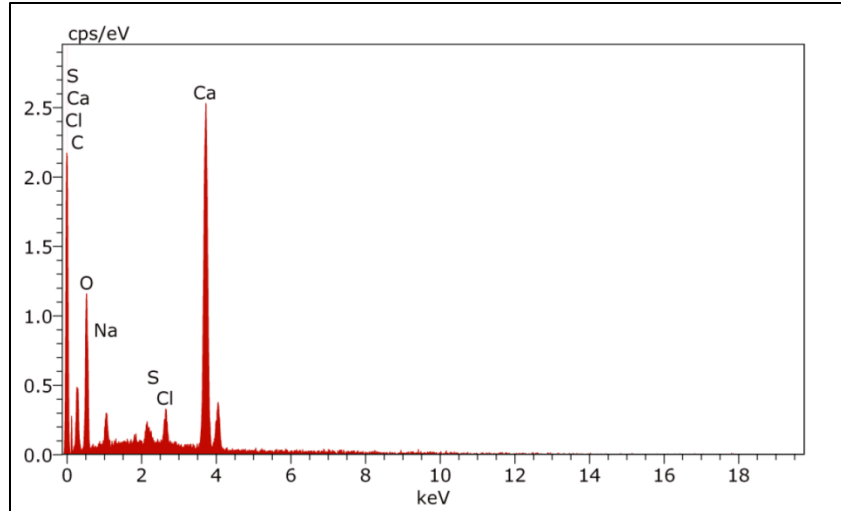


Figure 47: The EDS spectrum of the identified distinct crystal morphology shown in Figure 46.

Figure 48 shows the SEM-EDS analysis of different locations depicted as (a), (b) and (c) of the fouled membrane after 64 hours of batch runs. Moreover, Figure 48 depicts the different types of foulants at different locations of the membrane, which implies an inhomogeneous distribution of the salt crystals forming the deposit layer as proven by the SEM and EDS of various sites on the surface of the fouled membrane. The SEM image in Figure 48(a) identifies the existence of CaCO_3 in the form of aragonite [8, 106] and NaCl only, which is consistent with the elemental composition shown in the corresponding EDS spectrum (C, Ca, O, Na, and Cl). While, Figure 48(b) EDS analysis indicates that the deposit layer is composed of Ca, O, C and traces of Si, Fe, S, and Mg confirming the presence of CaCO_3 , CaSO_4 , MgCO_3 , and/or MgSiO_3 compounds in the layer covering the membrane surface as shown in the corresponding SEM image.

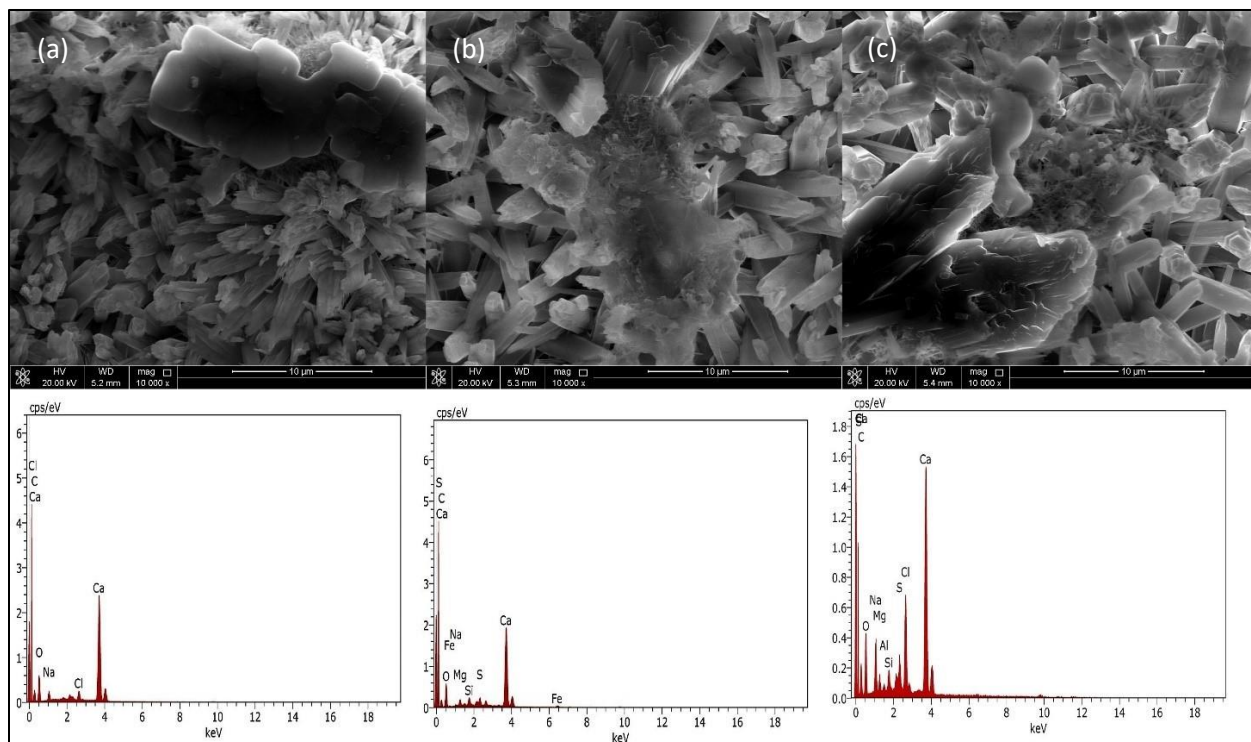


Figure 48: SEM images of the fouled membrane surface sites (a), (b), and (c) at x 10000 magnification and their corresponding EDS, where $t_f = 60\text{ }^\circ\text{C}$, $t_p = 20\text{ }^\circ\text{C}$ and $q_f = 1.5\text{ L/min}$ (experiment code: 6015).

Where the presence of Si and Fe can be classified as another form of fouling known as particulate and colloidal fouling. Silica particulate foulant is unlike other types of foulants it does not form a coat on the surface of the membrane nor it penetrate into the pores, but it causes clogging in the feed flow if hollow fiber membrane was used [86]. However, the seawater used as the feed was not pretreated; trivial amount of silica was seen in the EDS analysis and since the solubility of silica increases with temperature it was not present at the higher running temperature ($70\text{ }^\circ\text{C}$). Moreover, iron itself is not present in the feed seawater, it appears at the surface of the membrane as a result of a corrosion reaction in any form of iron oxide. This corrosion could be the result of a reaction between the seawater and the metallic surfaces in the flow loop. Moreover, iron oxides have tendency to accrue on the membrane surface and may penetrate into membrane pores. The crystalline structure of iron oxide existing depends on many

factors, such as: pH, temperature, and other ions present in the feed solution [62]. However, only trace amount of Fe was present as indicated by the EDS spectrum, due to the proper system design and the use of stainless steel which is more resistant to iron rusting.

Whereas, the salt deposit on the surface of the membrane shown in the SEM image corresponding to Figure 48(c) (different location) illustrate the presence of CaCO_3 , CaSO_4 , NaCl , MgSiO_3 and MgCO_3 as confirmed by the elemental composition displayed by the EDS analysis of that segment in addition to traces of aluminum that was not seen in other parts of the fouled membrane. Moreover, the SEM image at low magnification seen in Figure 49 gives an insight of the thickness and the coverage of the fouling layer at the surface, with compact large crystalline structures of the salt deposits due to the low feed flowrate [71].

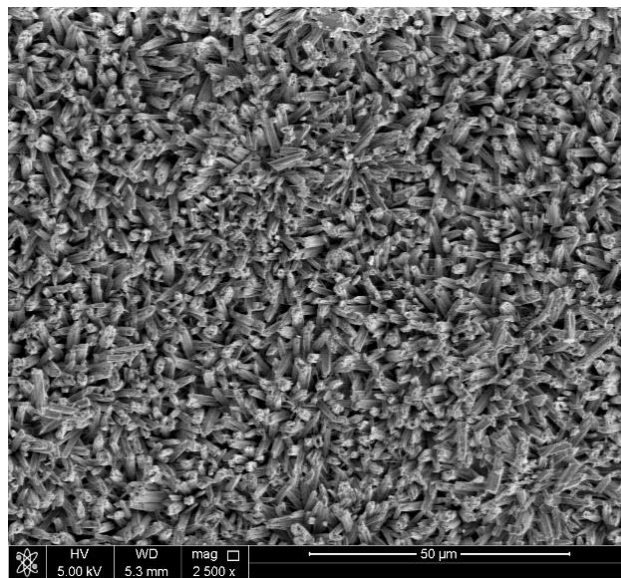


Figure 49: SEM image at x 2500 magnification of the surface of the fouled membrane, where $t_f= 60\text{ }^\circ\text{C}$, $t_p=20\text{ }^\circ\text{C}$ and $q_f=1.5\text{ L/min}$ (experiment code: 6015).

Figure 50 shows the SEM images corresponding to different parts of the used membrane as a result of 91 hours of operation at the feed temperature of 50 °C and feed flowrate of 1.5 L/min. The composition of the deposit shown in EDS spectrum Figure 50(a) consist of mainly Ca, O, C and traces of Na, thus the major component of the deposit corresponding to this segment is CaCO₃ in the form of vaterite (spherical shape, with diameter range of 0.05- 5 μm) [8, 106]. Moreover, the fouling layer cracks shown in Figure 50(a-b) and other SEM images (Appendix D: SEM images of the used membrane for experiment code 5015) indicate a thin and porous layer of fouling allowing the vapor to pass through the membrane surface. The stability of the permeate flux at feed temperature of 50 °C, can be deduced from the morphology of the fouling layer since it was proven by the SEM images to be less compact and more porous, with uncovered parts of the membrane surface as depicted in Figure 51. From the EDS spectrum of part (b) the major elements identified are C, O, N, Ca and small amounts of Mg, Si, and P. The obtained results confirm that CaCO₃, MgCO₃ and MgSiO₃ comprise the major components of this deposit layer.

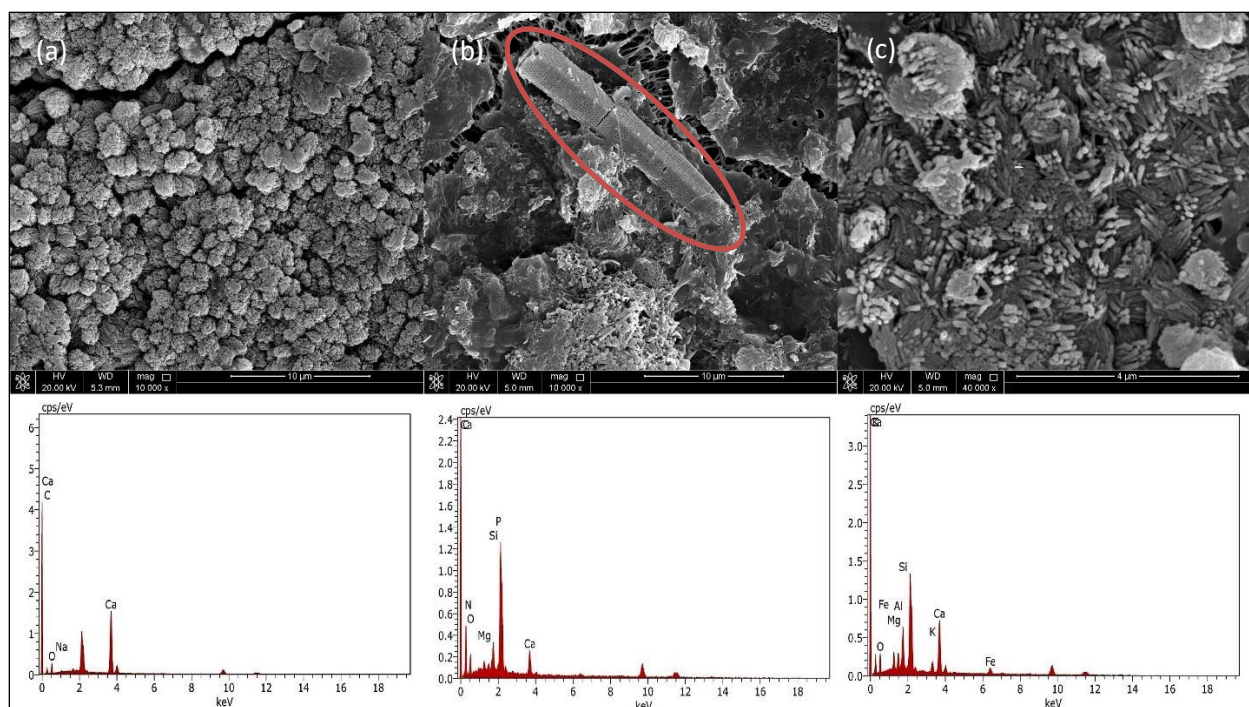


Figure 50: SEM-EDS analysis (a), (b), and (c) showing different parts of deposit formed on the surface of the fouled membrane at different high magnifications, where $t_f=50\text{ }^\circ\text{C}$ and $q_f=1.5\text{ L/min}$ (experiment code: 5015).

Due to the relatively low operating temperature, debris of dead plankton cells were observed on the surface of the fouled membrane as seen in Figure 50(b) indicated by a circle. Though, it may not be considered as biofouling or biofilm formation, since the SEM images show mainly mineral deposit with fragments of dead plankton. Therefore, in this work biofouling is not considered a major contribution to membrane fouling. Also, the inhomogeneity in deposit distribution of the fouled layer is confirmed by the SEM-EDS analysis. As shown in the EDS microanalysis Figure 50(c) the main elements constituting the deposit layer are C, O, and Ca and small amounts of Si, Mg, Fe, Al, and K confirming the presence of CaCO_3 , MgCO_3 , and MgSiO_3 . In additions to traces of Fe, Al and K that were not present in other parts on the membrane's surface. Furthermore, as can be noticed calcium sulfate scale was not observed under this specific operation conditions (low temperature).

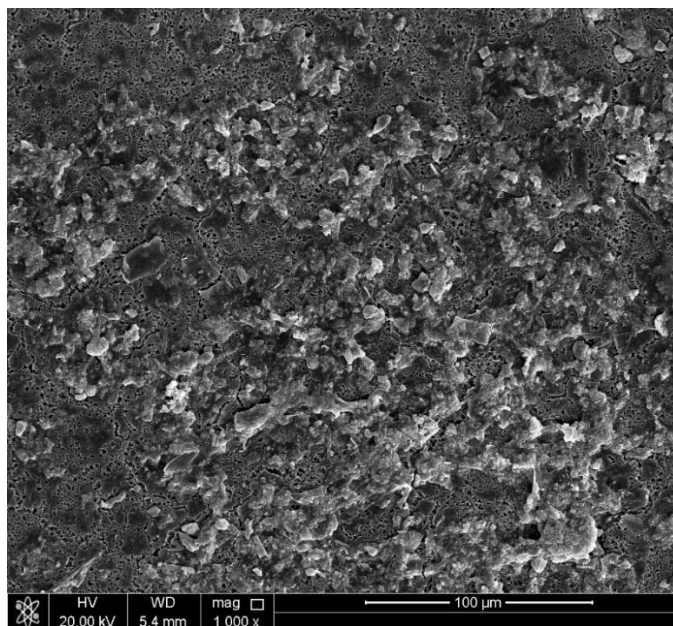


Figure 51: The SEM image at low magnification $\times 1000$ for experiment code: 5015.

It can be concluded that under different running temperatures different morphologies of the formed calcium carbonate crystal structure were determined. For example, Figure 46(a) indicates the presence of aragonite “needle-like structure” while Figure 50(a) indicates the presence vaterite identified by its spherical shape structure with diameter range of 0.05-5 μm . and the chemical composition and salts deposition and nucleation depends on the combination of operation conditions applied on the MD process.

5.3.2 SEM-EDS analysis at the higher feed flowrate

Figure 52 shows a representative section of the fouled surface of the membrane after 54 hours of operation at feed temperature of 70 $^{\circ}\text{C}$ and feed flowrate of 2.5 L/min. It was determined by the EDS spectrum that the major elements composing the deposit layer are Ca, C, O and small amounts of Mg, Si, Al and Fe. The obtained results confirm that CaCO_3 in the form of aragonite comprise the major component of the fouling layer on the surface on the membrane in addition to MgCO_3 and MgSiO_3 .

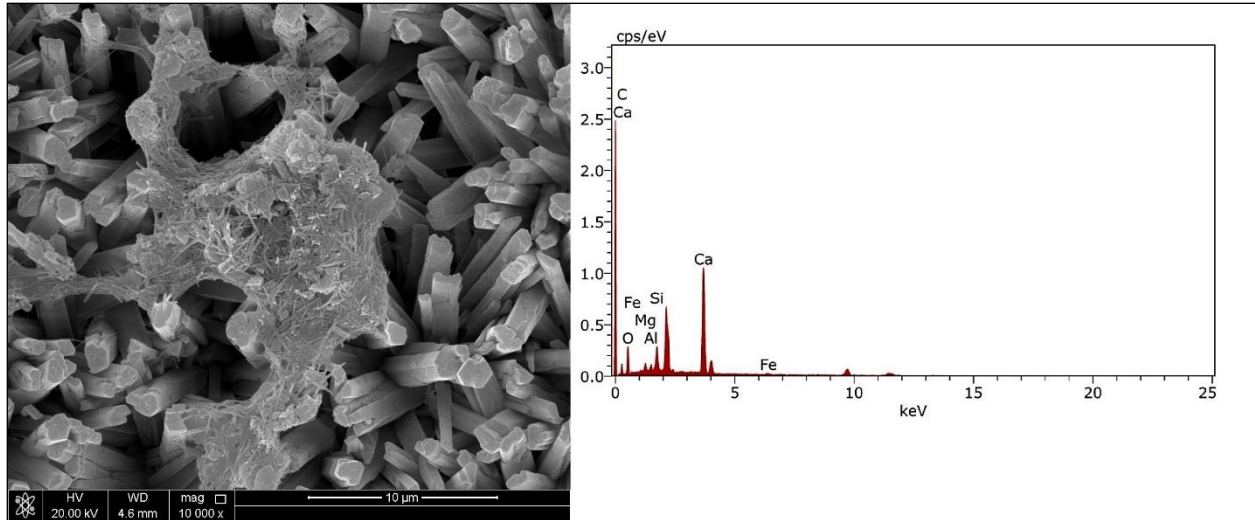


Figure 52: Sample of the SEM-EDS analysis of the fouled membrane surface, where $t_f = 70\text{ }^\circ\text{C}$ and $q_f = 2.5\text{ L/min}$ (experiment code: 7025).

In other section of the analyzed membrane surface different morphologies were obtained as confirmed by the SEM images despite the similar chemical compositions of species on the surface. Moreover, in some portions of the surface were not covered with deposits indicating a better permeability of the membrane at the higher feed flowrate, due to the increased surface shear action of water, reducing scaling potential. As well as, the size of the crystals formed is smaller compared with the lower feed flowrate, as explained in the kinetics of fouling process [9], and as found by Gryta [71].

CaSO_4 was not observed under high feed flowrate conditions, since CaSO_4 needs long induction period to precipitate and when it forms it adheres strongly to the surface, thus under stronger shear actions it will not have the same opportunity to form and adhere to the surface of the membrane.

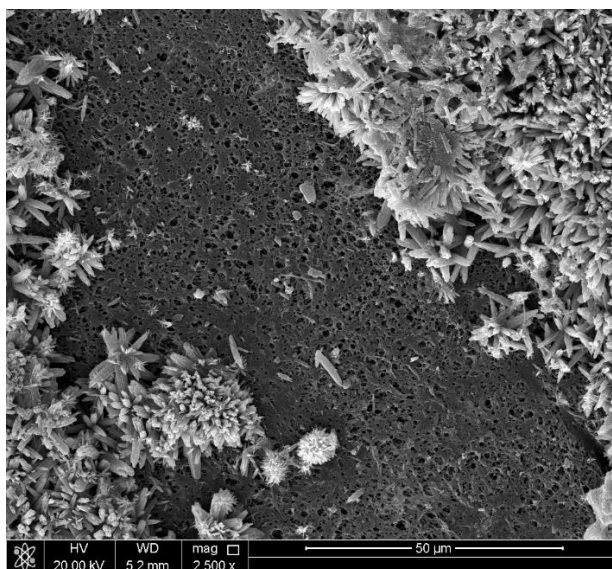


Figure 53: SEM image at 2500 x magnification showing the distribution of the deposit layer on the surface of the fouled membrane (experiment code: 7025).

Figure 54 was selected representatively to show the determined elements present on the surface of the membrane: Ca, C, and O and small amounts of Na, Cl, Al, Si, Mg, and Fe confirming the presence of CaCO_3 , NaCl, MgCO_3 , MgSiO_3 , and other particulates in the corresponding SEM image. Uneven distribution of the foulants composing the deposit layer analyzed in different sections of the membrane's surface, as confirmed by EDS (Appendix E: EDS for experimental code 6025). However, CaCO_3 in the form of aragonite crystalline structure "needle-like" [8, 106] can be considered to be the major component of the fouling layer deposited on the surface of the membrane.

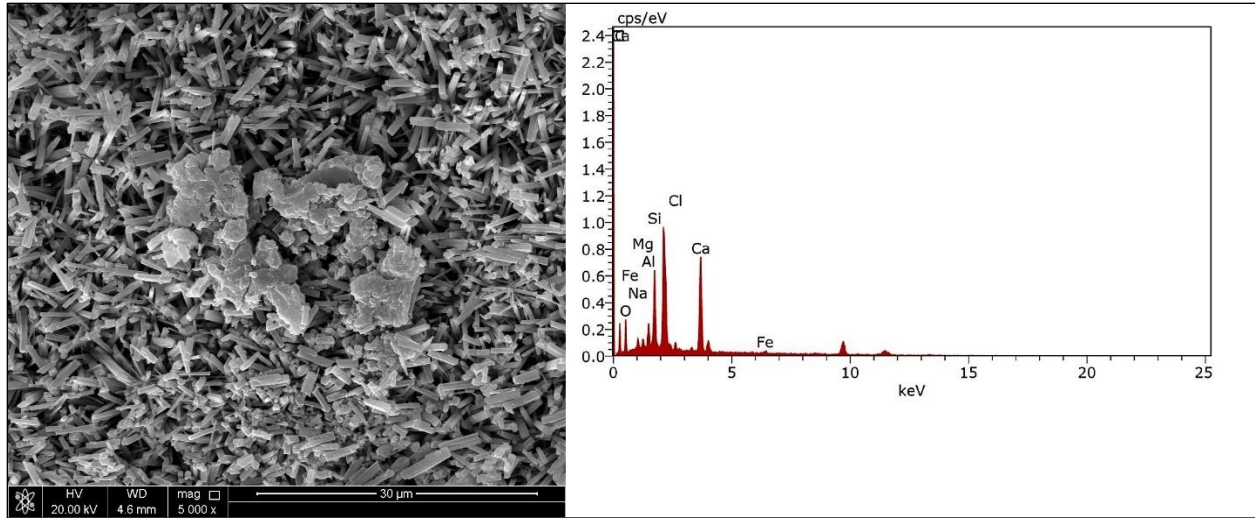


Figure 54: The result of the SEM-EDS analysis of the fouled membrane, where $t_f = 60\text{ }^\circ\text{C}$, and $q_f = 2.5\text{ L/min}$ (experiment code: 6025).

Furthermore, under the running conditions of $60\text{ }^\circ\text{C}$ and feed flowrate of 2.5 L/min a relatively thick deposit layer was formed indicating severe fouling. However, the fouling layer formed on the surface of the membrane was porous as indicated by the SEM image at low magnification in Figure 55. The crystals formed are relatively small when compared to the lower flowrate at the same feed temperature, depicted in Figure 49.

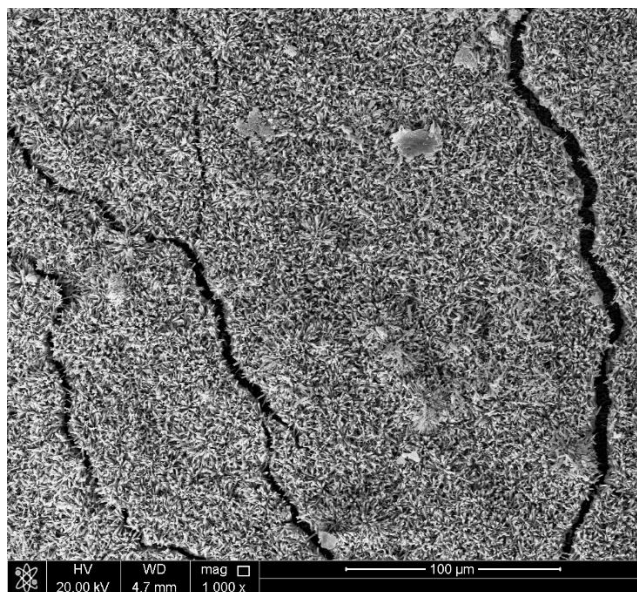


Figure 55: The SEM image at 1000 x magnification of the fouling layer formed on the surface of the membrane, at $t_f= 60$ °C and $q_f= 2.5$ L/min. (experiment code: 6025)

Figure 56 represent a sample of the SEM-EDS analysis performed at the fouled membrane after 71 hours of operation. The EDS analysis confirms that the major elements are Ca, C, O and small amounts of Mg, Si, Al, and Fe. Thus, CaCO_3 can be considered the major foulant shown in the SEM image in Figure 56 and other constituents such as: MgCO_3 , MgSiO_3 and NaCl comprise the fouling layer on the surface of membrane. Occasionally, K and Zn elements were determined in one of the EDS spectrum, nevertheless with negligible amounts.

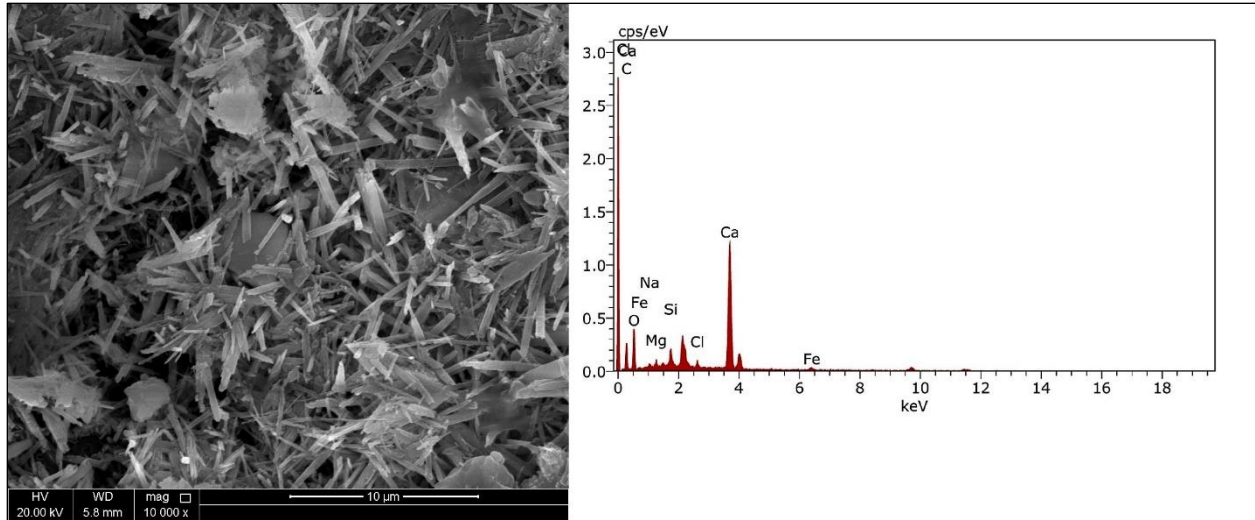


Figure 56: SEM-EDS analysis at 10000 x magnification of the fouled membrane surface, where $t_f = 50$ °C and $q_f = 2.5$ L/min (experiment code: 5025).

Different morphological structures were seen in different parts of the fouling layer. Moreover, the chemical compositions were different for different SEM images, suggesting an uneven distribution of the salt crystals. The deposit layer was fragile and less compact. Thus, less severe fouling indicated by the size of the crystals and the distance separating them on the membrane surface as perceived in Figure 57. This observation supports the explanation suggested by the CP effect that at a lower permeate flux lower potential of scale formation is expected, as depicted in Figure 38 a stable flux performance was obtained.

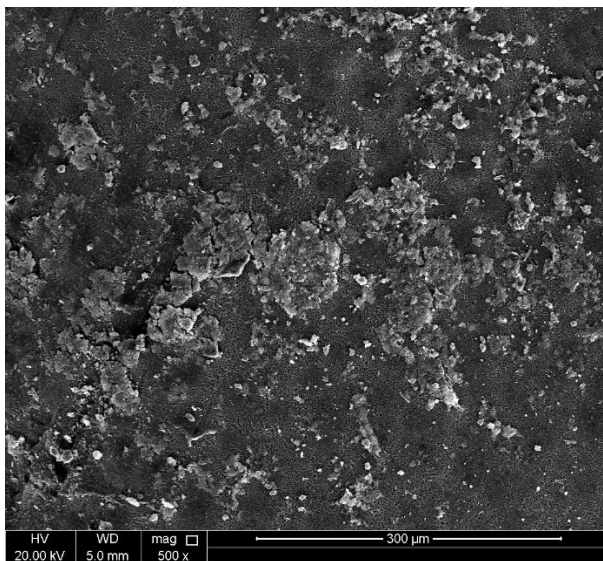


Figure 57: SEM image at a low magnification to give an indication on the distribution of the fouling layer on the surface of the membrane (experiment code: 5025).

5.4 The effect of antiscalant on the extended runs performance of MD

In this study, the use of a commercial antiscalant was investigated as a mitigation method to reduce and hinder fouling of the membrane, thus maintaining the flux and the quality of the distillate. The antiscalant PERFORMAX 3-S200 used was made of modified polycarboxlyte that is stable under high temperature operation and is non-toxic. More details about PERFORMAX 3-S200 antiscalant are presented in section 4.8.2. Three set of experiments were selected to perform the study with antiscalant. The operational conditions applied were listed in Table 13. The dosage of PERFORMAX 3-S200 antiscalant added for all the runs was 4 ppm, as recommended by the supplying company.

The addition of PERFORMAX 3-S200 antiscalant contributed to a significant reduction of permeate flux decline. Figure 58 shows that the permeate flux obtained is almost constant for an operation time of 52 hours. This can be explained by the ability of the antiscalant to inhibit the formation of the fouling layer by weakening the interactions between the salt crystals and their adherence to the flow surface of the membrane. This was explained in section 3.5.1. Thus, the thermal resistance due to presence of a fouling layer will be reduced, and so the heat transfer coefficient from the bulk of the feed to the surface of the membrane is less effected; hence the driving force for vapor transport will be enhanced.

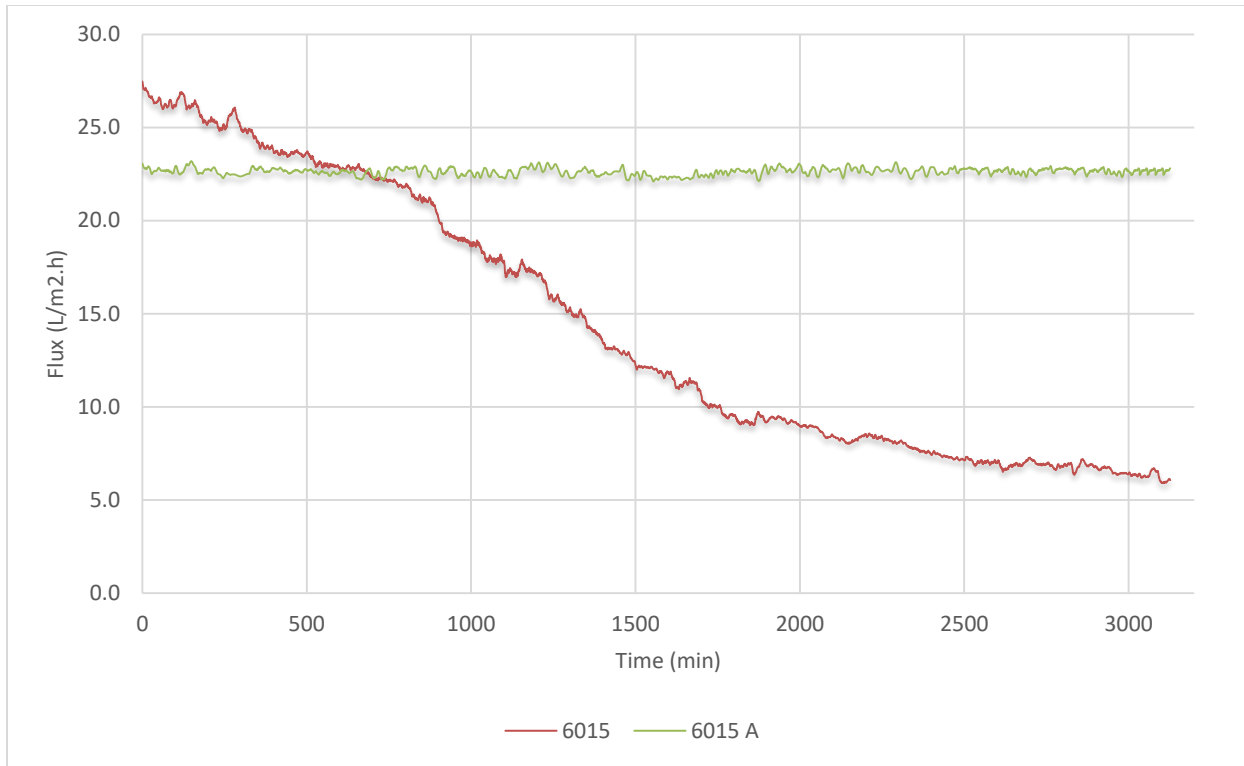


Figure 58: The permeate flux obtained at $t_f = 60\text{ }^\circ\text{C}$, $t_p = 20\text{ }^\circ\text{C}$ and $q_f = 1.5\text{ L/min}$, without (6015) and with added antiscalant (6015 A).

However, the initial flux produced is lower by a small amount under the effect of antiscalant added to the feed seawater as depicted from Figure 58. This could be due to some deviations caused by the constituents of the antiscalant on the seawater properties.

The results obtained in this work contrast with those obtained by Gryta [116] where the use of polyphosphate antiscalant additives caused larger decline in flux than without antiscalant in extended runs operation, thus reducing the efficiency of the MD process. This suggested that Gryta [116] used an unsuitable antiscalant for membrane distillation desalination.

Figure 59 shows that the addition of 4 ppm dosage of PERFORMAX 3-S200 antiscalant improved the flux performance drastically when compared to the experiment without antiscalant. This is due to the reduction in concentration polarization phenomena caused by the scale layer, enhancing mass transfer of

the vapor across the membrane by variety of mechanisms the antiscalant can work in, to control the growth of deposits and their adherence to the surface of the membrane. However, in the case of higher feed flowrate (2.5 L/min), a dip in the permeate flux was observed after 26 hours as depicted in Figure 59. Nevertheless, the flux remained constant thereafter until the end of the experiment (46 hours). It was not clear what may have caused this dip in flux.

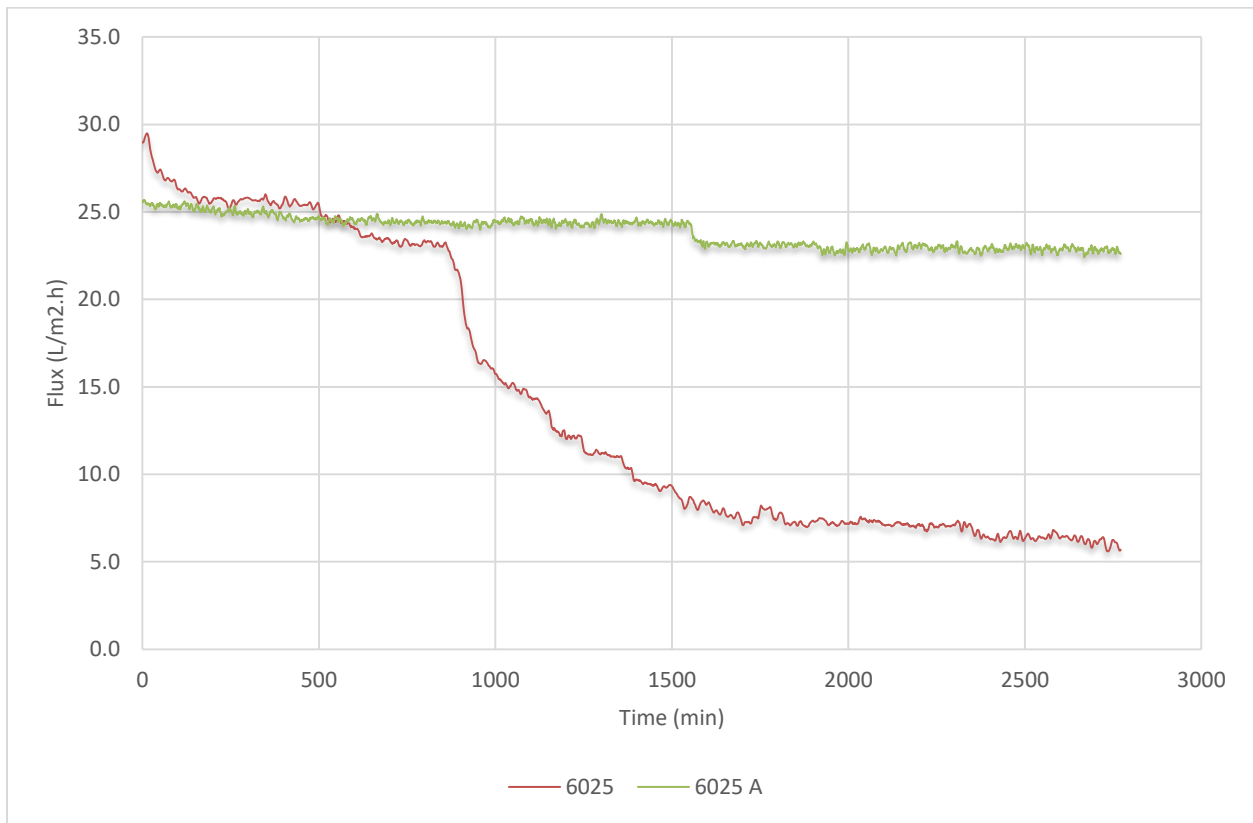


Figure 59: The permeate flux obtained at $t_f= 60\text{ }^\circ\text{C}$, $t_p= 20\text{ }^\circ\text{C}$ and $q_f= 2.5\text{L/min}$, without (6025) and with added antiscalant (6025A).

The results observed in Figure 60, confirms the effectiveness of the applied modified polycarboxlyte antiscalant, despite the higher applied feed temperature, since the permeate flux remained almost constant for 45 hours of operation.

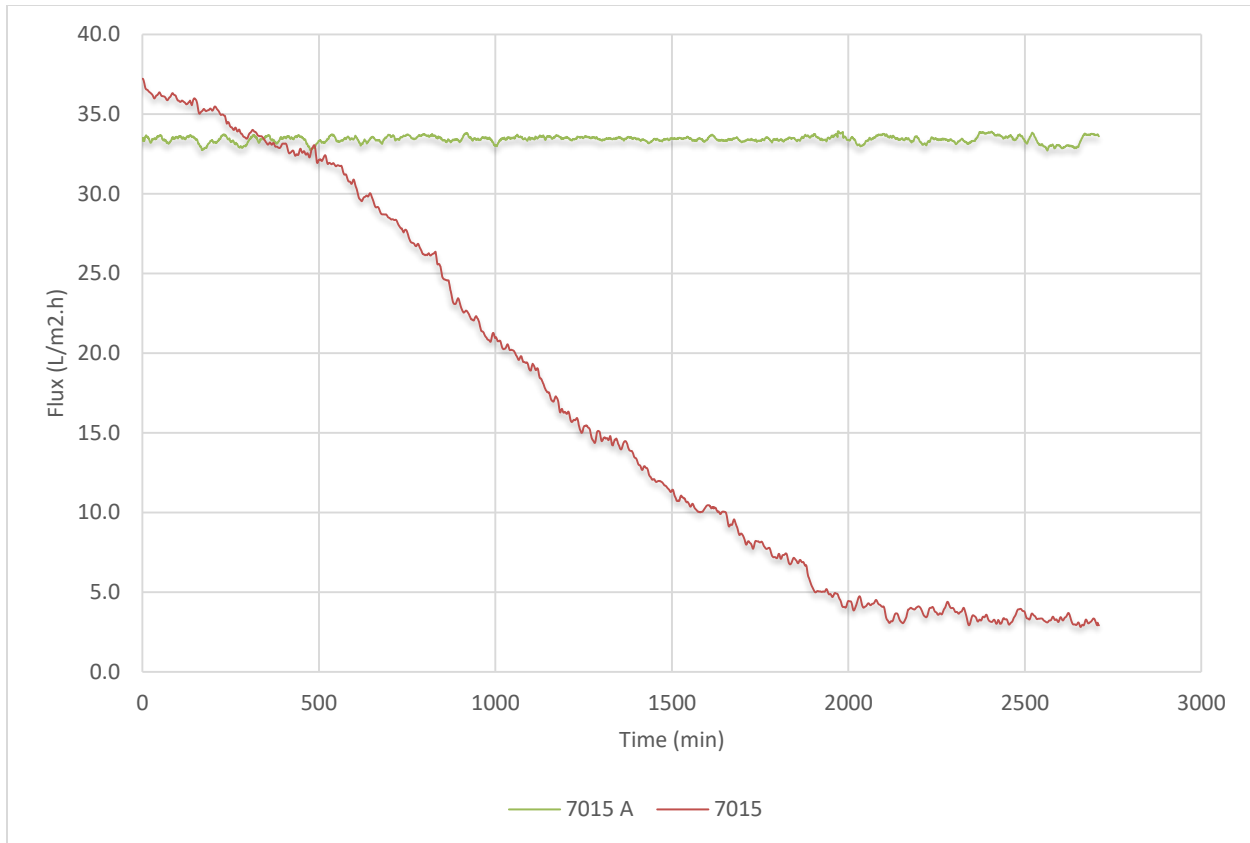


Figure 60: The permeate flux obtained at $t_f= 70\text{ }^\circ\text{C}$, $t_p= 20\text{ }^\circ\text{C}$ and $q_f= 1.5\text{L/min}$, without (7015) and with added antiscalant (7015 A).

The general observations perceived from Figure 60 are similar to those depicted by Figure 58 ($t_f= 60\text{ }^\circ\text{C}$, $q_f= 1.5\text{ L/min}$). Moreover, the addition of antiscalant at the same flowrate of 1.5 L/min caused a reduction in the initial permeate fluxes produced without adding antiscalant by 8% and 15% for feed temperatures of $70\text{ }^\circ\text{C}$ and $60\text{ }^\circ\text{C}$, respectively. Thus, increasing the operating temperature at the same feed flowrate leads to a higher production of permeate in MD desalination with added antiscalant. Unlike the results found by Gryta [116] in which the degree of hydrolysis of the polyphosphate antiscalant increased with an increase in feed temperature, and beyond 1 hour of MD instillation the antiscalant will be ineffective in inhabiting scale formation.

5.4.1 Investigation of membrane wetting occurrence with added antiscalant

In this section, the added antiscalant proves its effectiveness in terms of overall reduction in the damage caused by salt deposition and fouling with a minor reduction in surface contact angles regardless of the operating condition and since the salt rejection values were all higher than 99% indicating the production of highly pure distillate, not being contaminated by the feed constituents.

The pristine membrane contact angle was measured as 134.5 °. Details are presented in Table 15, in section 5.2. Moreover, the same procedures for measuring the contact angle were done on the used membranes from experiments with antiscalant, as described in section 4.8.3. The contact angles corresponding to the used membranes after applying antiscalant (does of 4 ppm) to the feed seawater, are shown in Table 21.

Table 21: The contact angle measurements of the used membrane under the effect of added antiscalant.

Experiment code	CA1	CA2	CA3	M1	M2	M3	OUT1	OUT2	OUT3	Average CA (°)
6015	104.9	109.65	111.09	106.58	111.31	113.12	108.87	110.74	110.84	109.68
7015	105.45	105.53	106.68	106.91	106.99	108.93	109.96	110.17	101.6	106.91
6025	110.93	113.45	118.23	102.91	109.74	102.49	118.1	104.44	101.9	109.13

Table 22 shows that all the contact angle measurements are very high compared to the pristine membrane and yet can be considered hydrophobic, regardless of the operational conditions applied. Moreover, the reduced hydrophobicity can be referred to a negligible surface wetting of the membrane due to the fact that the deposits covered the surface of the membrane partially. Uneven distribution of the crystals,

which was proven from the SEM images of the used membrane surfaces at low magnifications (a sample case is presented in Figure 63). And comparing the contact angle with and without the addition of antiscalant to the feed a general overall improvement can be concluded as shown in Table 22.

Table 22: The contact angle measurements of the used membranes, with and without the addition of antiscalant to the feed.

Experiment code	CA (°) without antiscalant	CA (°) with antiscalant
6015	102.41	109.68
7015	98.12	106.91
6025	90.68	109.13

High percentages of salt rejection were obtained with added antiscalant implying that no signs of partial wettability of the membrane caused by membranes full depth penetration by contaminants to the distillate side. Moreover, for 45- 52 hours of operation the antiscalant has worked effectively in mitigating membrane fouling with the production of high water quality, regardless of the operational condition applied in this study as illustrated in Figure 61. Yet, the highest reduction in the deterioration of water quality was in the instance of using feed temperature of 70 °C and feed flowrate of 1.5 L/min (7015). On the other hand, the addition of antiscalant did not cause a noticeable improvement in terms of salt rejection percentage at temperature of 60 °C and flowrate of 2.5 L/min (6025), because the application of higher feed flowrate prevented the contamination of the distillate by the feed seawater.

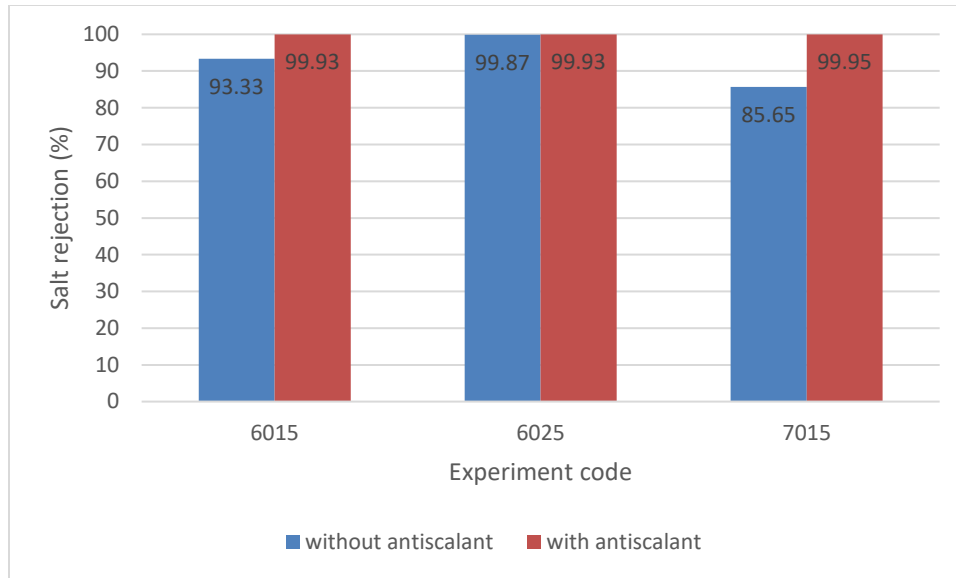


Figure 61: The salt rejection percentages with and without the addition of antiscalant to the feed.

SEM-EDS analysis of the used membranes with added antiscalant

The antiscalant inhibited the crystallization and nucleation of the salts to a large degree as depicted from Figure 62. Figure 62(b) shows a deformed deposit. This altered morphology of crystals is a result of the antiscalant working mechanism in disturbing crystal formation and weakening the adhesion of the crystals to the membrane surface, with the exact working mechanism left unestablished. However, insignificant amount was detected on the membrane surface. Moreover, negligible amount of scattered scale crystals has formed on the membrane surface as can be depicted from the SEM image obtained in Figure 62(a). Where the flux maintained stable and the MD process efficiency was enhanced, thus the antiscalant worked effectively in restricting the amounts of deposits formed on the surface of the membrane. Moreover, most of the membrane surface is free from deposit as shown in Figure 63. Notably, the SEM images presented were selected randomly since all the used membranes surfaces had similar morphologies and chemical composition, regardless of the operational conditions.

From the EDS analysis of the used membranes no traces of sulfur were found in the chemical composition of the scattered crystalline structures observed on the membranes surface, with Ca, C, and O being the main components suggesting that CaCO_3 was the dominant composition of the deposits.

On the other hand, highly amorphous morphologies with low porous scaling layer has been observed by Gryta [116] by adding antiscalant of polyphosphate to the feed solution (lake water with added bicarbonate) what caused the deterioration in the MD process efficiency.

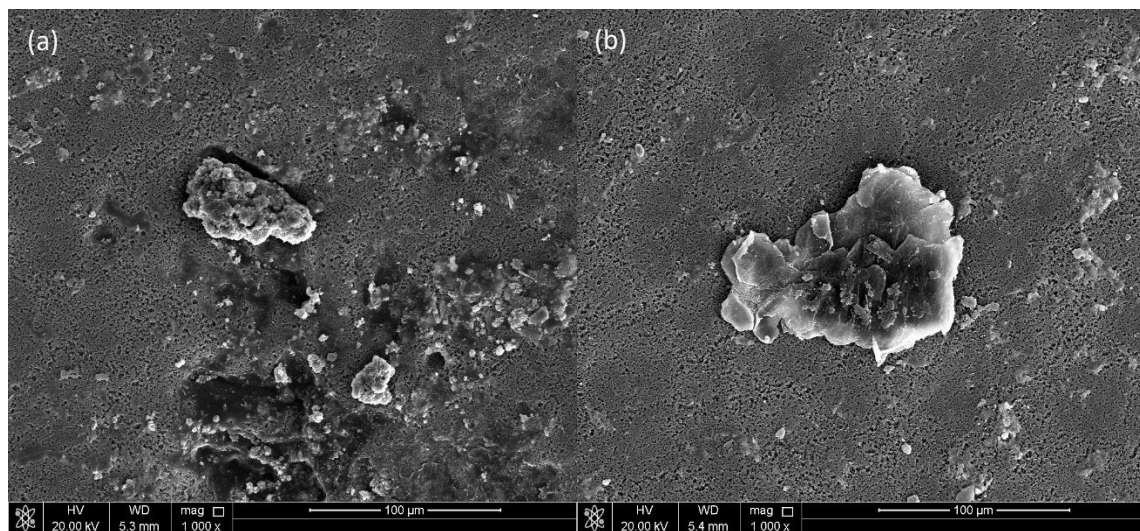


Figure 62: The SEM images of used membranes at x 2000 magnification with added antiscalant to the feed.

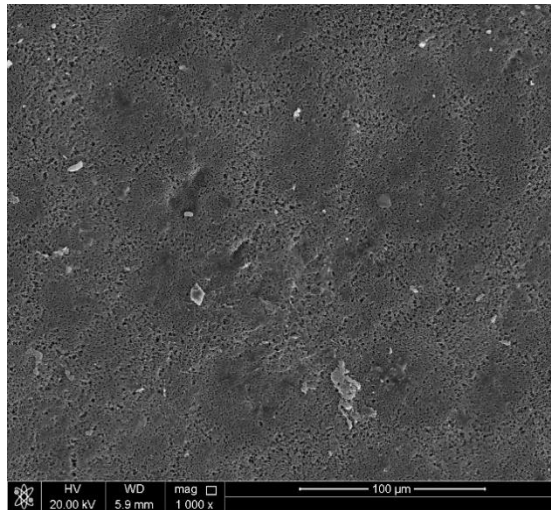


Figure 63: The SEM image at 1000x magnification of the used membrane after applying antiscalant to the feed.

A summary of the case studies with and without the addition of antiscalant presented in chapter 5 is conveniently presented in Table 23, Table 24, and Table 25.

Table 23 shows the case scenarios where both fouling and wetting of the membrane took place and the repeated cases with the addition of the antiscalant showed that the used polypropylene membranes (0.2 microns) and 73-75% porosity were partially clean with no signs of wettability. Table 24 shows more porous fouled surfaces with less compact and smaller size of crystals compared to those shown in Table 23 at the lower feed flowrate. Moreover, the high values of salt rejection percentage depict that membrane wetting did not occur, nevertheless surface loss of hydrophobicity of the membranes took place as indicated from the reduced contact angle measurements. Likewise, the addition of antiscalant (6025 A) was effective in mitigating membrane fouling to a significant degree. Table 25 shows the SEM images of the used membranes for cases 5015 and 5025 to be partially covered with scattered crystals and porous layer of fouling with negligible flux decline and the production of high water quality regardless of the low rate of production, due to the low operating feed temperature, likewise the higher flowrate shows small salt crystalline structures.

Table 23: The worst-case scenarios before and after the addition of antiscalant.

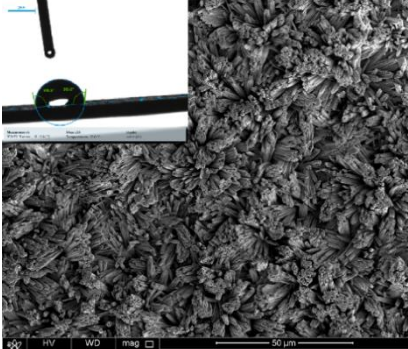
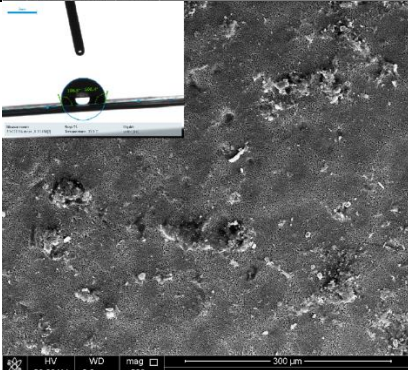
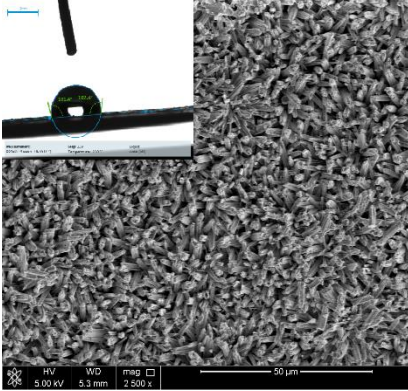
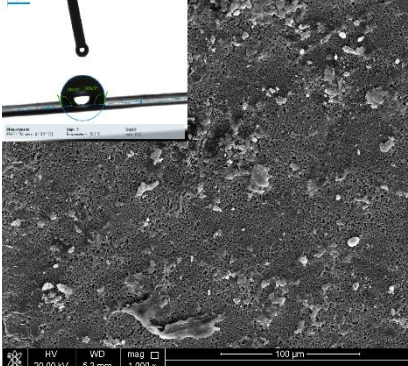
Experiment code	PP layer at low magnifications	Main constituents	Salt rejection (%)	Flux decline (%)
7015		carbonates and sulfates.	85.65	92.18
7015 A		Carbonates (negligible amounts)	99.95	insignificant
6015		Carbonates and sulfates	93.33	74.04
6015 A		Carbonates (negligible amount)	99.93	Insignificant

Table 24:Case scenarios with membrane fouling and after the addition of antiscalant.

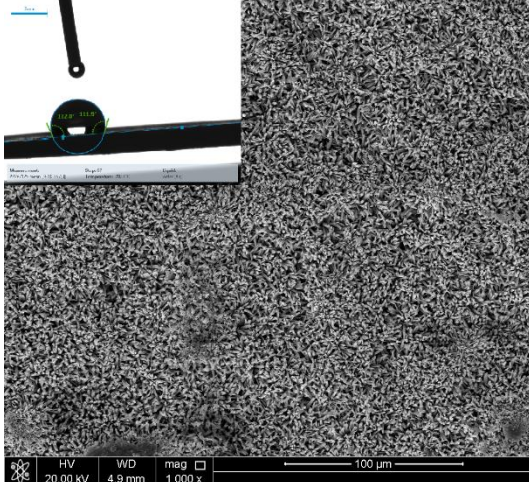
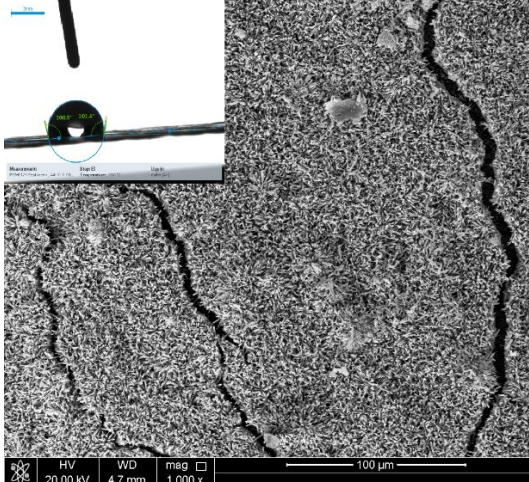

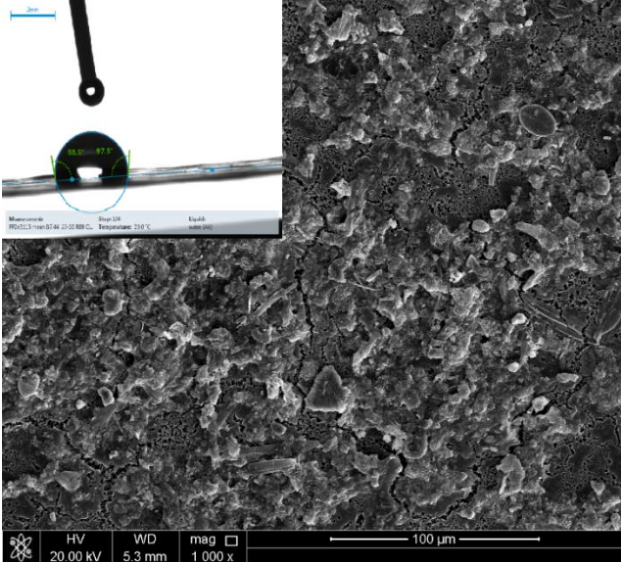
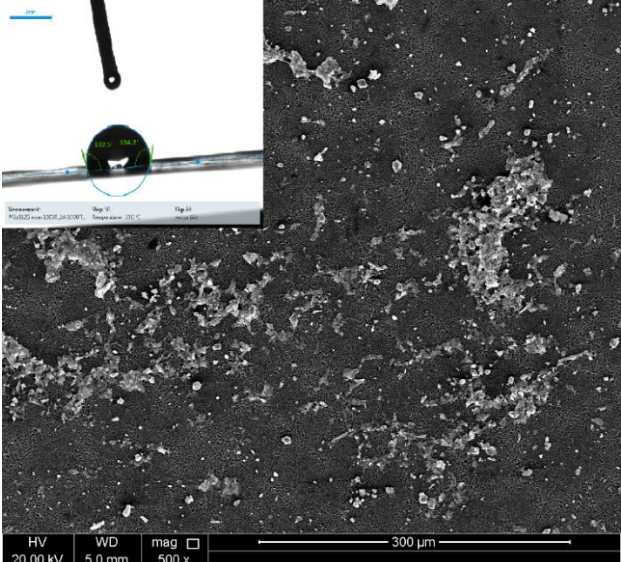
Experiment code	PP layer at low magnifications	Main constituents	Salt rejection (%)	Flux decline (%)
7025		Carbonates	99.08	92.60
6025		Carbonates	99.87	78.69
6025 A		Carbonates (negligible amounts)	99.93	9.6

Table 25: Case scenarios with minimal membrane fouling without the addition of antiscalant.

Experiment code	PP layer at low magnifications	Main constituents	Salt rejection (%)	Flux decline (%)
5015		Salts of carbonates	99.95	7.33
5025		Salts of carbonate	99.95	8.63

6 Conclusions and recommendations

6.1 Conclusions

The experiments performed in DCMD unit for desalination using polypropylene membranes, for the purpose of investigating membrane fouling behavior by studying the flux performance, SEM-EDS analysis and salt rejection percentages by means of distillate conductivity measurements. Moreover, membrane fouling problem significantly influence the effectiveness of the membrane and its life-cycle. The investigation of mitigation method by commercial antiscalant was a crucial factor for membrane distillation to effectively compete with other desalination systems. The objectives of this work were achieved, and the following conclusions were inferred.

In general, it can be concluded that at a given flowrate for extended runs using high salinity seawater as the feed in DCMD process using polypropylene membrane 0.2 microns and 73-75% porosity, beyond the operational temperature of 50 °C the percentage of flux decay increased drastically.

It can be concluded from studying the effect of varying the feed temperature at a constant flowrate on fouling behavior, that:

- Increasing the feed temperature led to a significant increase in the initial flux obtained, due to the exponential relation between the driving force of the MD process (partial vapor pressure) with temperature difference as suggested by Antoine equation.
- The higher the flux obtained, the higher the degree of concentration polarization (CP) observed in terms of flux decline. Thus, it can be inferred that the feed temperature as an operating parameter is the main factor influencing the potential of scale formation in terms of increasing the concentration polarization effect.

- At low feed temperature of 50 °C minimal scale formation occurred with low but stable flux performance, while at higher feed temperatures significant scale formation took place as inferred from the average fouling rates.

The following remarks can be inferred from studying the effect of varying the feed flowrate at constant feed temperature on the fouling behavior:

- The effect of feed flowrate can be divided into two categories: at low feed temperature and at high feed temperature. At the low feed temperature (50 °C) the effect of thermal resistance of the boundary layers was dominant (R1 and R4). Thus, a slightly higher flux was produced at the higher flowrate with minimal CP effects, due to the low fluxes produced.
- At higher feed temperatures, the effect of reduced TP becomes more significant promoting the formation of the fouling layer. However, the decline in flux at the higher flowrate was more significant due to the promotion of loss of heat by conduction and the initially higher flux causing an increase in CP effect and the thermal resistance of the fouling layer. However, TP will be increased as a result of heat loss by conduction, thus reducing scale formation that exhibits inverse solubility leading to a less compact fouling layer. Moreover, the higher the temperature the more pronounced the effect of feed flowrate on the permeate flux deterioration.

According to membrane wettability investigations, the following insights can be referred:

- In general, fouling of the membrane may potentially lead to membrane wetting. However, the impact of membrane wetting may not directly be related to the permeate flux performance (because wetting was not severe in the cases studied).
- The obtained salt rejection percentage was the lowest (85.6%) at the highest operating temperature (70 °C) and flowrate of 1.5 L/min, which indicates a sign of membrane partial wettability due to salt passage across the membrane.

- The higher operating flowrate lead to the production of high water quality (more than 99% salt rejection) at any studied temperature, probably by disturbing the growth of sulfate crystals associated with membrane wetting.
- The percentage of salt rejection at feed temperature of 50 °C was not affected regardless of the operating flowrate.
- All the used membranes showed partial loss of membrane hydrophobicity compared to the pristine membrane (134.5 °). Nevertheless, the surface contact angle measured for all the used membranes were above 90 °.

From the SEM-EDS analysis of the used membranes, the following conclusions can be deduced:

- Membrane fouling and salt crystallization lead to the formation of a deposit layer on the surface of the membrane and eventually permeate flux decline was observed in most of the cases studied. However, the composition of the fouling layer and its compactness depends on the operational conditions of the MD process.
- The feed flowrate has significantly influenced the morphology of the deposit layer. At the higher flowrate, smaller crystals were formed and the fouling layer was less compact when compared to layer of fouling observed at the lower flowrate.
- Carbonates were observed in all the cases studied, regardless of the amount deposited that depends on the operational conditions applied.
- At the lower flowrate (1.5 L/min) and higher temperatures of 60 °C and 70 °C both carbonates and sulfates were observed on the surface of the membrane.
- At the higher flowrate (2.5 L/min) calcium sulfates were not observed on the surface of the membrane at any temperature studied, but carbonates were observed. Since under stronger shear actions calcium sulfate will not have the same opportunity to adhere to membrane surface.

- Sodium chloride was observed on the membrane's surface in most cases studied, due to the long operational period of the extended runs and the use of spacer that may have caused the NaCl to be trapped near the membrane surface at small dead zones.
- Membrane wetting in terms of foulants full depth penetration into the permeate side, was detected when sulfates co-precipitated with carbonates.

The optimization of MD process in terms of adjusting the operational conditions was not practical, since the compromise between reduced membrane fouling and high permeate flux production was not feasible. This is due to the association of higher concentration polarization effect with the operational conditions that lead to the generation of higher flux. Thus, to insure high flux with optimum MD performance in extended runs operations, a mitigation method using a commercial antiscalant was proposed to the worst-case scenario conditions where the initial high flux was followed by decline due to membrane fouling.

From the application of commercial antiscalant to the feed seawater, the following can be stated:

- Antiscalant PERFORMAX 3-S200 at a dosage of 4 ppm has shown its effectiveness in mitigating membrane fouling, preventing wetting and improving the performance of the MD desalination.
- All the used membranes revealed high contact angle measurements, when compared to the pristine membrane. Moreover, the selectivity of the membranes was not affected since the salt rejection percentages were all higher than 99%.
- The antiscalant inhibited the growth of calcium sulfate completely and hindered the growth of carbonates to a significant degree.
- In the cases studied, the initial permeate flux was reduced slightly when applying antiscalant. However, no flux decline was observed.

6.2 Recommendations and future work

At the end of this study, some recommendations are proposed for future work:

- In long-term performances, the commercially available membranes are highly susceptible to fouling eventually leading to a reduced life time increasing the replacement costs if it is to be employed in real plants. Thus, it is vital to design special membranes for MD desalination with adjusted desirable properties to be applicable for large scale implementations.
- The kinetics of salt crystals nucleation and growth are not fully understood; thus, it should be further investigated in order to better comprehend the effect of fouling on the permeate flux performance.
- The employment of characterization methods that can determine membrane wetting in terms of revealing pore blockage by foulants, such as taking SEM images of the cross section of the used membranes. Moreover, estimating the thickness of the deposit layer by physical techniques such as, optical laser sensor to better understand the effect applied operational conditions on membrane fouling compactness and the process of MD.
- The increase in feed temperature led to the reduction in the induction periods of salt deposition. Moreover, increasing the flowrate will cause the induction period to be further reduced. However, it is difficult to predict the SI index of any salt in the presence of other salts. Therefore, efforts should be made in future work to develop advanced thermodynamic numerical models for mixed salts saturation indices.
- The temperature and concentration polarization effects were used to interpret the effect of fouling on the membrane and permeate flux performance. However, their effect should be correlated with advanced modeling of the MD desalination process which incorporates crystallization studies.

- The effect of varying the concentration of antiscalant added to the feed should be further investigated, to evaluate the cost of mitigation on the performance of MD if to be functional in large scale.
- Elucidation of the antiscalant working mechanism in preventing scale formation in MD desalination can further serve in optimizing the mitigation process.

References

1. Hsu, S.T., K.T. Cheng, and J.S. Chiou, *Seawater desalination by direct contact membrane distillation*. *Desalination*, 2002. **143**(3): p. 279-287.
2. El-Bourawi, M.S., et al., *A framework for better understanding membrane distillation separation process*. *Journal of Membrane Science*, 2006. **285**(1–2): p. 4-29.
3. Khayet, M., *Membranes and theoretical modeling of membrane distillation: A review*. *Advances in Colloid and Interface Science*, 2011. **164**(1–2): p. 56-88.
4. Tomaszewska, M., M. Gryta, and A.W. Morawski, *The influence of salt in solutions on hydrochloric acid recovery by membrane distillation*. *Separation and Purification Technology*, 1998. **14**(1–3): p. 183-188.
5. Alves, V.D. and I.M. Coelho, *Orange juice concentration by osmotic evaporation and membrane distillation: A comparative study*. *Journal of Food Engineering*, 2006. **74**(1): p. 125-133.
6. Banat, F.A. and J. Simandl, *Removal of benzene traces from contaminated water by vacuum membrane distillation*. *Chemical Engineering Science*, 1996. **51**(8): p. 1257-1265.
7. Chiam, C.-K. and R. Sarbatly, *Vacuum membrane distillation processes for aqueous solution treatment—A review*. *Chemical Engineering and Processing: Process Intensification*, 2013. **74**: p. 27-54.
8. Tijjng, L.D., et al., *Fouling and its control in membrane distillation—A review*. *Journal of Membrane Science*, 2015. **475**: p. 215-244.
9. Warsinger, D.M., et al., *Scaling and fouling in membrane distillation for desalination applications: A review*. *Desalination*, 2015. **356**: p. 294-313.
10. Lawson, K.W. and D.R. Lloyd, *Membrane distillation*. *Journal of Membrane Science*, 1997. **124**(1): p. 1-25.

11. Chew, J.W., W.B. Krantz, and A.G. Fane, *Effect of a macromolecular- or bio-fouling layer on membrane distillation*. Journal of Membrane Science, 2014. **456**: p. 66-76.
12. Gryta, M., *Fouling in direct contact membrane distillation process*. Journal of Membrane Science, 2008. **325**(1): p. 383-394.
13. Alkhudhiri, A., N. Darwish, and N. Hilal, *Membrane distillation: A comprehensive review*. Desalination, 2012. **287**: p. 2-18.
14. Tijing, L.D., et al., *A novel dual-layer bicomponent electrospun nanofibrous membrane for desalination by direct contact membrane distillation*. Chemical Engineering Journal, 2014. **256**: p. 155-159.
15. Tijing, L.D., et al., *Recent progress of membrane distillation using electrospun nanofibrous membrane*. Journal of Membrane Science, 2014. **453**: p. 435-462.
16. Cabassud, C. and D. Wirth, *Membrane distillation for water desalination: How to chose an appropriate membrane?* Desalination, 2003. **157**(1): p. 307-314.
17. Hassan, A.S. and H.E.S. Fath, *Review and assessment of the newly developed MD for desalination processes*. Desalination and Water Treatment, 2013. **51**(1-3): p. 574-585.
18. Tang, C.Y., T.H. Chong, and A.G. Fane, *Colloidal interactions and fouling of NF and RO membranes: A review*. Advances in Colloid and Interface Science, 2011. **164**(1-2): p. 126-143.
19. Al-Amoudi, A.S., *Factors affecting natural organic matter (NOM) and scaling fouling in NF membranes: A review*. Desalination, 2010. **259**(1-3): p. 1-10.
20. Mairal, A.P., et al., *Real-time measurement of inorganic fouling of RO desalination membranes using ultrasonic time-domain reflectometry*. Journal of Membrane Science, 1999. **159**(1-2): p. 185-196.
21. Antony, A., et al., *Scale formation and control in high pressure membrane water treatment systems: A review*. Journal of Membrane Science, 2011. **383**(1-2): p. 1-16.

22. Tzotzi, C., et al., *A study of CaCO₃ scale formation and inhibition in RO and NF membrane processes*. Journal of Membrane Science, 2007. **296**(1–2): p. 171-184.
23. Nghiem, L.D. and T. Cath, *A scaling mitigation approach during direct contact membrane distillation*. Separation and Purification Technology, 2011. **80**(2): p. 315-322.
24. Shirazi, S., C.-J. Lin, and D. Chen, *Inorganic fouling of pressure-driven membrane processes — A critical review*. Desalination, 2010. **250**(1): p. 236-248.
25. Susanto, H., *Towards practical implementations of membrane distillation*. Chemical Engineering and Processing: Process Intensification, 2011. **50**(2): p. 139-150.
26. Gunko, S., et al., *Concentration of apple juice using direct contact membrane distillation*. Desalination, 2006. **190**(1): p. 117-124.
27. Singh, D. and K.K. Sirkar, *Desalination of brine and produced water by direct contact membrane distillation at high temperatures and pressures*. Journal of Membrane Science, 2012. **389**: p. 380-388.
28. Tomaszewska, M., M. Gryta, and A.W. Morawski, *Study on the concentration of acids by membrane distillation*. Journal of Membrane Science, 1995. **102**: p. 113-122.
29. Banat, F.A. and J. Simandl, *Desalination by Membrane Distillation: A Parametric Study*. Separation Science and Technology, 1998. **33**(2): p. 201-226.
30. García-Payo, M.C., M.A. Izquierdo-Gil, and C. Fernández-Pineda, *Air gap membrane distillation of aqueous alcohol solutions*. Journal of Membrane Science, 2000. **169**(1): p. 61-80.
31. García-Payo, M.C., et al., *Separation of binary mixtures by thermostatic sweeping gas membrane distillation: II. Experimental results with aqueous formic acid solutions*. Journal of Membrane Science, 2002. **198**(2): p. 197-210.
32. Bandini, S. and G.C. Sarti, *Heat and mass transport resistances in vacuum membrane distillation per drop*. AIChE Journal, 1999. **45**(7): p. 1422-1433.

33. Lawson, K.W. and D.R. Lloyd, *Membrane distillation. I. Module design and performance evaluation using vacuum membrane distillation*. Journal of Membrane Science, 1996. **120**(1): p. 111-121.
34. Camacho, M.L., et al., *Advances in Membrane Distillation for Water Desalination and Purification Applications*. Water, 2013. **5**(1).
35. Curcio, E. and E. Drioli, *Membrane Distillation and Related Operations—A Review*. Separation & Purification Reviews, 2005. **34**(1): p. 35-86.
36. Mulder, J., *Basic principles of membrane technology*. 2012: Springer Science & Business Media.
37. Khayet, M., et al., *Design of novel direct contact membrane distillation membranes*. Desalination, 2006. **192**(1-3): p. 105-111.
38. Criscuoli, A., M.C. Carnevale, and E. Drioli, *Evaluation of energy requirements in membrane distillation*. Chemical Engineering and Processing: Process Intensification, 2008. **47**(7): p. 1098-1105.
39. Drioli, E., V. Calabro, and Y. Wu, *Microporous membranes in membrane distillation*. Pure and Applied Chemistry, 1986. **58**(12): p. 1657-1662.
40. Smolders, K. and A. Franken, *Terminology for membrane distillation*. Desalination, 1989. **72**(3): p. 249-262.
41. Gryta, M., et al., *The influence of polypropylene degradation on the membrane wettability during membrane distillation*. Journal of Membrane Science, 2009. **326**(2): p. 493-502.
42. Martínez, L. and J.M. Rodríguez-Maroto, *On transport resistances in direct contact membrane distillation*. Journal of Membrane Science, 2007. **295**(1–2): p. 28-39.
43. Phattaranawik, J., R. Jiraratananon, and A.G. Fane, *Effect of pore size distribution and air flux on mass transport in direct contact membrane distillation*. Journal of Membrane Science, 2003. **215**(1–2): p. 75-85.

44. Ding, Z., et al., *Fouling resistance in concentrating TCM extract by direct contact membrane distillation*. Journal of Membrane Science, 2010. **362**(1–2): p. 317-325.
45. Goh, S., et al., *Fouling and wetting in membrane distillation (MD) and MD-bioreactor (MDBR) for wastewater reclamation*. Desalination, 2013. **323**: p. 39-47.
46. Summers, B.L., in *Effective Methods for Software and Systems Integration*. 2012, Auerbach Publications. p. 1-8.
47. Gryta, M., *Influence of polypropylene membrane surface porosity on the performance of membrane distillation process*. Journal of Membrane Science, 2007. **287**(1): p. 67-78.
48. He, F., et al., *Potential for scaling by sparingly soluble salts in crossflow DCMD*. Journal of Membrane Science, 2008. **311**(1–2): p. 68-80.
49. Verwey, E.J.W., *Theory of the Stability of Lyophobic Colloids*. The Journal of Physical and Colloid Chemistry, 1947. **51**(3): p. 631-636.
50. Curcio, E., et al., *Membrane distillation operated at high seawater concentration factors: Role of the membrane on CaCO₃ scaling in presence of humic acid*. Journal of Membrane Science, 2010. **346**(2): p. 263-269.
51. Gryta, M., M. Tomaszewska, and K. Karakulski, *Wastewater treatment by membrane distillation*. Desalination, 2006. **198**(1): p. 67-73.
52. Knyazkova, T.V. and A.A. Maynarovich, *Recognition of membrane fouling: testing of theoretical approaches with data on NF of salt solutions containing a low molecular weight surfactant as a foulant*. Desalination, 1999. **126**(1): p. 163-169.
53. Zhu, H. and M. Nyström, *Cleaning results characterized by flux, streaming potential and FTIR measurements*. Colloids and Surfaces A: Physicochemical and Engineering Aspects, 1998. **138**(2–3): p. 309-321.

54. Meng, F., et al., *Recent advances in membrane bioreactors (MBRs): Membrane fouling and membrane material*. Water Research, 2009. **43**(6): p. 1489-1512.
55. Alklaibi, A.M. and N. Lior, *Membrane-distillation desalination: Status and potential*. Desalination, 2005. **171**(2): p. 111-131.
56. Gryta, M., *Calcium sulphate scaling in membrane distillation process*. Chemical Papers, 2009. **63**(2).
57. Schneider, K., et al., *Membranes and modules for transmembrane distillation*. Journal of Membrane Science, 1988. **39**(1): p. 25-42.
58. Lee, G.J., et al., *Use of catalytic materials for the mitigation of mineral fouling*. International Communications in Heat and Mass Transfer, 2006. **33**(1): p. 14-23.
59. Tijing, L.D., et al., *Use of an Oscillating Electric Field to Mitigate Mineral Fouling in a Heat Exchanger*. Experimental Heat Transfer, 2009. **22**(4): p. 257-270.
60. Pangarkar, B.L., M.G. Sane, and M. Guddad, *Reverse osmosis and membrane distillation for desalination of groundwater: a review*. ISRN Materials Science, 2011. **2011**.
61. Darton, T., et al., *Membrane autopsy helps to provide solutions to operational problems*. Desalination, 2004. **167**: p. 239-245.
62. Gryta, M., *Effect of iron oxides scaling on the MD process performance*. Desalination, 2007. **216**(1): p. 88-102.
63. Hoang, T.A., H.M. Ang, and A.L. Rohl, *Effects of temperature on the scaling of calcium sulphate in pipes*. Powder Technology, 2007. **179**(1-2): p. 31-37.
64. Tijing, L.D., et al., *Heat-Treated Titanium Balls for the Mitigation of Mineral Fouling in Heat Exchangers*. Experimental Heat Transfer, 2008. **21**(2): p. 115-132.
65. Gryta, M., *Effectiveness of Water Desalination by Membrane Distillation Process*. Membranes, 2012. **2**(3): p. 415.

66. Morel, F., J.G. Hering, and F. Morel, *Principles and applications of aquatic chemistry*. 1993, New York: Wiley.
67. Salvador Cob, S., et al., *Silica and silicate precipitation as limiting factors in high-recovery reverse osmosis operations*. Journal of Membrane Science, 2012. **423–424**: p. 1-10.
68. Koyuncu, I. and M.R. Wiesner, *Morphological variations of precipitated salts on NF and RO membranes*. Environmental engineering science, 2007. **24**(5): p. 602-614.
69. Chong, T. and R. Sheikholeslami, *Thermodynamics and kinetics for mixed calcium carbonate and calcium sulfate precipitation*. Chemical engineering science, 2001. **56**(18): p. 5391-5400.
70. Waly, T., et al., *Will calcium carbonate really scale in seawater reverse osmosis?* Desalination and Water Treatment, 2009. **5**(1-3): p. 146-152.
71. Gryta, M., *Alkaline scaling in the membrane distillation process*. Desalination, 2008. **228**(1-3): p. 128-134.
72. Sheikholeslami, R., *Scaling potential index (SPI) for CaCO₃ based on Gibbs free energies*. AIChE Journal, 2005. **51**(6): p. 1782-1789.
73. Al-Anezi, K. and N. Hilal, *Scale formation in desalination plants: effect of carbon dioxide solubility*. Desalination, 2007. **204**(1): p. 385-402.
74. El Din, A.M.S. and R.A. Mohammed, *Brine and scale chemistry in MSF distillers*. Desalination, 1994. **99**(1): p. 73-111.
75. Al-Anezi, K. and N. Hilal, *Effect of Carbon Dioxide in Seawater on Desalination: A Comprehensive Review*. Separation & Purification Reviews, 2006. **35**(3): p. 223-247.
76. Gryta, M., *The influence of magnetic water treatment on CaCO₃ scale formation in membrane distillation process*. Separation and Purification Technology, 2011. **80**(2): p. 293-299.

77. He, F., K.K. Sirkar, and J. Gilron, *Studies on scaling of membranes in desalination by direct contact membrane distillation: CaCO₃ and mixed CaCO₃/CaSO₄ systems*. Chemical Engineering Science, 2009. **64**(8): p. 1844-1859.
78. Abraham, T. and A. Luthra, *Socio-economic & technical assessment of photovoltaic powered membrane desalination processes for India*. Desalination, 2011. **268**(1–3): p. 238-248.
79. Elfil, H. and H. Roques, *Role of hydrate phases of calcium carbonate on the scaling phenomenon*. Desalination, 2001. **137**(1): p. 177-186.
80. Beck, R. and J.-P. Andreassen, *The onset of spherulitic growth in crystallization of calcium carbonate*. Journal of Crystal Growth, 2010. **312**(15): p. 2226-2238.
81. Lioliou, M.G., et al., *Heterogeneous nucleation and growth of calcium carbonate on calcite and quartz*. Journal of Colloid and Interface Science, 2007. **308**(2): p. 421-428.
82. Olsson, L.-F., *Induction time of precipitation of calcium carbonate*. Journal of Molecular Liquids, 1995. **65**: p. 349-352.
83. Pokrovsky, O.S., *Precipitation of calcium and magnesium carbonates from homogeneous supersaturated solutions*. Journal of Crystal Growth, 1998. **186**(1): p. 233-239.
84. Yang, X., et al., *Study on membrane fouling experiment of stacked AGMD module in low temperature*, in *Advanced Materials Research*. 2012. p. 458-462.
85. Gryta, M., *Long-term performance of membrane distillation process*. Journal of Membrane Science, 2005. **265**(1–2): p. 153-159.
86. Karakulski, K. and M. Gryta, *Water demineralisation by NF/MD integrated processes*. Desalination, 2005. **177**(1): p. 109-119.
87. Sheikholeslami, R. and M. Ng, *Calcium Sulfate Precipitation in the Presence of Nondominant Calcium Carbonate: Thermodynamics and Kinetics*. Industrial & Engineering Chemistry Research, 2001. **40**(16): p. 3570-3578.

88. Sheikholeslami, R., *Mixed salts—scaling limits and propensity*. Desalination, 2003. **154**(2): p. 117-127.
89. Lee, S. and C.-H. Lee, *Effect of operating conditions on CaSO₄ scale formation mechanism in nanofiltration for water softening*. Water Research, 2000. **34**(15): p. 3854-3866.
90. Cheng, T.-W., et al., *Influence of Feed Composition on Distillate Flux and Membrane Fouling in Direct Contact Membrane Distillation*. Separation Science and Technology, 2010. **45**(7): p. 967-974.
91. He, F., J. Gilron, and K.K. Sirkar, *High water recovery in direct contact membrane distillation using a series of cascades*. Desalination, 2013. **323**: p. 48-54.
92. Gryta, M., *Desalination of thermally softened water by membrane distillation process*. Desalination, 2010. **257**(1-3): p. 30-35.
93. Tun, C.M., et al., *Membrane distillation crystallization of concentrated salts—flux and crystal formation*. Journal of Membrane Science, 2005. **257**(1-2): p. 144-155.
94. Edwie, F. and T.-S. Chung, *Development of simultaneous membrane distillation–crystallization (SMDC) technology for treatment of saturated brine*. Chemical Engineering Science, 2013. **98**: p. 160-172.
95. Stamatakis, E., et al., *An improved predictive correlation for the induction time of CaCO₃ scale formation during flow in porous media*. Journal of Colloid and Interface Science, 2005. **286**(1): p. 7-13.
96. Krivorot, M., et al., *Factors affecting biofilm formation and biofouling in membrane distillation of seawater*. Journal of Membrane Science, 2011. **376**(1-2): p. 15-24.
97. Schofield, R.W., A.G. Fane, and C.J.D. Fell, *Gas and vapour transport through microporous membranes. I. Knudsen-Poiseuille transition*. Journal of Membrane Science, 1990. **53**(1): p. 159-171.

98. Mistry, K.H., A. Mitsos, and J.H. Lienhard V, *Optimal operating conditions and configurations for humidification–dehumidification desalination cycles*. International Journal of Thermal Sciences, 2011. **50**(5): p. 779-789.
99. Dudley, L.Y. and E.G. Darton, *Pretreatment procedures to control biogrowth and scale formation in membrane systems*. Desalination, 1997. **110**(1): p. 11-20.
100. Scott, K., *Handbook of industrial membranes*. 1995: Elsevier.
101. Khayet, M., K. Khulbe, and T. Matsuura, *Characterization of membranes for membrane distillation by atomic force microscopy and estimation of their water vapor transfer coefficients in vacuum membrane distillation process*. Journal of membrane science, 2004. **238**(1): p. 199-211.
102. Gryta, M., *Osmotic MD and other membrane distillation variants*. Journal of Membrane Science, 2005. **246**(2): p. 145-156.
103. Tomaszewska, M., *Preparation and properties of flat-sheet membranes from poly (vinylidene fluoride) for membrane distillation*. Desalination, 1996. **104**(1-2): p. 1-11.
104. Burgoyne, A. and M.M. Vahdati, *Direct Contact Membrane Distillation*. Separation Science and Technology, 2000. **35**(8): p. 1257-1284.
105. Gryta, M., et al., *Treatment of effluents from the regeneration of ion exchangers using the MD process*. Desalination, 2005. **180**(1): p. 173-180.
106. Gryta, M., *CONCENTRATION OF NaCl SOLUTION BY MEMBRANE DISTILLATION INTEGRATED WITH CRYSTALLIZATION*. Separation Science and Technology, 2002. **37**(15): p. 3535-3558.
107. Guillen-Burrieza, E., et al., *Effect of dry-out on the fouling of PVDF and PTFE membranes under conditions simulating intermittent seawater membrane distillation (SWMD)*. Journal of Membrane Science, 2013. **438**: p. 126-139.

108. Gekas, V. and B. Hallström, *Mass transfer in the membrane concentration polarization layer under turbulent cross flow*. Journal of Membrane Science, 1987. **30**(2): p. 153-170.
109. He, K., et al., *Production of drinking water from saline water by direct contact membrane distillation (DCMD)*. Journal of Industrial and Engineering Chemistry, 2011. **17**(1): p. 41-48.
110. Agashichev, S.P. and A.V. Sivakov, *Modeling and calculation of temperature-concentration polarisation in the membrane distillation process (MD)*. Desalination, 1993. **93**(1): p. 245-258.
111. Hausmann, A., et al., *Performance assessment of membrane distillation for skim milk and whey processing*. Journal of Dairy Science, 2014. **97**(1): p. 56-71.
112. Banat, F., et al., *Desalination by a "compact SMADES" autonomous solarpowered membrane distillation unit*. Desalination, 2007. **217**(1): p. 29-37.
113. Guillén-Burrieza, E., et al., *Experimental analysis of an air gap membrane distillation solar desalination pilot system*. Journal of Membrane Science, 2011. **379**(1–2): p. 386-396.
114. Gryta, M., *Effectiveness of Water Desalination by Membrane Distillation Process*. Membranes, 2012. **2**(3).
115. Thiel, G.P., S.M. Zubair, and J.H. Lienhard V, *An Analysis of Likely Scalants in the Treatment of Produced Water From Nova Scotia*. Heat Transfer Engineering, 2015. **36**(7-8): p. 652-662.
116. Gryta, M., *Polyphosphates used for membrane scaling inhibition during water desalination by membrane distillation*. Desalination, 2012. **285**: p. 170-176.
117. Ghani, S. and N.S. Al-Deffeeri, *Impacts of different antiscalant dosing rates and their thermal performance in Multi Stage Flash (MSF) distiller in Kuwait*. Desalination, 2010. **250**(1): p. 463-472.
118. Lyster, E., et al., *A method for evaluating antiscalant retardation of crystal nucleation and growth on RO membranes*. Journal of Membrane Science, 2010. **364**(1–2): p. 122-131.

119. Al-Anezi, K., et al., *Effect of anti-scale agents on the solubility of CO₂ in seawater at temperatures of 60 to 90°C and pressures of 1–2 bar*. *Desalination*, 2008. **227**(1): p. 46-56.
120. Franken, A.C.M., et al., *Wetting criteria for the applicability of membrane distillation*. *Journal of Membrane Science*, 1987. **33**(3): p. 315-328.
121. Gloede, M. and T. Melin, *Physical aspects of membrane scaling*. *Desalination*, 2008. **224**(1-3): p. 71-75.
122. Lin, Y.-P. and P.C. Singer, *Inhibition of calcite crystal growth by polyphosphates*. *Water Research*, 2005. **39**(19): p. 4835-4843.
123. He, F., K.K. Sirkar, and J. Gilron, *Effects of antiscalants to mitigate membrane scaling by direct contact membrane distillation*. *Journal of Membrane Science*, 2009. **345**(1–2): p. 53-58.
124. Van der Hoek, J.P., et al., *RO treatment: Selection of a pretreatment scheme based on fouling characteristics and operating conditions based on environmental impact*. *Desalination*, 2000. **127**(1): p. 89-101.
125. Zhang, H., R. Lamb, and J. Lewis, *Engineering nanoscale roughness on hydrophobic surface—preliminary assessment of fouling behaviour*. *Science and Technology of Advanced Materials*, 2005. **6**(3-4): p. 236.
126. Drioli, E., et al., *Integrated system for recovery of CaCO₃, NaCl and MgSO₄·7H₂O from nanofiltration retentate*. *Journal of Membrane Science*, 2004. **239**(1): p. 27-38.
127. Zhang, J., et al., *M2M: A simple Matlab-to-MapReduce translator for cloud computing*. *Tsinghua Science and Technology*, 2013. **18**(1): p. 1-9.
128. Song, L., et al., *Direct Contact Membrane Distillation-Based Desalination: Novel Membranes, Devices, Larger-Scale Studies, and a Model*. *Industrial & Engineering Chemistry Research*, 2007. **46**(8): p. 2307-2323.

129. Ma, Z., et al., *Superhydrophobic Membranes with Ordered Arrays of Nanospiked Microchannels for Water Desalination*. Langmuir, 2009. **25**(10): p. 5446-5450.
130. Razmjou, A., et al., *Superhydrophobic modification of TiO₂ nanocomposite PVDF membranes for applications in membrane distillation*. Journal of Membrane Science, 2012. **415–416**: p. 850-863.
131. Shon, H., et al., *Physical, chemical, and biological characterization of membrane fouling*. Membrane technology and environmental applications, 2012: p. 457-503.
132. Phuntsho, S., et al., *Membrane autopsy of a 10 year old hollow fibre membrane from Sydney Olympic Park water reclamation plant*. Desalination, 2011. **271**(1–3): p. 241-247.
133. Yu, X., et al., *Experimental evaluation on concentrating cooling tower blowdown water by direct contact membrane distillation*. Desalination, 2013. **323**: p. 134-141.
134. Hilal, N. and W.R. Bowen, *Atomic force microscope study of the rejection of colloids by membrane pores*. Desalination, 2002. **150**(3): p. 289-295.
135. Vrijenhoek, E.M., S. Hong, and M. Elimelech, *Influence of membrane surface properties on initial rate of colloidal fouling of reverse osmosis and nanofiltration membranes*. Journal of Membrane Science, 2001. **188**(1): p. 115-128.
136. Hamachi, M. and M. Mietton-Peuchot, *Experimental investigations of cake characteristics in crossflow microfiltration*. Chemical Engineering Science, 1999. **54**(18): p. 4023-4030.
137. Mendret, J., et al., *Development and comparison of optical and acoustic methods for in situ characterisation of particle fouling*. Desalination, 2006. **199**(1): p. 373-375.
138. Xu, X., et al., *Non-invasive monitoring of fouling in hollow fiber membrane via UTDR*. Journal of Membrane Science, 2009. **326**(1): p. 103-110.
139. Shirtcliffe, N.J., et al., *An introduction to superhydrophobicity*. Advances in Colloid and Interface Science, 2010. **161**(1–2): p. 124-138.

140. Zhang, X., et al., *Superhydrophobic surfaces: from structural control to functional application*. Journal of Materials Chemistry, 2008. **18**(6): p. 621-633.
141. Nghiem, L.D. and A.I. Schäfer, *Fouling autopsy of hollow-fibre MF membranes in wastewater reclamation*. Desalination, 2006. **188**(1): p. 113-121.
142. Al-Khatib, A., *An experimental comparison of performance between flat sheet and hollow fiber membrane modules in direct contact membrane distillation system for desalination of seawater*. 2016, Qatar University.
143. Alkhudhiri, A., N. Darwish, and N. Hilal, *Treatment of saline solutions using Air Gap Membrane Distillation: Experimental study*. Desalination, 2013. **323**: p. 2-7.
144. Farid Benyahia, Y.M.a.A.F., *Evaluation of Membrane Distillation to Augment Water Production from Thermal Desalination Brines by Leveraging Low Grade Waste Heat*, ConocoPhillips, Editor. 2013.
145. lenntech. *Teflon*. 2014 [cited 2016 19-11-2016]; Available from: <http://www.lenntech.com/teflon.htm>.
146. Rainierrubber. *Viton fluoroelastomer*. 1998 [cited 2016 19-11-2016]; Available from: <http://rainierrubber.com/wp-content/uploads/2014/01/Viton-Selection-Guide.pdf>.
147. Julabo, *F32-MA Refrigerated/Heating Circulator*.
148. Scientific, T. *Thermo Scientific FH Series Peristaltic Pump Systems*. 2010 [cited 20-11-2016]; Available from: <http://www.thermofisher.com.au/Uploads/file/Scientific/Laboratory-Equipment-Furniture/Small-Equipment/FH-Series-Peristaltic-Pump-Systems.pdf>.
149. plastic, U. *Wall Versilon™ C-219-A Flexible PVC Tubing*. 28-2-2017]; Available from: <http://www.usplastic.com/catalog/item.aspx?itemid=102161>.

150. Toledo, M. *MS Precision Balances*. [cited 2016 19-11-2016]; Available from:
http://www.mt.com/us/en/home/products/Laboratory_Weighing_Solutions/Precision_Balances.html.
151. cooperation, E.i. *Model 421502 Dual Input Type J/K Digital Thermometer*. 2005 21-11-2016];
Available from: http://www.extech.com/resources/421502_UM.pdf.
152. AQUALYTIC. *Electrochemistry Meters SD 300 pH & SD 320 Con (IP 67 waterproof)*. 2015 21-11-
2016]; Available from: <http://dl.aqualytic.de/cat/en/sd300ph,sd320con.pdf>.
153. KRÜSS. *DROP SHAPE ANALYZER – DSA25* 22-11-2016]; Available from:
https://www.kruss.de/fileadmin/user_upload/website/brochures/kruss-bro-dsa25-en.pdf.

Appendix A: Antiscalant datasheet

The datasheet of the antiscalant used in this study, provided by the supplying company.

PRODUCT DATA

ASHLAND.

Ashland Hercules Water Technologies
www.ashland.com

Page 1 of 1

CWT-DS-069-R0-PERFORMAX 3S-200

PERFORMAX[®] 3S-200 Dispersant

Use

Performax 3-S200 is an anti-scalant for use in evaporator systems and thermal sea water desalination applications.

Performax 3-S200, is a modified polycarboxylate free of nitrogen and phosphorous. The molecular-weight of Performax 3-S200 is especially designed to control scale in high temperature applications with high particle content such as:

- Cooling systems with high cycles of concentration, or recycling waste water
- Scrubber systems in the incinerator or steel industry.
- Waste water treatment installations.

Features

- Using PERFORMAX 3-S200 in recirculating cooling towers allows for substantial water savings due to higher cycles of concentration which can be stabilised.
- PERFORMAX 3-S200 is compatible with oxidising biocides (chlorine, bromine, ClO₂, ozone etc.)
- PERFORMAX 3-S200 is a non-toxic, P free "all organic" formulation recommended for use in environmentally sensitive areas.
- The strongly dispersing polymers formulated in PERFORMAX 3-S200 allow scale free operation of low flow areas such as fillfill cooling tower packings and lamelle filters.
- The calcium tolerant ingredients of PERFORMAX 3-S200 allow its use in very calcium rich waters without the risk for Ca-polymer precipitations.

Appearance : yellowish
Density (kg/m³) : 1200
pH : 6
Solubility : miscible with water in all proportions
Freezing point : approximately < 0°C.

These data are to be seen as typical values and should not be considered as specifications.

Feeding

PERFORMAX 3-S200 is typically fed continuously in the make-up or directly in the system. The required dose rate is depending on the water chemistry, as well as the operating conditions (flow, temperature). Your Ashland representative will advise you about required dose rates for your systems.

The latest Ashland monitoring & control system; PULSE III should be used to evaluate the most effective dosage level and achieve the optimum level of system performance and reliability.

Handling precautions

Wear suitable protective gloves and safety goggles. In case of contact immediately flush with plenty of water. After eye contact seek medical advice. In case of spillage, absorb with sand or other absorbent materials and sweep up. Then flush the area with water. Before use review the Material Safety Data Sheet for additional information.

Important info

Ashland Corporate maintains Material Safety Data Sheets of all of its chemical products. Material Safety Data Sheets contain health and safety information relevant for your development of appropriate product handling procedures to protect your employees and customers. Our Material Safety Data Sheets should be read and understood by all of your supervisory personnel and employees before using Ashland products in your facilities.

Packaging

PERFORMAX 3-S200 is packed in 200 kg PE L-drum or a 1000 kg container.



HERCULES



ASHLAND[®] and its subsidiaries ("Ashland") believe that all information provided with respect to its products is accurate at the time such information is provided. All statements, information, and data presented herein are believed to be accurate but do not constitute a guarantee, an express warranty, or an implied warranty of merchantability or fitness for a particular purpose, or representation, express or implied, by which Ashland assumes legal responsibility. They are offered solely for your consideration, investigation, and verification. All recommendations or suggestions contained herein must be evaluated by the user to determine their applicability or suitability for a particular application. Users are encouraged to read and consult with the Material Safety Data Sheet (MSDS) and to abide by all use and safety recommendations detailed therein and on all product labeling. No freedom to use any patent owned by Ashland is to be inferred. (Trademark owned by a 501(c)(3) organization. © Registered trademark, Ashland or its subsidiaries. © 2009, Ashland.)

Appendix B: Salt rejection tables

The tables below present the calculated salt rejection percentages and the duration of each run operating at the higher feed flowrate of 2.5 L/min.

The salt rejection percentages for all runs of experiment code 7025.

Sample #	Run Duration (min)	Distilled conductivity (mS/cm)	Salt rejection %
1	313	0.015	99.99
2	303	0.016	99.98
3	302	0.028	99.97
4	258	0.281	99.65
5	252	0.486	99.33
6	296	0.618	99.09
7	296	0.379	99.42
8	277	0.872	98.64

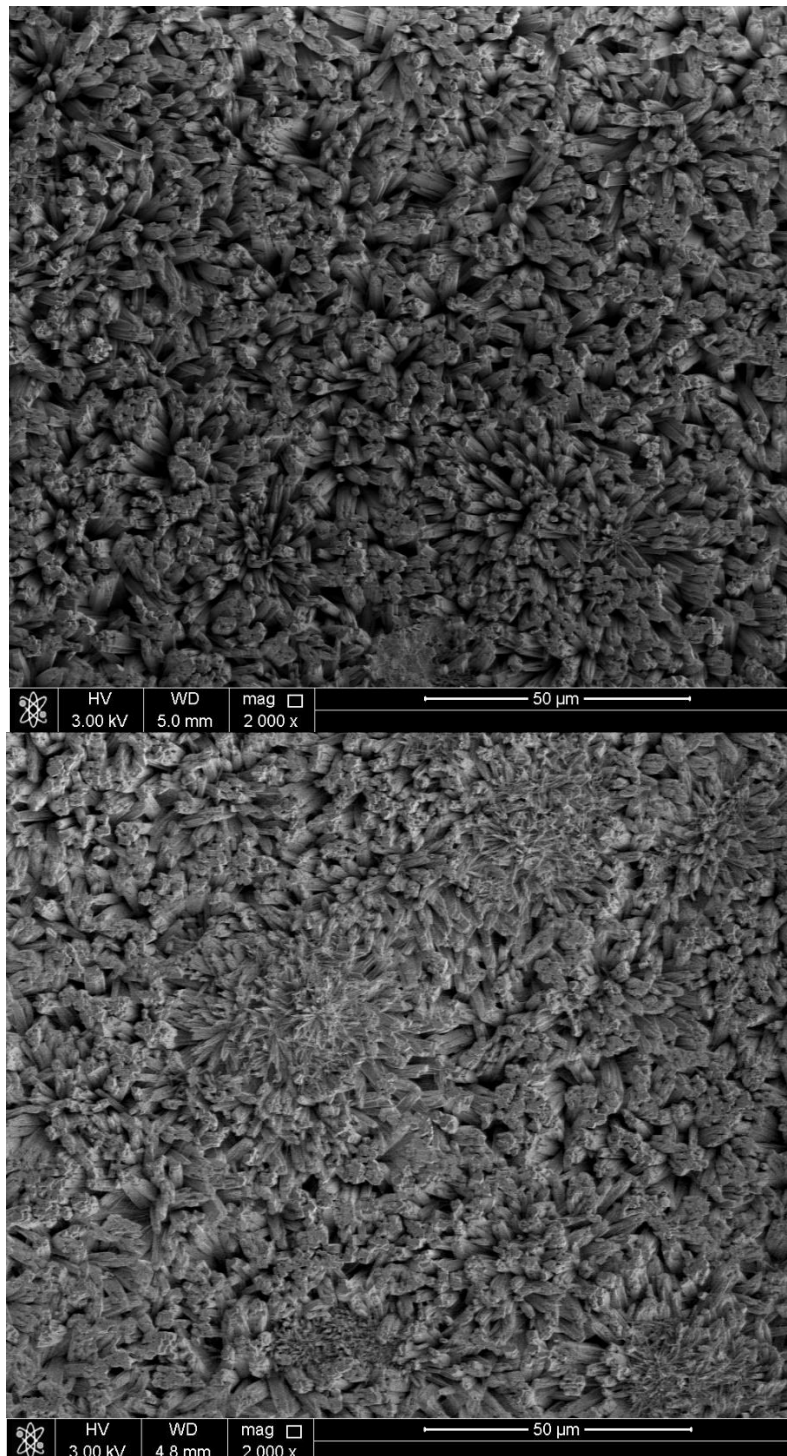
The salt rejection percentage for all runs of experiment code 6025.

Sample #	Run Duration (min)	Distilled conductivity (mS/cm)	Salt rejection %
1	252	0.046	99.94
2	267	0.015	99.98
2	231	0.024	99.98
4	264	0.024	99.98
5	302	0.03	99.97
6	298	0.23	99.77
7	292	0.071	99.92
8	288	0.04	99.96
9	205	0.059	99.94
10	306	0.098	99.89
11	300	0.205	99.77
12	242	0.124	99.86

The salt rejection percentage for all runs of experiment code 5025.

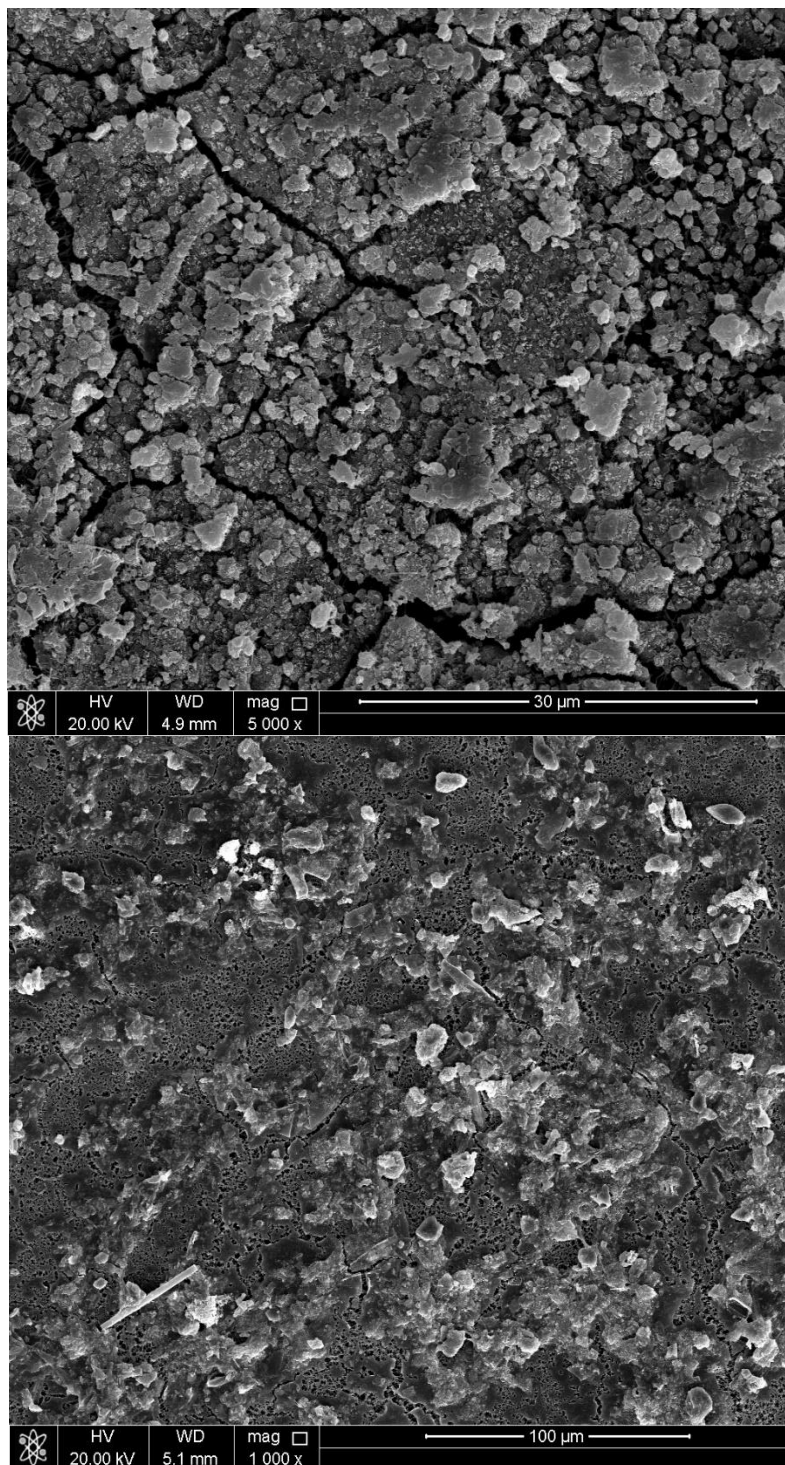
Sample #	Run Duration	Distilled conductivity (mS/cm)	Salt rejection %
1	226	0.032	99.96
2	333	0.061	99.93
3	318	0.026	99.97
4	244	0.027	99.96
5	310	0.045	99.95
6	289	0.053	99.93
7	289	0.035	99.96
8	287	0.015	99.98
9	309	0.035	99.96
10	271	0.09	99.89
11	270	0.045	99.94
12	290	0.05	99.94

Appendix C: SEM images of the used membrane for experiment code 7015



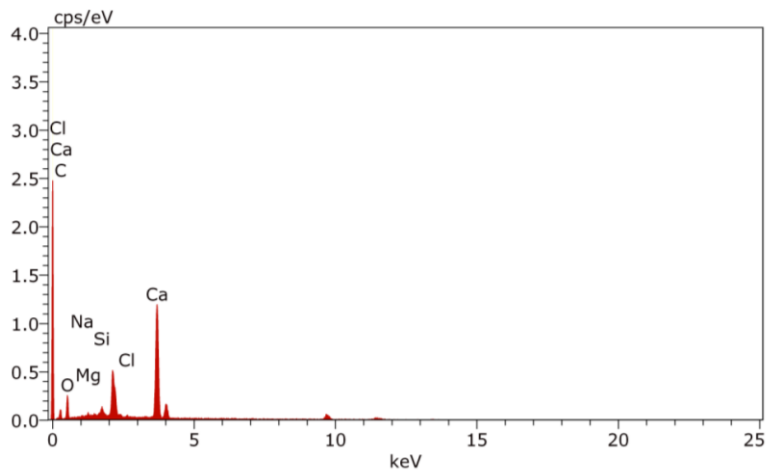
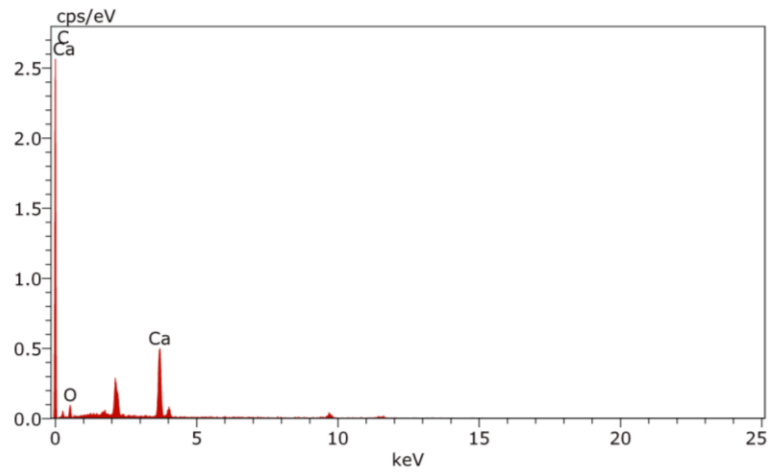
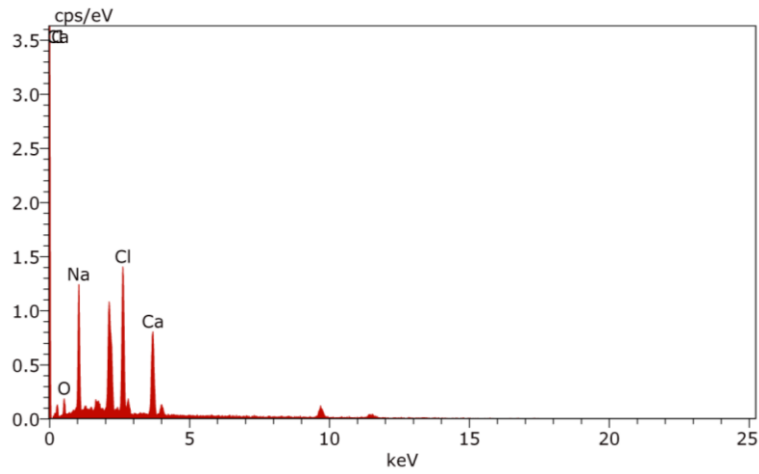
SEM images at low magnifications showing different sites of the fouled membrane surface having similar morphologies.

Appendix D: SEM images of the used membrane for experiment code 5015



SEM images of the used membrane showing cracks and uncovered parts of the surface indicating a less compact and more porous fouling layer.

Appendix E: EDS for experimental code 6025



The EDS showing that the elements on different parts of the used membrane surface are diverse, implying an uneven distribution of the constituents on the surface.